

ISTANBUL TECHNICAL UNIVERSITY ★ GRADUATE SCHOOL OF SCIENCE
ENGINEERING AND TECHNOLOGY

**NOVEL MECHANISM AND CONTROLLER DESIGN
FOR HYBRID FORCE-POSITION CONTROL OF HUMANOID ROBOTS**



Ph.D. THESIS

Cihat Bora YİĞİT

Mechanical Engineering Department

Mechanical Engineering Doctorate Program

FEBRUARY 2018

ISTANBUL TECHNICAL UNIVERSITY ★ GRADUATE SCHOOL OF SCIENCE
ENGINEERING AND TECHNOLOGY

**NOVEL MECHANISM AND CONTROLLER DESIGN
FOR HYBRID FORCE-POSITION CONTROL OF HUMANOID ROBOTS**

Ph.D. THESIS

**Cihat Bora YİĞİT
(503122002)**

Mechanical Engineering Department

Mechanical Engineering Doctorate Program

Thesis Advisor: Assoc. Prof. Dr. Pınar BOYRAZ BAYKAŞ

FEBRUARY 2018

İSTANBUL TEKNİK ÜNİVERSİTESİ ★ FEN BİLİMLERİ ENSTİTÜSÜ

**İNSANSI ROBOTLARDA BİRLEŞİK KUVVET-KONUM KONTROLÜ İÇİN
YENİLİKÇİ MEKANİZMA VE KONTROL TASARIMI**

DOKTORA TEZİ

**Cihat Bora YİĞİT
(503122002)**

Makina Mühendisliği Anabilim Dalı

Makina Mühendisliği Doktora Programı

Tez Danışmanı: Assoc. Prof. Dr. Pınar BOYRAZ BAYKAŞ

ŞUBAT 2018

Cihat Bora YİĞİT, a Ph.D. student of ITU Graduate School of Science Engineering and Technology 503122002 successfully defended the thesis entitled “NOVEL MECHANISM AND CONTROLLER DESIGN FOR HYBRID FORCE-POSITION CONTROL OF HUMANOID ROBOTS”, which he/she prepared after fulfilling the requirements specified in the associated legislations, before the jury whose signatures are below.

Thesis Advisor : **Assoc. Prof. Dr. Pınar BOYRAZ BAYKAŞ**
Istanbul Technical University

Jury Members : **Prof. Dr. Ekrem TÜFEKÇİ**
Istanbul Technical University

Assist. Prof. Dr. Figen ÖZEN
Haliç University

Prof. Dr. Şeniz ERTUĞRUL
Istanbul Technical University

Assist. Prof. Dr. Tolga EMİRLER
Okan University

Date of Submission : **1 February 2018**

Date of Defense : **28 February 2018**





To my family,



FOREWORD

Within the scope of this thesis, I have made mechanisms and control designs suitable for the needs of humanoid robots that I believe will take place frequently in our daily life in the future and make life easier. To achieve this goal, keeping the cost low and to make production easier was priority. I would like to think that the mechanisms obtained will contribute to the studies to be done in this area.

I would like to thank my thesis advisor Assoc. Prof. Pınar BOYRAZ BAYKAŞ who supported me and guided me in the difficulties I encountered during this study. I am also grateful to Ertuğrul BAYRAKTAR, my co-worker in all of our complementary studies, Ozan KAYA and Gökçe Burak TAĞLIOĞLU, who have made significant contributions with great effort. Through the thesis, I would like to thank the valuable System Dynamics and Control Laboratory and Mechatronics Education and Research Center assistants and students who have always motivated me with their valuable conversations. Finally, I appreciate endless support and faith of my family.

February 2018

Cihat Bora YİĞİT
(Mechanical Engineer)

TABLE OF CONTENTS

	<u>Page</u>
FOREWORD	ix
TABLE OF CONTENTS	xi
ABBREVIATIONS	xv
SYMBOLS	xvii
LIST OF TABLES	xix
LIST OF FIGURES	xxi
SUMMARY	xxiii
ÖZET	xxv
1. INTRODUCTION	1
1.1 Purpose of The Thesis	2
1.2 Literature Review	5
1.2.1 Humanoid robots	5
1.2.2 Structure of human joints	8
1.2.3 Joint mechanisms in humanoid robots	10
1.2.4 Elastic joints and variable stiffness actuators	12
1.2.5 Joint control and artificial intelligence	15
1.3 Contributions of The Thesis	17
1.4 Thesis Outline.....	18
2. NECK JOINT (CDPS) DESIGN AND ANALYSIS	19
2.1 Description of Cable-Driven Parallel-Series (CDPS) Hybrid Mechanism.....	20
2.2 Kinematic Model	21
2.3 Dynamic Model	27
2.3.1 Dimension reduction of the model	28
2.3.2 Helical spring analysis.....	28
2.3.3 Complete dynamic model.....	35
2.4 Experiments and Results	37
2.4.1 Experimental setup	37
2.4.2 Results	39
2.5 Conclusion.....	40
3. ELBOW - KNEE JOINT (VRP-VSJ) DESIGN AND ANALYSIS	45
3.1 VRP Mechanism Description and Synthesis Methods	48
3.1.1 Analytic solution and feasibility condition.....	48
3.1.2 Numerical methods.....	51
3.1.2.1 Simple iterative method.....	52
3.1.2.2 Optimization method	54
3.1.3 Implementation of VRP.....	57
3.2 VRP-VSJ Mechanism.....	58

3.2.1	Dynamic model	61
3.2.2	Stiffness adjustment ability	63
3.2.3	Position and stiffness control.....	63
3.3	Experimental Setup and Results.....	64
3.3.1	Tensile test of VRP mechanism.....	64
3.3.2	VRP-VSJ mechanism control.....	67
3.4	External F/T Estimation	69
3.4.1	Modifications in experimental setup	72
3.4.2	The estimation methods.....	73
3.4.2.1	KF approach.....	73
3.4.2.2	EFOB approach	75
3.4.2.3	Model-free approach.....	76
3.4.3	Results	78
3.5	Conclusion.....	80
4.	SHOULDER - HIP JOINT (VRP-VSJ3) DESIGN AND ANALYSIS	83
4.1	Description of VRP-VSJ3	84
4.2	Kinematic Model.....	86
4.3	Dynamic Model.....	88
4.4	Simulations	89
4.4.1	Simulation environment	89
4.4.2	Results	91
4.5	Experiments.....	92
4.5.1	Experimental setup	92
4.5.2	Experimental results	94
4.6	Conclusion.....	95
5.	CASE STUDY: FEEDBACK-FEEDFORWARD CONTROL.....	99
5.1	Object Recognition by DL.....	100
5.2	ADORESET: A Hybrid Image Dataset.....	102
5.3	Proposed Control Approach	105
5.4	Simulations	106
5.4.1	Simulation environment	106
5.4.2	Results	107
5.5	Experiments.....	107
5.5.1	Experimental setup	107
5.5.2	Results	109
5.5.2.1	Case 1: wrong positioning, manipulation failure	110
5.5.2.2	Case 2: wrong stiffness, low inertia, manipulation failure	110
5.5.2.3	Case 3: wrong stiffness, high inertia, manipulation failure	112
5.5.2.4	Case 4: correct stiffness, low inertia, manipulation success.....	113
5.5.2.5	Case 5: correct stiffness, high inertia, manipulation success	113
5.6	Conclusion.....	115
6.	CONCLUSION	117
6.1	Summary.....	117
6.2	Future Directions	120
	REFERENCES.....	121

CURRICULUM VITAE..... 134





ABBREVIATIONS

AI	: Artificial Intelligence
ANN	: Artificial Neural Network
CAD	: Computer-aided Design
CDPS	: Cable-driven Parallel-Series
CNN	: Convolutional Neural Network
DNN	: Deep Neural Network
DL	: Deep Learning
DOF	: Degree of Freedom
EFOB	: External Force Observer
EMG	: Electromyography
EOM	: Equation of Motion
FEA	: Finite Element Analysis
F/T	: Force/Torque
GSE	: Gazebo Simulation Environment
GUI	: Graphical User Interface
HRI	: Human-Robot Interaction
IMU	: Inertial Measurement Unit
KF	: Kalman Filter
LFP	: Low-pass Filter
MSE	: Mean Squared Error
PID	: Proportional Integral Derivative
PWM	: Pulse-width Modulation
RGB	: Red-Green-Blue
RMS	: Root Mean Square
ROM	: Range of Motion
ROS	: Robot Operating System
SEA	: Series Elastic Actuator
VRP	: Variable Radius Pulley
VIA	: Variable-impedance Actuator
VSA	: Variable-stiffness Actuator
VSJ	: Variable-stiffness Joint



SYMBOLS

θ	: Pitch angle
ϕ	: Roll angle
d_1	: Distance between the lower shaft and the lower plate
d_2	: Distance between the universal joint center and the upper plate
l_i	: Cable lengths
\mathbf{O}_i	: The points on the lower plate
\mathbf{P}_i	: The points on the the upper plate
$Tr.$: Translation matrix
f_i	: Error function about the cable lengths
\mathbf{q}_k	: Vector of the generalized coordinates
\mathbf{F}	: Vector contains the nonlinear error function
J	: The Jacobian matrix
\mathbf{E}	: Example motion vector
ρ	: The bending angle of the helical spring
\mathbf{N}_k	: Origin of every coil
$\varepsilon_x, \varepsilon_y$: Infinitesimal element frame
$C_{0,1,2,3}$: Control points of Bezier Curve
v_k	: The vector between 0 and 1
\mathbf{T}_i	: Tensions on cables
\mathbf{F}_{eq}	: Equivalent forces
\mathbf{M}_{eq}	: Equivalent moment
${}^k\mathbf{r}_\mu$: Position of an infinitesimal element
${}^k\mathbf{r}_\alpha$: Position vector of the infinitesimal element in the particular coil
${}^k\mathbf{M}_\mu$: Moment vector
${}^k\mathbf{M}_{\mu t}$: Total moment acting on the element
${}^k\mathbf{M}_c$: Resulting moment vector
$(U_b)_k$: Potential Energy (bending)
$(U_t)_k$: Potential Energy (torsion)
E	: Modulus elasticity
\bar{G}	: Shear modulus
I	: Area moment inertia
\bar{J}	: Polar moment inertia
R_{spring}	: Radius of the spring
$(U)_k$: Total strain energy
Δd_2	: Compression distance
K	: Stiffness matrix
$\dot{\mathbf{q}}, \ddot{\mathbf{q}}$: The velocity and acceleration vectors
M	: Mass matrix
C	: Coriolis and centrifugal forces
G	: Gravity matrix
B	: Mapping matrix

\mathbf{F}_s	: Generalized force vector of helical spring
\mathbf{s}_i	: Unit vector on the i^{th} cable direction
$F(u)$: Pulling force
u	: Elongation of the cable
$M(\alpha)$: Moment of linear torsional spring
α	: Pulley rotation
$u(\alpha)$: Cable Elongation
s	: Wrapped cable length
l	: Free cable length
β	: Departure angle
R	: Radius of the body
k_{spring}	: Spring coefficient
k	: Iteration step
$P_{o,k}$: Outlet point
p_n	: Departure point
P_i	: Points included by the convex hull
\mathbf{l}	: Unit vector in cable direction
J	: Inertia of the load side
θ_0	: Joint angle
T_i	: Cable tension forces
d_v	: Distance between link and cables
τ_{ext}	: External torque
f_{vrp}	: Force function for both VRPs
r_c	: Radius of the motor pulley
A	: State transition matrix
H	: Measurement matrix
\hat{x}	: Predicted state vector
P	: Covariance matrix
Q	: Noise covariance matrix
\bar{R}	: Measurement noise covariance matrix
K_k	: Kalman gain
z	: Measurements
cf_i	: Low pass filter frequency
F_{ref}	: Computed force
x_i	: Inputs
w_i	: Weights
b	: Bias term
y	: Outputs
μ	: Mean value
σ	: Standard deviation
θ_{M1}, θ_{M2}	: The motor angles
y_p	: Predicted outputs of the methods
y_a	: Ground-truth for force estimation

LIST OF TABLES

	<u>Page</u>
Table 2.1 : Simulation parameters in workspace analysis.....	27
Table 2.2 : Simulation parameters in helical spring analysis.....	33
Table 3.1 : Total cost of experimental setup for VRP-VSJ mechanism.....	68
Table 4.1 : Cable routing map between the lower and upper plate.....	84
Table 5.1 : Complete object class list in ADORESET.....	102





LIST OF FIGURES

	<u>Page</u>
Figure 1.1 : Joint types on human skeleton, composed by [1] and [2].	8
Figure 1.2 : Motion freedoms of human joints [3].....	9
Figure 1.3 : Series elastic actuators.....	12
Figure 1.4 : Schematic representation of VSA types: a)Spring preload b) changing transmission between load and spring.....	14
Figure 2.1 : CDPS mechanism and its components, with motors, bearings and capstans.....	21
Figure 2.2 : Neck mechanism with variables, local and global axes, cable lengths, upper and lower plate cable assembly points.	22
Figure 2.3 : Reduced serial kinematic model of neck mechanism with RRP structure (pitch, roll and translation).....	23
Figure 2.4 : Top view of the lower plate and an example motion command vector.....	26
Figure 2.5 : Workspace of the proposed mechanism in a) 3D b) Y-Z c) X-Z view d) Pitch and Roll Angles.	26
Figure 2.6 : Dimension reduction operation from the top view.	29
Figure 2.7 : a) Local frames on spring and infinitesimal element b) Top view of a spring coil.	29
Figure 2.8 : Coil origins and control points of Bezier curve.....	30
Figure 2.9 : Spring and cable forces acting on the mechanism.....	31
Figure 2.10 : Stiffness matrix change with respect to bending angle and compression length.	34
Figure 2.11 : The models of the mechanism in finite element analysis a) initial b) deformed.....	35
Figure 2.12 : Behaviour of the spring under compression and bending effects a) Reaction force b) Reaction moment.	36
Figure 2.13 : UMay neck mechanism.....	38
Figure 2.14 : Control structure used in experiments.	39
Figure 2.15 : Angular positions of the output shaft in pitch and roll axes.....	41
Figure 2.16 : Cable tension estimations from inverse dynamics and motor currents.....	42
Figure 3.1 : Schematic representation of the mechanism and components.	46
Figure 3.2 : Simplified view of VRP mechanism.	47
Figure 3.3 : Two possible use of variable radius pulleys to obtain a desired nonlinear spring: a) translational, b) rotational.	49
Figure 3.4 : Variables used in the analytical solution.....	50
Figure 3.5 : Variables used in simple iterative method.	52
Figure 3.6 : Variables used in optimization based method.....	55

Figure 3.7 : Synthesized pulley profiles: a) from three methods and b) 3D printed pulley image for optimization method.....	60
Figure 3.8 : Schematic view of VRP mechanism.	60
Figure 3.9 : Free body diagram of the mechanism.....	62
Figure 3.10 : Controller block diagram.....	64
Figure 3.11 : The tensile test equipment.	65
Figure 3.12 : Exploded view of VRP mechanism.....	66
Figure 3.13 : Force-elongation curves for three proposed methods from left to right: analytical, simple iterative and nonlinear optimization.	67
Figure 3.14 : Experimental results for the VRP mechanism synthesized to use in VRP-VSJ: a) force-elongation b) force-rotation c) rotation-elongation relations.	68
Figure 3.15 : Agonist-antagonist VRP pair force-elongation curves showing hysteresis.....	68
Figure 3.16 : Experimental setup for VRP-VSJ mechanism.....	69
Figure 3.17 : Control scenario outputs: a) Joint position control, b) Left pulley stiffness control, c) Right pulley stiffness control.	70
Figure 3.18 : Force-rotation curves for VRPs.....	73
Figure 3.19 : External force observer structure.....	76
Figure 3.20 : Fundamental neuron structure.	77
Figure 3.21 : Relation between the system and artificial neural network model. ...	78
Figure 3.22 : Encoder measurements used as the training and test data	79
Figure 3.23 : Comparison of external F/T methods	80
Figure 4.1 : Point and cable definitions of the lower (left) and upper (right) plate.	85
Figure 4.2 : Point and cable definitions of the lower (left) and upper (right) plate.	86
Figure 4.3 : VRP-VSJ3 in an arbitrary position in simulation environment.....	90
Figure 4.4 : VRP-VSJ3 simulation results.	91
Figure 4.5 : VRP-VSJ3 experimental setup.	93
Figure 4.6 : IMU measurements in VRP-VSJ3 single-axis motion experiment... ..	94
Figure 4.7 : IMU measurements in VRP-VSJ3 multi-axis motion experiment. ...	95
Figure 4.8 : VRP-VSJ3 multi-axis motion experiment, motor and VRP encoder measurements.....	96
Figure 5.1 : Preprocessed real images.....	103
Figure 5.2 : Preprocessed synthetic images.	104
Figure 5.3 : Block diagram of the presented control approach.	106
Figure 5.4 : Simulation results of pushing object via proposed control method... ..	108
Figure 5.5 : Experimental setup to test the control method.	109
Figure 5.6 : Manipulation failure due to wrong positioning.	110
Figure 5.7 : Images from the first case.....	111
Figure 5.8 : Manipulation failure due to high stiffness.....	112
Figure 5.9 : Manipulation failure regarding low stiffness.....	113
Figure 5.10 : Successful manipulation for low-inertia object.....	114
Figure 5.11 : Successful manipulation for high-inertia object.....	114

NOVEL MECHANISM AND CONTROLLER DESIGN FOR HYBRID FORCE-POSITION CONTROL OF HUMANOID ROBOTS

SUMMARY

Conventional rigid joint designs meet the industrial requirements, i.e., highly precise and stiff motions as much as possible. On the other hand, the humanoid robots are expected to move and seem as humans do. In order to bridge the gap between humans and humanoid robots, three different mechanisms and control algorithms are presented in this thesis.

The first mechanism presented in the study is composed of two plates connected with a two-part shaft having a universal-joint in the middle. The orientation of the top plate is changed by the cables which pass through the lower plate and are connected to the capstans on the motor shafts. A universal joint attaches each part of the shaft which constrains the motion of the mechanism and allows it to be treated as serial kinematic chain. The elasticity in the mechanism is provided by the helical spring that shows nonlinear behavior under combined compression and bending. The nonlinear behavior of the spring allows adjusting the stiffness of the mechanism. The full and simplified inverse kinematic models are presented in the study. Afterwards, the dynamic analysis which includes analysis of the nonlinear behavior of the helical spring is given in detail. Finite Elements Method is employed to validate the findings from the helical spring analysis by using Castigliano Theorem. The experimental results show that both kinematic and dynamic model are confirmed.

The second mechanism is based on antagonistic working principle. To assure the variable-stiffness property nonlinear springs are required. Variable radius pulley mechanism constitutes custom force-elongation curves by using linear torsional springs. Three synthesis methods are proposed to obtain desired nonlinear force-elongation curves and they are experimentally validated via a custom built tensile testing platform. Furthermore, the position and stiffness control is tested on the implemented mechanism. In addition to the control experiments, three algorithms are given for the estimation of external forces by using three encoder measurements.

The third mechanism is the combination of first two systems. The revolute joint in the second mechanism is substituted with a magnetic spherical joint. The kinematic and dynamic models of the system are formulated benefiting from previous designs. Both simulations and experiments are performed to validate the models.



İNSANSI ROBOTLARDA BİRLEŞİK KUVVET-KONUM KONTROLÜ İÇİN YENİLİKÇİ MEKANİZMA VE KONTROL TASARIMI

ÖZET

İlerleyen teknoloji ile birlikte, endüstride insanların yaptığı tekrarlı işleri önceden şekillendirilmiş ve başka insanların girmemesi için yalıtılmış ortamlarda yapan, robot olarak isimlendirilen programlanabilir makineler geliştirildi. Ancak insanlar, kendi işlerini yapabilecekleri ve kendileri ile benzer kabiliyetlere sahip makinelerin hayalini kurmuştur. Öncelikle bilim kurgu hikayelerine konu olan ve insansı robot olarak bilinen bu robotlar 1980’lerde ilk kez gerçekleşmiş ve bu tarihten sonra artan bir ivme ile geliştirilmeye devam etmiştir. Bu robotlardan hem görünüm hem fonksiyon açısından insanlara benzemeleri beklendiği gibi, endüstriyel robotlardan farklı olarak, kısıtlanmış alanların dışında ve daha önceden bilmediği ortamlarda, etrafındaki objelere zarar vermeden hareket etmeleri beklenmektedir.

İnsansı robotlar hareketlerini eklemleri vasıtasıyla gerçekleştirirler. Öncül insansı robot modelleri, endüstriyel robotlarda olduğu gibi katı ve kesin hareketler yapan eklemler içermekteydi. Ancak insansı robotlar ile endüstriyel robotlardan beklenenler arasında farklılıklar vardır. Endüstriyel robotlar önceden tanımlanmış bir görevi mümkün olan en yüksek doğruluk ve hız ile yerine getirmek üzere tasarlanmaktadırlar. Oysaki insansı robotlar, önceden programlanmadığı ve insanların bulunduğu ortamlarda belirli görevleri tamamlamak için üretilmektedirler. Bu nedenle insansı robotlar endüstriyel robotlardan hem hareket, hem algı kabiliyetleri açısından ayrılmaktadırlar.

Öte yandan insansı robot tasarımında amaç insan seviyesinde hareket kabiliyeti olduğu için, son yıllarda doğrudan insanın hareket sisteminden esinlenerek tasarımlar yapılmaya başlanmıştır. Temel olarak insanda hareketler kas-iskelet-tendon yapısı ile sağlanmaktadır. Kaslar kimyasal enerjiyi mekanik enerjiye dönüştürürken; tendonlar, kasların iskelete bağlantı noktasını teşkil ederler, adeta bir yay gibi çalışarak enerji depolarlar. Kasların eklemler etrafında oluşturulduğu yapıya bakıldığında antagonistik çalışma prensibi ön plana çıkmaktadır. Bu yapı iskeletin etrafındaki kas-tendon çiftinden oluşur. Tek bir kasın kasılması eklemin hareketini kontrol ederken, birlikte kasılma eklemin çıkış sertliğinde değişmeye neden olur. Kasların yay gibi çalışmasına ek olarak, üzerine düşen gerilmeden yola çıkarak dış kuvvetleri tahmin edebilme yetenekleri vardır.

Bu tez kapsamında, insansı robotların eklemlerinden beklenen özellikler göz önüne alınarak üç farklı; kablo ile sürülen, değişken sertlikli, kuvvet uyumlu, enerji verimliliği yüksek, düşük maliyetli, hafif, kolay imal edilebilen ve kompakt eklem tasarımı yapılmıştır. Farklı yapılar ve serbestlik derecelerindeki bu eklemlerin kinematik ve dinamik modelleri çıkarılmış, her biri için pozisyon ve sertlik kontrolü için yöntemler önerilmiştir. Hem elde edilen modelleri doğrulamak, hem de kontrol yöntemlerini test etmek adına eklemler üretilmiş ve deneysel olarak sınanmıştır.

İlk olarak 4 serbestlik derecesine sahip eklem tanıtılmıştır. Bu mekanizma iki plaka arasına sıkıştırılmış bir helisel yay ile iki parçalı bir milin kardan kavraması ile birleştirilmesinden oluşmaktadır. Mekanizmanın hareketi, alt plakanın altında bulunan motorlar tarafından sağlanır. Bu motorlar, millerine bağlı kasnaklar yardımı ile üst plakaya bağlı kabloları çeker veya bırakırlar. Bu şekilde üst plakanın 2 ekseninde dönme hareketi sağlanmış olur. Üçüncü dönme hareketi ise mekanizmanın ortasından geçen milin hareketi ile doğrudan sürülerek sağlanır. Bu mil yayın ve dolayısıyla mekanizmanın hareketini kısıtlayarak kinematik modelin seri mekanizmalarda olduğu gibi kolaylıkla elde edilmesini sağlar. Öte yandan yay sayesinde, mekanizma kuvvet uyumluluk kazandığı gibi, yayın hem basma hem eğilme zorlanmasına maruz kalması nedeni ile doğrusal olmayan bir davranış sergilemesine neden olur. Bu özellik kullanılarak, mekanizmanın dördüncü serbestlik derecesini oluşturan çıkış sertliği ayarlanabilir. Bu mekanizma için tam ve basitleştirilmiş ters kinematik modeller sunulmuştur. İleri kinematik model, gradyan bazlı metotlar ile elde edilmiştir. Bu mekanizmanın dinamik modelinin hesaplanabilmesi için öncelikle helisel yayların basma ve eğilme zorlanmalarına aynı anda maruzlarken davranışlarının incelenmesi gerekmektedir. Bu nedenle öncelikle yayın hareketini tanımlayan parametre sayısı herhangi bir veri kaybı olmadan indirgenmiştir. Sonrasında yayın her bir sarımı ayrıca ele alınmış, üzerinde oluşturulan sonsuz küçük elemanların potansiyel enerjileri hesaplanarak Castigliano teoremi yardımıyla izin verilen basma/eğilme aralığında oluşturacağı tepki kuvvet/moment değerleri bulunmuştur. Bu değerler 2x2 sertlik matrisi olarak belirli aralıkta sayısal olarak elde edilmiştir. Dinamik hesap yaparken tüm mukavemet hesaplarını tekrar yapmak yerine bu hesaplarda elde edilen sonuçlar tablodan interpolasyon yardımı ile çekilmiştir. Yay sertliğinin hesabını doğrulamak için aynı yay sonlu elemanlar yöntemi ile aynı etkilere maruz bırakılmıştır. Bu bilgiler ışığında mekanizmanın dinamik denklemleri elde edilmiştir. Elde edilen modeller, deney düzeneği üzerinde yapılan testler ile doğrulanmıştır. Bu mekanizmayı önemli kılan özellik sertlik değişimini sağlamak için piyasada rahatlıkla bulunabilen doğrusal helisel yay dışında herhangi ek bir ekipmana veya mekanizmaya ihtiyaç duyulmayışıdır. Burada yay, insan boynunu oluşturan 7 adet omurilik ile hem hareket hem yapı olarak benzeşmektedir. Bu nedenle bu mekanizma boyun eklemi için uygun olarak düşünülmüştür.

İkinci önerilen mekanizma tek bir eksen etrafında dönme kabiliyetine ve sertliğini değiştirebilme özelliğine sahiptir. Bu mekanizma tasarımı itibari ile insan kas-iskelet-tendon yapısına büyük benzerlik göstermektedir. Mekanizma, temel olarak birbirine bir dönel eklem ile bağlı iki plakadan oluşmaktadır. Hareket, dönel eklemin iki tarafında karşılıklı olarak duran üst plakaya bağlı kabloların doğru akımlı motorlar ile çekilmesi ve bırakılması ile elde edilmektedir. Mekanizmanın sertlik değiştirme kabiliyeti kabloların üst plakada bağlantı noktasındaki değişken yarıçaplı kasnak mekanizması ile mümkün olmaktadır. Bu mekanizma doğrusal özellikteki kurma yayı kullanarak istenilen kuvvet-uzama eğrilerini üretmeyi amaçlar. Mekanizmanın istenilen değerleri sağlayabilmesi için kasnak profilinin istenilen kuvvet-uzama eğrisine göre tasarlanması gerekmektedir. Tez kapsamında analitik, optimal ve sayısal olmak üzere üç metot önerilmiştir. Bu metotların performansları oluşturulan bir çekme düzeneği ile test edilmiştir. Değişken yarıçaplı kasnağın sentezlenmesinin ardından, eklem mekanizmasının kontrolü anlatılmış ve deneysel olarak hem sertliği hem de pozisyonu kontrol edilmiştir. Ek olarak, mekanizma üzerinde bulunan üç enkoder verisi kullanılarak mekanizma üzerine gelen dış kuvvetler tahminlenmiştir.

Kalman Filtresi, dış kuvvet gözlemcisi ve yapay sinir ağları bu amaçla elde edilen veri üzerinde çalıştırılmış ve sonuçlar karşılaştırılmıştır. Mekanizmada kullanılan motorlar dışarıdan hareket ettirilemez oldukları için, sabit konumda enerji harcamaz. Pasif yerçekimi kompanzasyonu olarak bilinen bu durum sağlanırken, elastik elemanlar sayesinde mekanizma dışarıdan gelen etkiler ile hareket ettirilebilir. Bu mekanizma hareket yapısı itibarıyla tek serbestlik dereceli olduğu için dirsek ve diz eklemlerinde kullanılabileceği düşünülmektedir.

İkinci mekanizmanın hareket kabiliyetinin tek eksenenden üç eksene artırılması ve dönel eklem yerine küresel mafsal kullanılması ile üçüncü mekanizma elde edilmiştir. Bu mekanizma literatürde az sayıda bulunan çok serbestlik dereceli değişken sertlikli eklem tasarımlarına örnektir. Mekanizma dört doğru akımlı motor-kasnak ve kablo ile hareket ettirilmektedir. Üç hareket bir sertlik olmak üzere dört serbestlik derecesine sahip olan bu mekanizma, manyetik küresel mafsal sayesinde geniş bir hareket kabiliyetine sahiptir. Kinematik ve dinamik modellerin sunulmasının ardından, önce benzetim ortamında, sonra da deneysel olarak hareket kabiliyeti sınanmıştır. Sonuçlar göstermektedir ki, hem hareket kabiliyeti hem de sertlik değiştirme özelliği bakımından; bu eklem omuz, bilek ve kalça eklemlerine kullanılabilir.

Sunulan tüm mekanizmalarda alt seviye pozisyon ve sertlik kontrolü anlatılmış ve deneyleri yapılmıştır. Ancak, herhangi bir obje ile etkileşime geçildiğinde sertliğin nasıl belirleneceği anlatılmamıştır. Tez kapsamında, objenin görsel veriler ile tanındığı ve fiziksel özelliklerine bağlı olarak temas noktası ve eklem sertliğinin ayarlandığı bir kontrol metodu önerilmiştir. Bunun için masaüstünde bulunan ve günlük hayatta sıklıkla kullanılan 30 objeden oluşturulmuş bir veri kümesi ve derin öğrenme teknikleri kullanılarak objeler tanınmıştır. Önerilen metot hem benzetim ortamında hem de deneysel olarak incelenmiştir. Sonuçta, her obje için geçerli tek bir sertlik değeri olmadığı ve yanlış sertlik veya temas noktası seçimi halinde etkileşimin kararsız olacağı ve başarısızlıkla sonuçlanacağı gösterilmiştir.



1. INTRODUCTION

The machines gradually became more complex and capable with each passing day. This capability is partly due to the programmable and controllable features integrated into the machines in the industrial age. The programmable and controllable machines, which are called robots, were first developed in the 1950s and they have become a crucial part of industry thereafter. The industrial robots have the ability to complete pre-described tasks repeatedly within a structured environment. Traditionally, because of the safety of humans and the continuous flow of the operation, the humans/human co-workers cannot enter into the robotic production cells while the robots are in operation mode.

The people have imagined machines interacting with and working for humans as well as resembling them since the ancient times. These machines were the ancestors of the robots which are known today as humanoids. Although humanoids are also classified as robots, their design requirements are different from the industrial robots. The mechanical structure of the robots should provide a safe interaction with humans and follow motion patterns similar to humans. In addition, the structure of the robot usually imitates the appearance of the humans as well. These robots should have an ability to respond the changes in the environment like a person does; therefore a better perception capability, control strategy, and decision making/artificial intelligence are required.

A robot can be described as a combination of joints and links from the mechanical perspective. In fact, the robot gains its ability of movement via joints. Thus, the motion of a robot is defined by its joints. This motion has to be very precise in most of the industrial cases; therefore the joints are designed as rigid as possible. In the humanoids, contrary to industrial robots, the rigid joints are not necessarily desired. In spite of preliminary examples of humanoid robots which utilized the rigid joints, elastic joints have started to replace with rigid ones in humanoids considering their requirements. In order to provide the elasticity and compliance which are much needed in humanoids, recently, the robotic joints have been designed using the varying elastic property to

comply with various tasks in the last decade. In addition to variable stiffness and elasticity in the joints, the actuation units are also coupled with joints in a tendon-driven manner as in human muscular system. As an alternative to the conventional direct-drive technology, this trend is using elasticity to increase the similarity between the human and humanoid motions, and tendon based structures tend to be lighter and give more space of design for the robotics researcher.

Another aspect of robotic design in humanoids is the control of the applied force while planning for a precise trajectory. This type of trajectory may involve physical interaction with surrounding objects and people in an unstructured environment. Therefore, a combined force and trajectory/position control strategy is searched after. In addition to this extra control ability, the humanoids are expected to be able to do complex tasks that people can do, so their ability to perceive and semantic inference should be high. As a result, the humanoid applications are more demanding in the control and perception fronts, therefore, more open for AI implementations.

In this thesis, three different tendon-driven variable stiffness joint mechanisms are designed and presented. After detailing the general conceptual and geometric design, the kinematic and dynamic analyses are given with corresponding simulation results. Next, the application of low-level control algorithms for the mechanisms is mentioned together with the experimentally evaluated performances. Finally, a force control strategy based on the visual object recognition using deep-NN is demonstrated in an object manipulation task.

After this brief introduction herein, the next section opens with the purpose of the thesis. Then, in order to have a better insight and understanding of the topic, many similar studies and inspiring research results are presented. Next, the contributions of this thesis are given to clarify the differences from the previous studies and show how this thesis advances the past achievements in the field. Finally, this section finishes with an outline of the thesis.

1.1 Purpose of The Thesis

The humanoid robots which are designed according to the general design criteria of industrial robots fall short of the requirements of safe human-robot interaction and

following the human motions in terms of smoothness, force control, and dexterity. Industrial robot joints are built as stiff as possible to ensure the position accuracy. Unlike industrial robots, humanoid robots are expected to interact with humans and other surrounding objects, having less or no requirements on the position accuracy. The joints of a humanoid should, therefore, be designed with a different approach so that HRI is safe, especially when an impact is unavoidable. Another difference in the requirements can be observed in task-dependency. For example, industrial robots are supposed to perform a given task in a minimum time window; therefore, sharp motions involving high levels of acceleration are acceptable. On the other hand, in humanoid robots, the motions with sharp characteristics and high level of accelerations are not desired due to safety concerns.

In order to build a humanoid robot with desired characteristics, investigation of the human body, especially the muscle-skeleton system, is a good starting point. Human muscles are settled around the bones and work mutually with other muscles. Since they are able to pull only, every skeletal muscle exists with its antagonist pair which is responsible for intentional motions. In recent years, cable-driven robotic actuation systems have been developed. Similar to the muscles, cables are unidirectional and cannot be subjected to compression forces. Thus, cable-driven joints resemble human muscle system and often called as tendon-driven system due to similarities between them especially in force related sense. Furthermore, human muscles behave like a mechanical spring and capable of storing energy. This property is beneficial for energy efficiency in most of the tasks, especially in walking. By storing and releasing elastic energy in the Achilles tendon, people improve the effectiveness of lower leg joint a long way past what is feasible for work. Beyond energy efficiency, this feature allows people to interact with humans and objects around them without posing a harmful effect. It is worth noting that precision is not often the main goal for most of the daily activities. Once the precision is needed, antagonistic muscle pair works together and increase the stiffness. Therefore, the muscle resembles springs in mechanics and can adjust its stiffness depending on the task necessities. VSA has recently gained popularity in robotics research field. These mechanisms comprise elastic elements with special designs to set the desired stiffness value. Following their biological counterparts in the human body (i.e., shoulders, neck and ankle), these mechanisms

have multiple degrees of freedom per joint, instead of the single DOF mostly seen in industrial robotic mechanisms. The industrial robots generally use single DOF joints successively, whereas, the certain humanoid designs employ multiple DOF. One way to achieve multiple DOF is to use parallel actuation, for instance, universal and spherical joints. In addition to resembling the DOF of the human musculoskeletal system, the actuation of such mechanisms can have internal feedback. As well as being actuators of the human body, muscles are competent to sense exerted forces so that people can feel roughly how much weight they are carrying without measuring the object. In the conventional robotics, actuator and sensors are designed to perform separate tasks. The elastic element, beyond being a prominent part of the actuator in VSAs, acts as a force sensor due to its deformation. Besides, in order to capture a resembling nature of the human motion, the humanoids also require a control structure which is different from the classical approach. Human intelligence benefits from a good blend of feedforward and feedback control whilst feedback control is a common approach in industrial robotics. In this context, recent advances in deep learning area could extend the capability of control strategies in humanoid robotics supporting this feedback and feedforward structure.

From the overview of a wide range of robotics, it can be seen that there is an exciting tide of solutions to joint design problem, perception, learning and control. However, the unified solution is still required. The problem cannot be resolved by mechanical design improvements or advancements in perception or control alone. These fields should be integrated to obtain an original and feasible solution advancing the area in multiple aspects. In this thesis, the goal is to present humanoid joint designs for the motion of head and limbs with the energy-efficiency, compliance, cable-driven and variable stiffness properties. Besides these capabilities, the mechanism should have simple structures and it should be easily manufacturable as well as being low-cost to be a part of our daily lives in the future. The underlying theory of the mechanisms with kinematic and dynamic analyses are attempted to be explained alongside with the synthesis methods to design similar mechanisms for specific assignments. Moreover, force interaction and position control are two important aspects in humanoid robot

design. Another aim is presenting both low and high-level control applications with experimental results to evaluate the performances.

1.2 Literature Review

In order to better explain the contributions of this thesis, first, a general literature overview is presented covering the current research trends in humanoids. This section is divided into five subsections to increase clarity; i) humanoid robots, ii) structure of human joints, iii) joint mechanisms in humanoid robots, iv) elastic joints and variable stiffness actuators and v) joint control with artificial intelligence. The literature overview here also provides a general perspective for the whole thesis. The detailed literature surveys are given in each chapter having the relevant topics to have a succinct introduction into the thesis here and have adequate space for the detailed literature analysis later in their own respective sections.

1.2.1 Humanoid robots

Robots that resemble the human body in both movements/functions and appearance are called humanoid robots [4]. The first concrete example Wabot-1 [5] is a two-legged walking robot (biped). This robot has artificial ears and mouth and has oral communication skills. Although it seems primitive with today's technology, the foundations of advanced humanoid robots have been laid in this early example.

After the development of Wabot, high-profile firms have started to develop such robots. For example, Honda is the leading company which started biped robot project (P1) in the middle 1980s and today Asimo, the 11th version, is one of the most advanced humanoid robots. Despite its rigid joint structure [6], it can run at 6 km/h and climb stairs [7]. Humanoid robot design is still a focus of active research. Many rigid-joint robots have been developed and are now commercially available for research and development purposes while focusing on different aspects ranging from mechanical design to perception capabilities. For instance, HRP-4 is designed to be light-weight and low-power life-size humanoid robot [8]. Similar to HRP, Nao is a well-known robot in a broad range of research applications such as Robocup standard league football [9] and autism rehabilitation [10]. Another commercially available humanoid robot is Personal Robot (PR2) which is a test platform for Robot Operating System

(ROS) [11]. Instead of biped walking, PR2 provides locomotion by its omnidirectional wheeled mobile base. Unlike the commercial examples, Icube is an open-source project and available online. This robot is manufactured in the average size of a human infant and is also expected to learn everything from crawling to walking as human infants do [12].

Anthropomorphism is a term that defines the attribution of human properties to non-human individuals or objects, and this concept is heavily applied in humanoid robot design. An anthropomorphic robot design considers the real human body dimensions. This concept was first applied to the "Manny the mannequin" robot that has the ability to sweat and breathe in 1988 [7]. Researchers in the University of Tokyo have approached anthropomorphism concept in a more realistic manner and transferred the model of the human musculoskeletal system to a set of robots, finally designing Kenshiro with the aim of simulating human motions [13]. The motion of Kenshiro is generated by electric motors and tendons. Furthermore, the muscles and bones are imitated based on the human body in the sense of shape, power levels, and placement/location. These tendons are flexible like human muscles. In another study, humanoid robot Justin was designed to gain compliance by using elastic actuation which allows safe human-robot interaction and tasks requiring force control such as assembling objects [14], cleaning a board or sweeping a table [15] without harming them through the torque sensors on each joint. In addition to testing the performance of the robot in the daily tasks in which the robot should be moving in a gentle motion, the safety of the arm is also evaluated in the impact scenarios in a crash test. [14].

The interaction between the humans and robots should be examined not only in the physical sense, but also in the sociological and psychological dimensions. Social robotics is the area which investigates the psychological effects of human-robot interaction. A well-known hypothesis suggests that over a certain level of humanoid resemblance to human beings are not welcomed. This phenomenon is known as uncanny valley [16]. However, the hypothesis has become a matter of debate in recent years. It is shown that exceptionally humanlike robot showing feelings can reduce death-thought, thus uncanniness [17]. In addition, humanoid robots with human-like faces and expressions or androids, are used in autism rehabilitation purpose [18, 19]. Social interaction is also a necessity for service robots which assist people in their

daily work. For example, REEM, a service humanoid robot, can assist people in daily activities through its indoor visual navigation system [20].

Humanoid robots are not only useful in daily jobs, but also they can perform tasks that are considered to be dangerous for human beings. NASA and General Motors have developed Robonaut 2 for space exploration missions that are expected to work with other astronauts and activate switches, use power tools and manipulate objects [21]. Like the space operations, the military fronts and operations can also pose a threat to human safety. In order to deploy missions without human soldiers or assist them in dangerous situations, robotic solutions are searched for. One example of this application is Atlas, which is a highly mobile biped robot with elastic joints, are designed by Boston Dynamics Company that formerly manufactured big dog for assistance to soldiers. The robot has appeared in [22] Darpa Robotics Challenge which is a competition for [23] paving the path for obtaining more realistic search and rescue robotic platforms. The theme of search and rescue has become prominent especially after Fukushima disaster and the questions on why robots cannot help the people. The aim of the competition was to make robots interact with the unstructured environment objects like cars, valves or demolished concrete in a disaster scenario [23]. Another recent application of risky tasks is Ocean One robot, which is developed by Stanford University. The goal of the robot is to be an avatar for users in under-water explorations by using a haptic interface [24].

Together with the advancements in additive manufacturing technology, humanoid robot designs are also upgraded. Poppy [25] and Inmoov [26] are examples of this new approach which have 3D printable open-access designs. While reducing the manufacturing cost of the robot, this new trend makes it more accessible to the researchers all over the world.

Although all humanoid designs are not covered, the most influential design trends are selected and detailed here. It is for the sake of brevity that this overview is kept at a reasonable length. For further information on the general humanoid design, a detailed survey on the topic could be found in the review article [7].

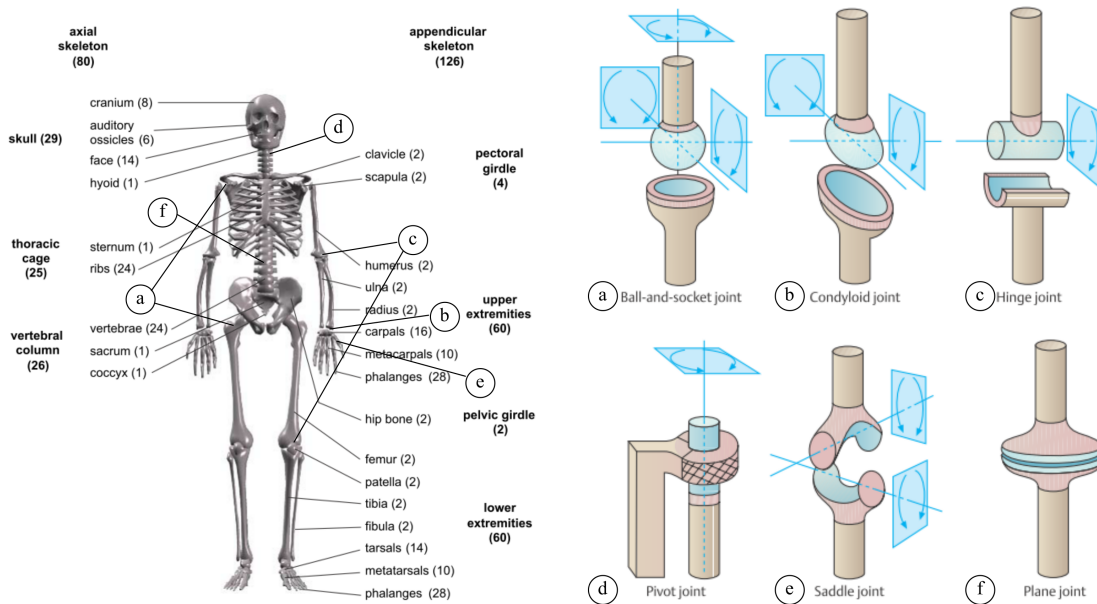


Figure 1.1 : Joint types on human skeleton, composed by [1] and [2].

1.2.2 Structure of human joints

Before browsing the literature for humanoid robot joints, first having a look into the human musculoskeletal system could be beneficial. Rather than a detailed analysis, an engineering point of view to human anatomy is attempted in this section, since this study is an engineering thesis. First, musculoskeletal system is introduced, and the human joint types are examined. Then, general muscle behaviors are presented with antagonistic working principle.

The tree of total 206 bones forms the frame of the human body connected together by ligaments in joints [1]. There are three types of joints which are classified in the allowable motion range. First two types are called as synarthrosis, and phiarthrosis that are either immovable or slight motions are permitted. Therefore, only the third type (diarthrosis or synovial joints) is of interest in this thesis because of the generation of human limb and head motions is the goal. Movable joints are also divided into six categories corresponding to the DOF in motions [2]. Skeletal system and the mechanical analogies of the joint categories is shown in Figure 1.2.

It is worth mentioning that the aim of the thesis is designing a mechanism following/copying the functional abilities of the human joints rather than replicating them. In robotics, the complex motion data of human is captured and degraded into a more simple structure composed of 1 and 3 DOF joints [3] which is shown in Figure 1.2. Nevertheless, the robot used in the study does not have 3 DOF joints in

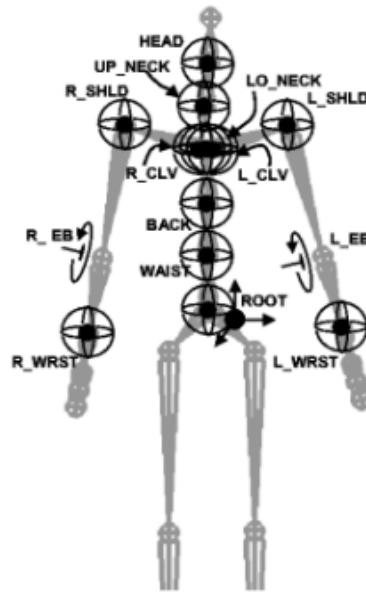


Figure 1.2 : Motion freedoms of human joints [3].

upper-limbs and researchers try to scale the data to the robot available for research. In fact, it is common to assume that human arm [27] and leg [28] to have 7 DOF whilst the wrist and ankle are not actually spherical joints. Similar to humans, 7 DOF humanoid arms can have multiple configurations without moving end-effector (hand) as a result of redundancy. Consequently, having only revolute (knees and elbows) and spherical joint (neck, shoulders, wrists, hips and ankles) modules, 31 DOF humanoid which is capable of imitating human locomotor motions can be implemented.

Muscles are responsible for human motions and classified into three categories [1]: i) Visceral muscle ii) cardiac muscle, and iii) skeletal muscle. First two of the muscle groups are related to heart and inner body activities, so they cannot be activated by conscious mind/motor neuron system. Muscles in the third type are connected to the peripheral nervous system and can both be controlled and receive the force feedback using spindles [29]. The muscles produce force by contracting in a series of chemical processes, in which actin and myosin protein filaments in their cells get involved, yielding various force-length and force-velocity models which are detailed in [30]. Tendons are the anchors between muscles and the joints; furthermore, they store the elastic energy and give the ability of spring-like behavior which is investigated in a multi-joint limb in [31]. At the macroscopic level, the arrangement of muscle fibers is called muscle architecture. When the muscle architecture changes, force-length and force-elongation characteristics change [32]. Also, the muscle-tendon

internal architecture affects the use of force economically and the recovery of elastic energy [33]. From the anatomical point of view, skeletal muscles are arranged in an antagonistic manner to form a functional musculoskeletal structure. Co-contraction of an antagonistic pair of muscles can adjust the impedance to stabilize the posture against the perturbances [34].

Researchers from the areas of biomechanics and robotics may benefit from the increase in the accuracy of musculoskeletal models. A freely available software OpenSim presents a possibility to simulate musculoskeletal structure with realistic results [35]. In addition to simulating human motions accurately, knowledge of the limits of joint motions is substantial in humanoid design in order to start with already feasible dimensions. Despite being designated for space operations, NASA Man-System Integration Standards can form a basis for anthropomorphic dimensions [36].

All in all, although the basic structures of the musculoskeletal systems are understood, it is still necessary to study the movement mechanism and the relation with the brain [37]. Robotics have achieved a long way in the light of the biomechanics research, and yet there is still room for basic and applied research.

1.2.3 Joint mechanisms in humanoid robots

After having an insight on how human skeletal and muscular systems work together, the joint architectures in existing humanoid robots may be reviewed. Because the joint structures adapt themselves according to their locations in the body, the state of art mechanisms given here only include the neck, shoulders (upper limb) and hips (lower limb) to make less confusion.

In the human body, neck consists of 7 vertebrae, atlas bone and around 22 muscles [2]. Vertebrae behave like a spring and muscles are responsible for various motions. Likewise, the other joints of the human body, the neck joint is simplified to a certain extent when applied in humanoid design in order to make a simpler and feasible implementation. The neck mechanism of robot KHR-3 simplifies the complex structure to 2 DOF joint with harmonic drives and DC motors [38]. A more advanced version of this mechanism comprises 4 DOF; 2 for leaning side by side, 1 for rotation around the longitudinal axis and final one for nodding. 4 DOF mechanisms are obtained using four-bar [39], differential [40] and belt-pulley [41] mechanisms. In lieu

of stiff designs, cable-driven and spring based solutions are proposed [42, 43]. These solutions make it difficult to solve the kinematics in spite of increasing similarity to human beings.

Akin to neck structure in the human body, another complicated part is the shoulder complex. The human shoulder includes four joints, and two of them act as a spherical joint, i.e., sternoclavicular and acromioclavicular joints. Moving parts clavicle and scapula and a constant bone sternum/thorax form a 12 DOF parallel mechanism [44]. A simple approach to shoulder design problem is building a 3 DOF serial manipulator [41], [45]. Researchers in [27] proposed a 3 DOF spherical joint and cable-driven configuration. In [46], a parallel spherical mechanism is presented. The spherical six-bar linkage mechanism is a promising step further and presented with kinematic calculations [44]. But the prototype is difficult and expensive to manufacture. The most advanced shoulder concept is given in [44] with a qualitative comparison between real human motions and the mechanism. Despite the successive results in simulations, the mechanism is not implemented. The researchers in [47, 48] addressed the imitation of compliance as well as kinematics. 3 DOF mechanism has programmable compliance in [47] so that the elasticity can be set for different payloads. On the other hand, the human shoulder is replicated with most of the bones and joints in [48]. Albeit it is possible to replicate human motions within this configuration, it is not possible to produce desired motions as a result of impossibility to copy all muscles.

Humanoid robot's locomotion is provided by either a wheeled-base or two-legged structures, which is known as biped robots. The hip joint is the connection point between the leg and the robot, thus has an important role in walking. The simplest design includes 2 DOF serial hip joint in Nao Robot [49]. 3 DOF serial drives form a spherical joint with axes intersecting at one point, is the most common implementation with a belt and gear transmission [50–52]. The robot Robian benefits from a parallel mechanism [53] instead of serial one. Energy efficiency of the walking task is increased by using double spherical joint in hips [54]. Similar to shoulder joint, elastic components have been used in designs partially [55] or completely [56, 57]. The impedance values are modulated in the design of robot Blue [58] through a modified version of AWAS [59] considering human motion patterns.

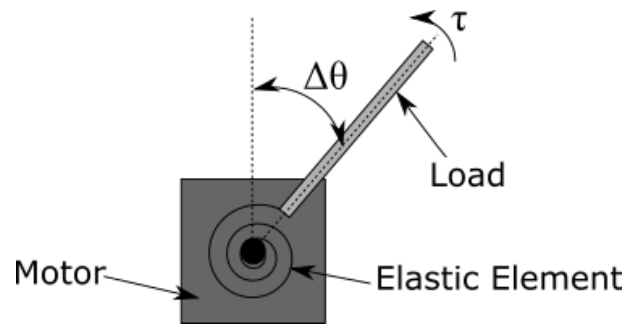


Figure 1.3 : Series elastic actuators.

Despite the great effort by humanoid robot researchers, there is still no perfect solution to the imitation of human motions problem. In fact, the human body is too complicated to be replicated in a humanoid robot. It is not possible to replicate all the muscle arrangements with state of the art actuation techniques. The mission of the robot designers is to maximize the similarity between human and robot in terms of look, motion and interaction whilst reducing complexity and cost of the robot. It is worth noting that the focus of this thesis is to design humanoid robot joints which resemble human joints in functionality but not on the appearance while preserving simplicity and keeping costs low.

1.2.4 Elastic joints and variable stiffness actuators

Safety has been an important and expanding topic within the robotics in recent years. In the conventional approach, to increase precision, robot joints are built as stiff as possible, but in the recent research more elastic elements are proposed in between the connection of motor and load [60]. However, it is understood from the experiments that single stiffness values is not suitable if we would like to achieve several tasks with the same robotic arm. To set the stiffness/impedance value, variable stiffness actuators (VSAs) or in general variable impedance actuators (VIAs) have been developed.

After reaching the desired position, industrial robots tend to hold the position against external forces (i.e., gravity) using active motor input. Moreover, they track desired motion profiles accurately to complete the well-defined repetitive task in a structured environment. On the other hand, external effects are allowed to change the position of the joint in SEA mechanism design due to the elastic element between the motor and the load. Considering the constant-stiffness (k) elastic element, the static equation is

in linear form as follows:

$$k = \frac{d\tau}{d\theta} \quad (1.1)$$

$$\tau = k \delta \theta \quad (1.2)$$

The symbol τ denotes the torque; the angle is represented by θ . The deflection of the elastic element is computed by the difference between free and final positions and shown by δ . The relation between torque and deflection angle is non-linear in VSA mechanisms which yields a variable output stiffness as given in equation (1.3).

$$d\tau = f(\theta) d\theta \quad (1.3)$$

where $f(\theta)$ is the nonlinear stiffness function. The response of the joint to external forces could be adjusted with respect to the desired task by changing joint stiffness. A classification of stiffness adjustment mechanisms in literature is given [61] in three main categories: i) Spring preload, ii) Changing transmission between load and spring, and iii) Physical properties of the spring. The first type is the system in which a couple of springs and motors work mutually, i.e., antagonistic springs. In this category, the working principle imitates biological musculoskeletal system. To obtain a linear stiffness change, a quadratic spring is built using a cam mechanism with a linear helical spring [62]. Researchers in [63] show the significance of quadratic springs in VSA design. Second and third mechanism design proposed in this thesis is built on this idea. Mechanisms fall in the second kind, changes the distance between the rotation center and one of the following: linear spring connection point or tip point to set a desired non-linear torque-position relation [59]. Mechanisms in the last type utilizes natural characteristics of linear springs. The Jack spring mechanism specifies the number of helical spring active coils causing stiffness variation [64]. The first mechanism presented in this thesis is included in this type and stiffness variation is obtained by the pure response of the linear helical spring under bending and compression effect. A general schematic representation of first two types is given in Figure 1.4.

Power is usually generated by electrical motors in VSAs, whereas there are VSA designs which are actuated by pneumatically artificial muscles [65]. Another variant to actuation concepts is using low-cost and low-precision electrical motors, in other words, hobby servo motors. In [66], a modular VSA is coupled with hobby servo motors to reduce the cost. Likewise to actuation components, elastic parts could differ

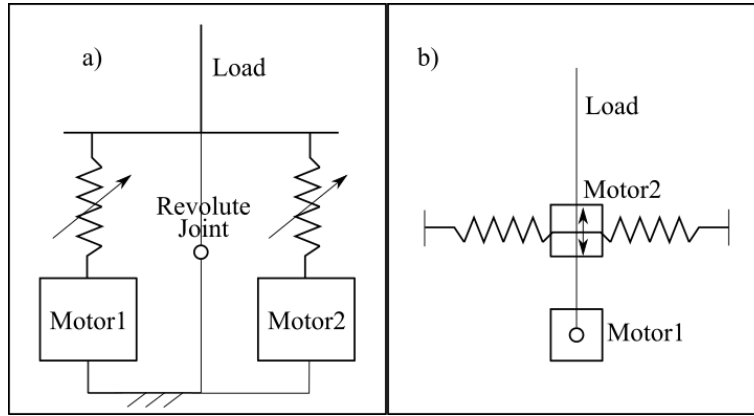


Figure 1.4 : Schematic representation of VSA types: a)Spring preload b) changing transmission between load and spring.

in various mechanisms. Even though it is not introduced in a VSA, rubber [67] and timing belt [68] is used as the source of elasticity.

Beyond the compliance, stiffness change is an essential notion to be able to complete some tasks that are expected from humanoids, such as walking and throwing a ball. Energy-efficient walking of bipeds is performed by utilizing compliant actuators on account of energy storing ability of the elastic component. Energy efficiency is a key concept for humanoid robots because of limited space that is left for batteries. In 1990, the impressive study of the research group in Leg Laboratory in Massachusetts Institute of Technology was a revolution to conventional biped walking methods [69]. Their mechanism could walk owing to its initial energy without any actuator or external energy injection. Although this may be true for stable conditions, when there is a change in walking speed or environment, to maintain the efficiency and the stability of the mechanism, it is expected to change its natural dynamics. Putting the two mechanisms side by side, one is fixed legged robot and the other is Edubot, a variable stiffness legged robot, having the energy cost decrease about 40% in running [70]. In a similar manner, compliance in the mechanism increases the distance in the case of ball throwing due to energy storage feature. In accordance to this, an optimal control strategy is implemented to the VSA mechanism to maximize ball-throwing distance [71]. Benefits of stiffness adjustment are presented in the study by comparing variable and fixed stiffness performances.

VSAs are superior to conventional actuators in terms of energy efficiency, safety in impact scenarios and potential sensor failures. Today, design and control of VSA is a very active research field in robotics, and the number of studies has been growing

rapidly [72]. A detailed analysis of the VSA designs in literature can be found in [61, 73–75].

1.2.5 Joint control and artificial intelligence

Feedback and feedforward are most common types of control which the system reacts the change in the environment automatically. In the feedback control technique, sensor measurement(s) are utilized to change and hold the control variable at a set value. Unlike feedback control, actions are taken in a pre-described way in feedforward control without caring how control variable reacts. In conventional control, these two techniques have applications that are used together, as well as applications that are used on their own. On the other hand, the researchers question which method is preferred by the human intelligence to carry out daily tasks. The existence of feedback control in human decision mechanism can be explained by referring the sensory organs in the muscles (i.e., [29]). On the other hand, the presence of the feedforward control in human control strategy was brought to light with inspiring studies in [76, 77]. In both studies, the movements of the human subjects are perturbed in a controlled environment, a rotating room and an unstable force field. As a proof of the existence of feedforward control, the subjects can adapt their motion trajectory to the changing environmental conditions. As a result, it can be said that human brain exploits both feedback and feedforward control.

Feedback control has been used in humanoid robots since the first design. In earlier stages of the humanoid robot history, position control is performed to complete manipulation or walking tasks via encoders. However, in last decades, the force control has gained importance due to increase in the requirement of interaction with unstructured environments. Two ways of force control are defined in [78]: passive and active force control, where the former is low-cost and simple, yet not suitable for industrial applications, latter is expensive and complicated. The passive force control is provided by the intrinsic properties of the joint mechanism which must include elastic elements between load and motor as given in the previous section. On the other hand, active force control requires additional force sensors. In [79], custom force/torque sensors are designed to lower the cost for joints of humanoid robot Icube. In addition to additional sensors, the algorithms are complicated and require precise

models of both the robot and the environment. The impedance control, which is one of the major algorithms, creates a virtual impedance and the system turns to be a mass-spring-damper system [80]. This method and derivatives of active force control are applied to many humanoid robot tasks such as walking [81], manipulation [21] and opening a door [82]. Although the successful applications are reported, dynamics based structures of the methods make it prone to be unstable according to modeling errors. Additionally, sensor failures and impact scenarios [83] are other failure modes which damage the HRI.

Feedforward control strategy is based on the knowledge of the system model instead of the variable measurements. Therefore, a model of the environment or the robot can be useful for this approach. For example, it is shown in [84] that humans can predict when to catch a falling ball as a result of their experiences with the Newton's Law. Accordingly, it requires semantic information retrieval from the environment. Similar to humans, humanoid robots can benefit experiences and increase the performance metrics of the desired tasks by using this information, especially in a visual way. In fact, computer vision is a well-established research area, and many studies are present. Despite the extensive effort in conventional techniques [85], accuracy and computation cost restrict to harvest semantic information from the images. On the contrary, a new algorithm, which is based on neural networks, a well-known feedforward method, have gained more interest recently. This new method is called as deep learning (DL), and the first example is published in 2012 [86] with a record-breaking accuracy to solve classification problem of 1.2 million images from 1000 classes. Afterwards, many great models are designed to carry the performance of classification one step further [87–89]. Besides the accurate results, DL algorithms are good candidates to be used in humanoid robots to acquire semantic information from various sources due to its similarity to human brain architecture [90].

In the previous sections, the benefits of the similarity between human and humanoid joints are explained. In addition to mechanical resemblance, the similarity in control strategy is a good step to close the gap between human and robot intelligence. As in humans, a combination of feedforward decision scheme can be exploited with a feedback control action.

1.3 Contributions of The Thesis

The main goal of the humanoid robotics research is to design robots which mimic the human motions as close as possible. In order to achieve this goal, both mechanical structures and control strategies should be inspired by humans while avoiding the increase in complexity and cost. In this thesis, new humanoid robot joint designs are presented considering the aforesaid requirements. Although the main focus is on the mechanical design, low-level control methodologies are given for each design. In addition to this, a high-level control approach is proposed as a case study. We believe that the study will contribute to humanoid robotics by introducing new ideas and will help to make today's robots one step closer to human-like robots. The major contributions of the thesis are summarised as follows:

- A 4 DOF cable-driven variable stiffness neck mechanism is introduced, and the mathematical models are derived. The mechanism combines the advantages of two different design approaches as given in [42, 43] and [27, 91–94]. Hence the shaft and the universal joint inside the mechanism constrain the motion which facilitates the calculations of kinematic and dynamic models without losing the compliance due to the presence of the helical spring. In addition, the mechanism introduces a new approach to adjust stiffness without additional components.
- An antagonistic 2 DOF cable-driven variable stiffness elbow/knee mechanism using variable radius pulleys is proposed. Despite the examples of antagonistic bi-directional VSA design in the current literature [62], use of VRP as nonlinear spring mechanism reduces the complexity and cost. Also, three VRP synthesis methods are detailed in order to design user-defined nonlinear spring mechanisms. To our knowledge, the synthesis methods are the first methods in the literature for translational VRP mechanisms. Besides the structural similarity to human muscles, three methods are shown to estimate external force/torque with regards to elastic element deflection as human muscles sense the external effects.
- Previous studies in literature mostly focused on single DOF VSAs. In this thesis, a 4 DOF VSA is designed which combines the advantages of cable-driven multi DOF joints and antagonistic VSA mechanisms. This mechanism is an advanced version of previous 2 DOF elbow mechanism. Instead of the revolute joint in the middle of

2 DOF system, a magnetic spherical joint is utilized which resembles the shoulder and hip joints in human.

- The stiffness adjustment ability brings new motion freedom which contributes the complexity of control. To choose correct stiffness value in the context of manipulation of an object, we proposed a methodology on contemporary object recognition techniques. The approach is similar to human manipulation system as having a combination of feedforward and feedback controls.

1.4 Thesis Outline

Following the introduction presented in this chapter, the thesis starts with the description of 4 DOF cable-driven variable stiffness neck mechanism in Chapter 2, where the kinematic/dynamic models are presented with the control approach. Next, in Chapter 3, 2 DOF elbow/knee mechanism which utilizes variable radius pulley mechanism as nonlinear spring. The synthesis methods of the nonlinear spring mechanism are detailed within the chapter. Additionally, three external force/torque estimation methods are applied to variable stiffness joint. Then, 2 DOF joint is improved, and DOF number is increased to 4 in Chapter 4. A stiffness adjustment method using the results of a visual recognition technique is used to adjust the mechanism stiffness in a case study in Chapter 5. Finally, the conclusion and the future works are drawn in Chapter 6.

2. NECK JOINT (CDPS) DESIGN AND ANALYSIS

In this section, a cable-driven, compression spring-supported hybrid mechanism is presented. The benefits of the proposed system are the special blend of various qualities of variable compliance, hybrid parallel-serial structure for better controllability and light-weight design. The mechanism can be used as a neck joint in humanoid robots due to smooth motion profile and resemblance to human neck joint structure. It can also be classified as an individually controllable joint module.

This new joint mechanism design combines two different design perspectives. In the first perspective, in order to imitate the spring-like behaviour of the human cervical vertebrae, it is replaced with a helical spring. Similarly, the muscles are substituted with cables which are pulled by electric motors [42, 43]. Accurate kinematic models of the given mechanism are difficult to compute unlike serial manipulators and also the control of such a mechanism is a difficult task. In the proposed CDPS mechanism, a two part shaft combined with a universal joint in the middle is placed co-centrally with the spring which is located between the top and bottom plates. The shaft in the middle serves as a series link and simplifies the computations of kinematics and dynamics. Moreover, the additional components allow transferring yaw motion directly. In some other research, a similar mechanism is designed without using a helical spring, resulting in a more stiff mechanism [27, 91–94]. On the contrary, the helical spring in the CDPS mechanism, which is proposed in this thesis, brings compliant behaviour alongside with the translational motion of the output plate on the upper part of the shaft.

A conventional helical spring exerts an opposing force proportional to its length change resulting in a linear force-length relation under compression effect. However, when a combined bending and compression loading is applied to spring, a nonlinear relation is formed between force/moment and the deflection. The nonlinearity is not necessarily a disadvantage. On the contrary, it is a desired behaviour in VSA design and to obtain the nonlinearity often in the state-of-the-art studies the

researchers make use of complicated mechanisms [61, 74]. In this chapter, the methodology of using the conventional helical springs as nonlinear spring mechanisms under bending and compression effects is detailed without using additional parts and complex mechanisms. Only a few studies analyse the effect of combined bending and compression on a helical spring, even though the spring is a widely used classical machine element. Shape memory alloys are used as actuators and two different mixture of bending and compression loading scenarios are considered in [95]. The first scenario is a single-side loading and the second one is pure bending. Both cases are solved based on Castigliano's Theorem. In this thesis, the spring is analysed numerically by using this theorem under combined effects of bending and compression.

This chapter is divided into 4 sections. The first section gives a general description and the main ideas in the concept of CDPS mechanism. The kinematic and dynamic models of the proposed mechanism are presented in the second and third section, respectively. In the final section, the experimental setup is introduced and the experimental results are reported with conclusions.

2.1 Description of Cable-Driven Parallel-Series (CDPS) Hybrid Mechanism

The proposed mechanism is comprised of two plates, a compression spring, two-part shaft, four cables and motors as shown in the CDPS mechanism drawing in Figure 2.1. The lower plate and the upper plate hold the compression spring in concentric position. The lower plate and the motors are fixed to the base and the upper plate position is adjusted by three cables that are pulled or released by which three servo motors located underneath the lower plate. Thus, the upper plate can rotate in two axes providing pitch and roll angles. The two-part shaft with a universal joint in the middle, which passes through the mechanism, and constrains the spring motion. The yaw motion which is defined the rotation about the longitudinal axis is obtained by a fourth motor transferring through the concentric shaft. In order to make the mechanism lightweight and remotely-actuated, all motors are encapsulated in an isolated box and can be installed at a far location from the joint. The mechanism may be classified as a parallel manipulator considering its closed-chain structure, yet the two-part shaft and the universal joint imposes serial kinematics which is reflected by serial mechanism properties. As a result of this, the mechanism is called as CDPS hybrid mechanism.

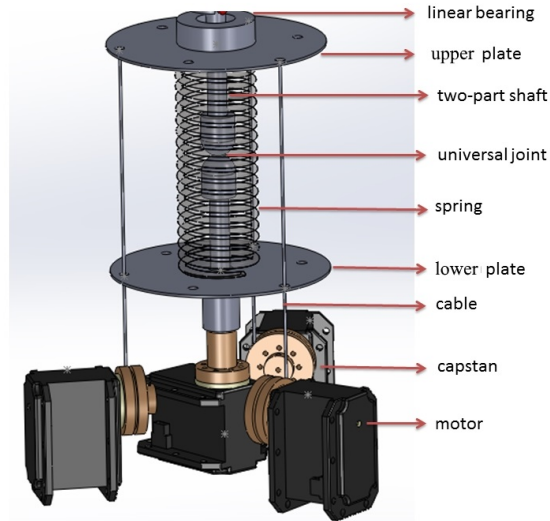


Figure 2.1 : CDPS mechanism and its components, with motors, bearings and capstans.

The mechanism has four DOF in total; three of them corresponds to pitch, roll and yaw motions. The last one is related to the stiffness adjustment capability, in other words, translational motion of the upper plate on the shaft. The pitch and roll motions are described as the rotations of the upper plate about the radial axes that are perpendicular to each other and placed on the shaft. The universal joint restricts these rotations which also helps easier kinematic and dynamic modeling. Unlike the pitch and roll motions, the yaw motion is actuated by a direct-drive motor and is not inherently compliant, for that reason this motion is not included in modelling and experimental sections. Nevertheless, the compliance can be integrated using a torsional spring to the shaft rotation at the lower plate when it is required. The last DOF is the upper plate translation on the shaft which is designed to change the combined stiffness of the mechanism in pitch and roll axes. In this mechanism, the stiffness control is achieved via a structure-dependent way without using extra mechanism.

2.2 Kinematic Model

In CDPS mechanism, the upper part of the shaft is connected to either an end effector or the successive link, for instance, a robotic head. Therefore, the motion of the upper shaft can be considered as the output motion of the mechanism. Since the output yaw motion is excluded from the analysis due to the aforementioned reasons, upper plate motions play a decisive role. Since the upper plate is pulled by the cables externally, it

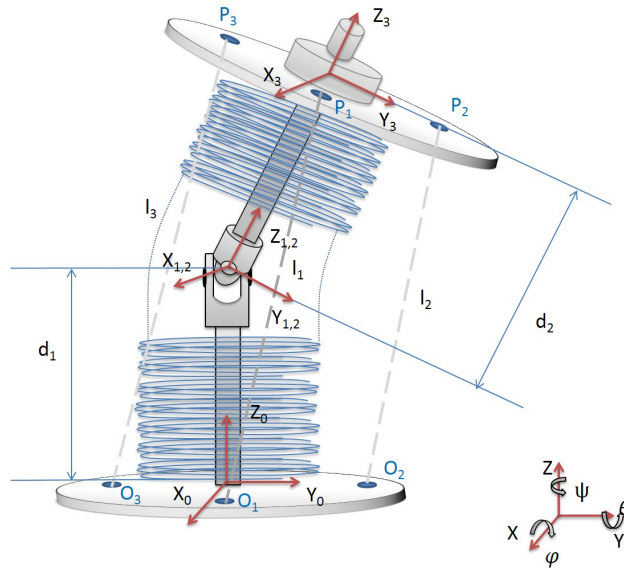


Figure 2.2 : Neck mechanism with variables, local and global axes, cable lengths, upper and lower plate cable assembly points.

defines the pitch and roll motions of the output shaft. In addition to these motions, the upper plate translational motion changes the compression on the spring. The motion of the upper plate affects helical spring and stiffness of the mechanism too. The pitch and roll (θ , ϕ) motions determine the bending angle of the compression spring where the bending center is forced to be the center of the universal joint by the restrictive geometry of the mechanism. Similarly, the compression amount of the helical spring is taken into account as the translational motion of the upper plate. Because the lower part of the shaft is at rest, the compression is measured by the distance (d_2) between the universal joint center and the upper plate. Therefore, the upper plate relative position to lower plate can be described by using three generalised coordinates and collected in a vector (\mathbf{q}), noting that the vectors are shown with bold symbols. The geometric variables used to derive kinematic model are illustrated schematically in Figure 3.4.

It is clearly seen in Figure 3.5 that the neck mechanism is an RRP structure with 3 DOF. The local frames (\mathbf{X}_1 , \mathbf{Y}_1 , \mathbf{Z}_1) and (\mathbf{X}_2 , \mathbf{Y}_2 , \mathbf{Z}_2) intersect and one of them is rotated by angle $\pi/2$ with respect to the other one. The distance d_1 is constant since the lower shaft is fixed to the lower plate.

The forward and inverse kinematic model can be obtained by using the given variable definitions. The motor shaft angles or the cable lengths (l_1 , l_2 , l_3) are the inputs and the pitch, roll angles and the translation of the upper plate (θ , ϕ , d_2) are the outputs in the forward kinematics. On the other hand, in the inverse kinematics, generalized

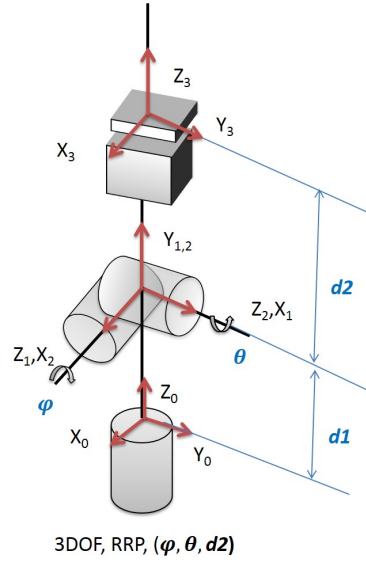


Figure 2.3 : Reduced serial kinematic model of neck mechanism with RRP structure (pitch, roll and translation).

coordinates are the inputs and the cable lengths are the outputs. Since the mechanism between the upper and lower plates is serial in RRP structure, transformation matrix between them can be written to derive kinematic equations. Three cable connection points on the upper plate ($\mathbf{P}_1, \mathbf{P}_2, \mathbf{P}_3$), which are located at $\pi/3$ intervals, define the upper plane. Similarly, evenly spaced three points ($\mathbf{O}_1, \mathbf{O}_2, \mathbf{O}_3$) in which the cables pass through on the lower plate defines the plane which can be used in geometric relations for the lower plate and the rest of the mechanism. The first component of the transformation matrix is the constant translation (Tr_1) of the fixed-length lower shaft. After the translation, the pitch and roll rotations are taken into account around the universal joint center. Finally, the translation of the upper plate is added to calculations. In equation (2.1), the transformations are given and when combined with the rotation matrix, the transformation matrix described between upper and lower planes is formed.

$$\begin{aligned}
 Tr_1 &= \begin{bmatrix} 1 & 0 & 0 & 0 \\ 0 & 1 & 0 & 0 \\ 0 & 0 & 1 & d_1 \\ 0 & 0 & 0 & 1 \end{bmatrix} \\
 Rot_1 &= \begin{bmatrix} c\theta & s\theta s\phi & s\theta c\phi & 0 \\ 0 & c\phi & -s\phi & 0 \\ -s\phi & c\theta s\phi & c\theta c\phi & d_1 \\ 0 & 0 & 0 & 1 \end{bmatrix} \\
 Tr_2 &= \begin{bmatrix} 1 & 0 & 0 & 0 \\ 0 & 1 & 0 & 0 \\ 0 & 0 & 1 & d_2 \\ 0 & 0 & 0 & 1 \end{bmatrix}
 \end{aligned} \tag{2.1}$$

$$T_{03} = \begin{bmatrix} c\theta & s\theta s\phi & s\theta c\phi & s\theta c\phi d_2 \\ 0 & c\phi & -s\phi & -s\phi d_2 \\ -s\phi & c\theta s\phi & c\theta c\phi & c\theta c\phi d_2 + d_1 \\ 0 & 0 & 0 & 1 \end{bmatrix} \quad (2.2)$$

Then, equation (2.3) is used to calculate the transformation matrix $\mathbf{P}_i = [P_{i,x}, P_{i,y}, P_{i,z}]^T$ via $\mathbf{O}_i = [O_{i,x}, O_{i,y}, O_{i,z}]^T$.

$$\begin{bmatrix} \mathbf{P}_i \\ 1 \end{bmatrix} = T_{03} \begin{bmatrix} \mathbf{O}_i \\ 1 \end{bmatrix} \quad (2.3)$$

The Euclidean distance between \mathbf{O}_i and \mathbf{P}_i is used in order to compute the relation between the cable lengths (l_1, l_2, l_3) and the upper plate position (θ, ϕ, d_2) . Any cable length can be calculated by the given expression in equation (2.4) according to this distance.

$$l_i = \sqrt{(P_{i,x} - O_{i,x})^2 + (P_{i,y} - O_{i,y})^2 + (P_{i,z} - O_{i,z})^2}, \quad (2.4)$$

where $i = 1, 2, 3$

When the exact position of the upper plate is calculated, the error f_i between the cable lengths and the points where the cables tied upon must be zero. The error function between the real length and the Euclidean distance between the points is given in equation (2.5).

$$f_i = l_i - \sqrt{(P_{i,x} - O_{i,x})^2 + (P_{i,y} - O_{i,y})^2 + (P_{i,z} - O_{i,z})^2} = 0 \quad (2.5)$$

Because of the nonlinearity in the error function, Newton-Raphson numerical method can be applied. The formula can be adapted to calculate any of the parameters when the rest of them is known/ predicted. The iterative method is expressed by the equation (2.6).

$$\mathbf{q}_k = \mathbf{q}_{k-1} - J^{-1}\mathbf{F} \quad (2.6)$$

The symbol $((\cdot)_k)$ shows the iteration step and \mathbf{q}_k is the vector of the generalized coordinates in k^{th} iteration step. The vector \mathbf{F} contains the nonlinear error function in equation (2.5). where J is the Jacobian matrix defined by equation (2.7) and \mathbf{q}_k is the k^{th} iteration of the solution for the vector of the generalised coordinates, while vector \mathbf{F} is formed by error equations of cable lengths f_i . The Jacobian matrix (J) is described by equation (2.7) which is calculated as follows:

$$J = \begin{bmatrix} \frac{\partial f_1}{\partial \theta} & \frac{\partial f_1}{\partial \phi} & \frac{\partial f_1}{\partial d_2} \\ \frac{\partial f_2}{\partial \theta} & \frac{\partial f_2}{\partial \phi} & \frac{\partial f_2}{\partial d_2} \\ \frac{\partial f_3}{\partial \theta} & \frac{\partial f_3}{\partial \phi} & \frac{\partial f_3}{\partial d_2} \end{bmatrix} \quad (2.7)$$

If desired generalized coordinates are known, then the calculation of the necessary cable lengths become a simple task via equation (2.5). In addition to this, a reduced kinematic model is presented which minimizes the spring compression. Rather than the generalized coordinates vector, this model takes only orientation inputs into account and calculate necessary cable lengths with the assumption of one of the cables is fixed at its initial length. In fact, when the stiffness change is neglected, system DOF reduces to 2, thus it can still be assumed as a fully actuated system with two cables. In this method, first, the idle cable is detected according to the motion command. Then the iterative solution technique is performed to find remaining cable lengths by using the simplified Jacobian matrix given in equation (2.8).

$$J = \begin{bmatrix} \frac{\partial f_1}{l_2} & \frac{\partial f_1}{l_3} & \frac{\partial f_1}{d_2} \\ \frac{\partial f_2}{l_2} & \frac{\partial f_2}{l_3} & \frac{\partial f_2}{d_2} \\ \frac{\partial f_3}{l_2} & \frac{\partial f_3}{l_3} & \frac{\partial f_3}{d_2} \end{bmatrix} = \begin{bmatrix} 0 & 0 & \frac{\partial f_1}{d_2} \\ 1 & 0 & \frac{\partial f_2}{d_2} \\ 0 & 1 & \frac{\partial f_3}{d_2} \end{bmatrix} \quad (2.8)$$

To have a better insight into the reduced kinematic model, Figure 2.4 can be referred. In the figure, the top view of the lower plate and the O_i points are shown. The lower plate is split into three areas with virtual lines which are drawn between the center and the circumferential points. These areas are used to determine the idle cable by looking at the desired pitch and roll motion vector. Two cables around the motion vector are marked as moving cables for that case, whilst the opposite one is fixed and is set to default value. As an illustration, a motion vector \mathbf{E} , corresponding to 30° rotation in both pitch and roll axes, is drawn to show the direction of motion. The neighboring cables to this vector are cable-1 and cable-3, therefore these cables are selected as moving cables. After this selection, the pulling amount of cables required to obtain desired motion is calculated by using equation (2.7) and (2.8). The other cable is retained at the default position.

The humanoid neck platform is implemented and all the experiments in this chapter are performed on the setup. The physical parameters used in the setup are given in Table 2.1. In order to achieve a realistic workspace, these parameters are fed into the reduced forward kinematics algorithms. Thus, by holding one cable length constant, the translational position of the upper plate center point and the orientation of the upper plate with respect to the global frame on the lower plate are calculated. The algorithm is repeated to include the idle condition for every cable at (95 mm) while changing the other two within 50-95 mm range, as given in Figure 2.5. As a result of workspace

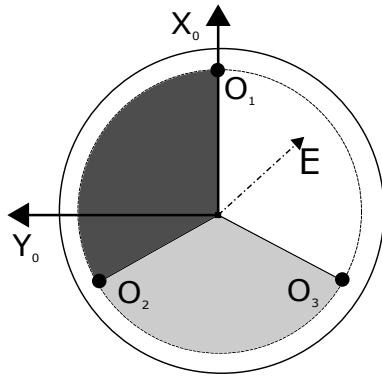


Figure 2.4 : Top view of the lower plate and an example motion command vector.

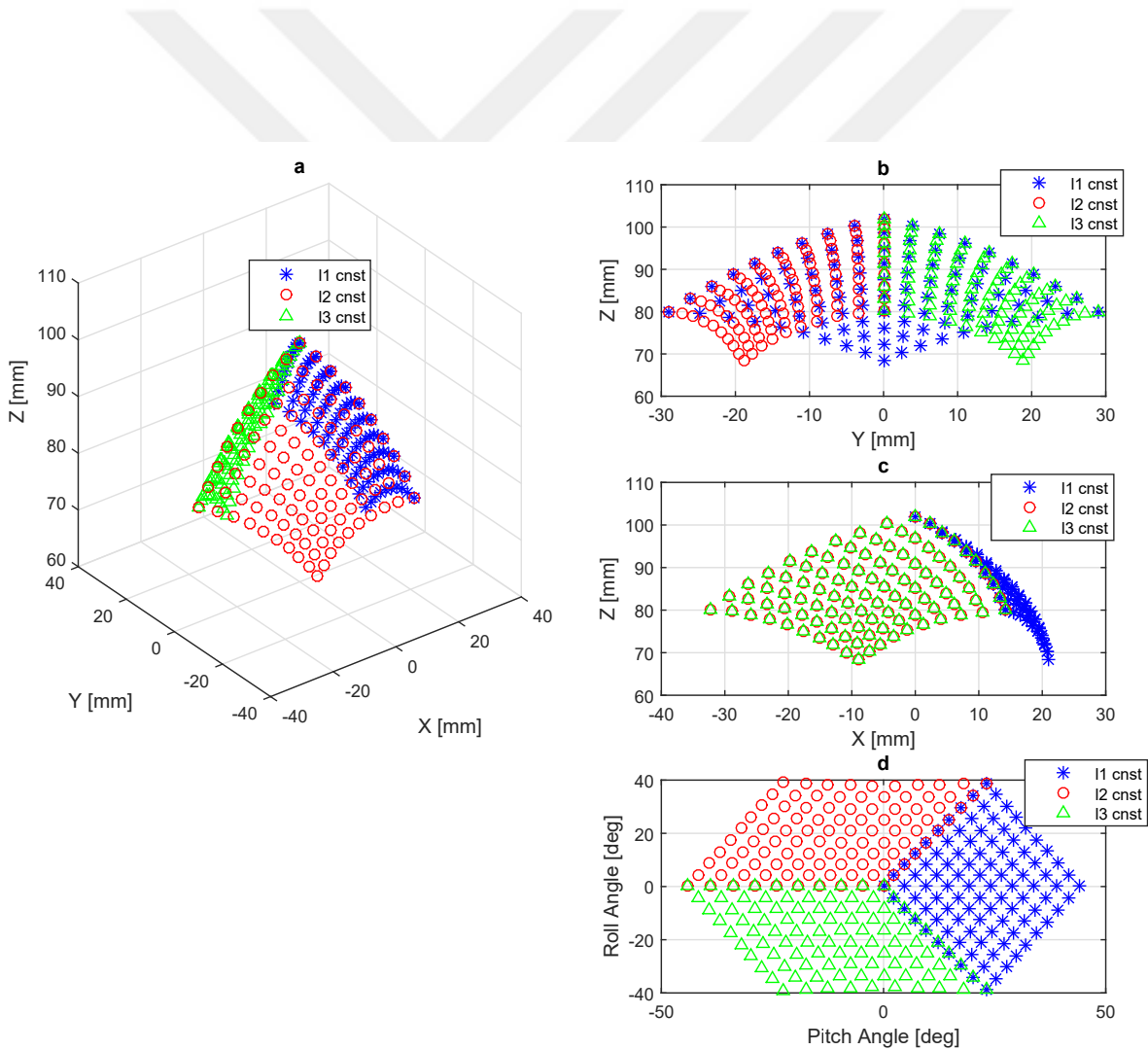


Figure 2.5 : Workspace of the proposed mechanism in a) 3D b) Y-Z c) X-Z view d) Pitch and Roll Angles.

Table 2.1 : Simulation parameters in workspace analysis.

Variable	Value [unit]
Lower shaft length d_1	47 [mm]
Length of constant cable	95 [mm]
Distance between lower plate center and O_i points	40 [mm]
Distance between upper plate center and P_i points	40 [mm]

analysis, the position of the upper plate center is given in Figure 2.5, where three different colors and symbols are used to show distinct cases of idle cables. Figure 2.5.(b) and Figure 2.5.(c) show Y-Z and X-Z views of the same figure, respectively. The symmetrical distribution in Y-Z plane with respect to X-axis is caused by the symmetrical location of the cable 2 and 3. Conversely, only cable 1 is located on the X-axis which results in an asymmetrical distribution on X-Z plane. Therefore, both in positive and negative directions, pure roll motions requires the cables 2 and 3 to be pulled. Although cable 1 is adequate for positive pitch motion, two cables are needed for negative roll motions. The final part of the Figure 2.5 shows the range of motions (ROM) in pitch and roll axes.

In spite of the fact that, in [96], the human neck ROM varies from individual to individual in regards to their ages, genders and physical traits, average values for pitch (flexion-extension), roll (lateral bending) and yaw (axial rotation) axes are stated as 60° , 40° and 80° . However, a limited amount of the full motion is employed to fulfill daily tasks as given in [97]. It can be seen from the Figure 2.5.(d) the proposed neck joint is able to rotate between -30° and 30° yielding 60° in total in pitch and roll axes. The limiting factors for the ROM are the strength of the cables and the stall torque of the motors. Another limiting factors comes from the construction as the lower plate blocks physically the upper plate after a certain rotation. All in all, despite the motion limits of the mechanism, cannot fulfil the full ROM of an average person, which is the major disadvantage of the joint, its ROM is sufficient to complete human daily tasks.

2.3 Dynamic Model

The dynamic model of the mechanism derived in this section uses the kinematic relations obtained in the previous section. To derive the dynamic model firstly 3D geometric model is simplified to 2D due to its symmetric structure. As a result of

the simplification, the pitch and roll motions are reduced to pure bending without any information loss, thus the motion of the mechanism is degraded to bending and translation (compression according to spring). Secondly, the helical spring is analysed under combined bending and compression case. The reaction force and moment of the spring are calculated by using Castigliano's Theorem. Finally, the cable tensions, the spring reactions and the inertial forces of the mechanism are taken into account to build the complete dynamic model.

2.3.1 Dimension reduction of the model

Despite the fact that the pitch and roll motions are two distinct rotations about X_0 and Y_0 axes, their effect is combined and it can be considered as bending. Hence, these two rotations can be formulated so that the bending is computed as a resultant motion in order to simplify the analysis of the spring. To accomplish this task, two different Euler angles conventions are employed as illustrated in Figure 2.6. In the first place, two rotations about X_0 and Y_0 axes are defined in Euler (X-Y-Z) convention which implies the pitch and roll angles. After this definition, the same orientation of the upper plate is achieved by Euler (Z-X-Y) convention. Therefore, X_0 - Y_0 frame is rotated about Z_0 axis resulting a new rotation axis Y_{new} . The motion around the new axis is called as bending and denoted with ρ . Great care must be taken that both the pitch and roll rotations have this bending effect in the spring, but the rotation about Z_0 have no influence on the spring. Thus, in the second convention, only second rotation characterize spring reactions. Because the total number of parameters is retained same, there is no information loss due to this operation.

2.3.2 Helical spring analysis

After expressing three motions with two parameters which have an influence on the helical spring, we can now analyse the helical spring. The general assumptions of this analysis are that the bending effect that occurs under the compression load on the helical spring rather than causing buckling. The other assumption is that the cables have constant lengths.

The purpose of the analysis is to find the relation between the compression force / the bending moment and the deflection / bending angle, i.e. the stiffness of the helical

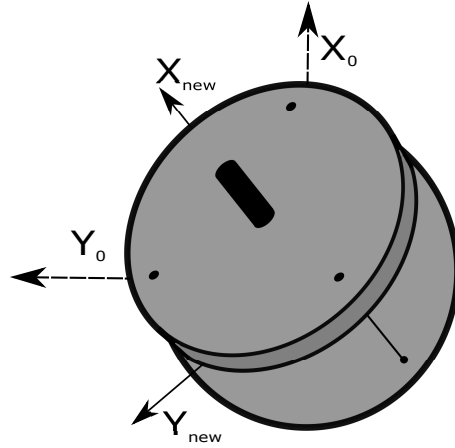


Figure 2.6 : Dimension reduction operation from the top view.

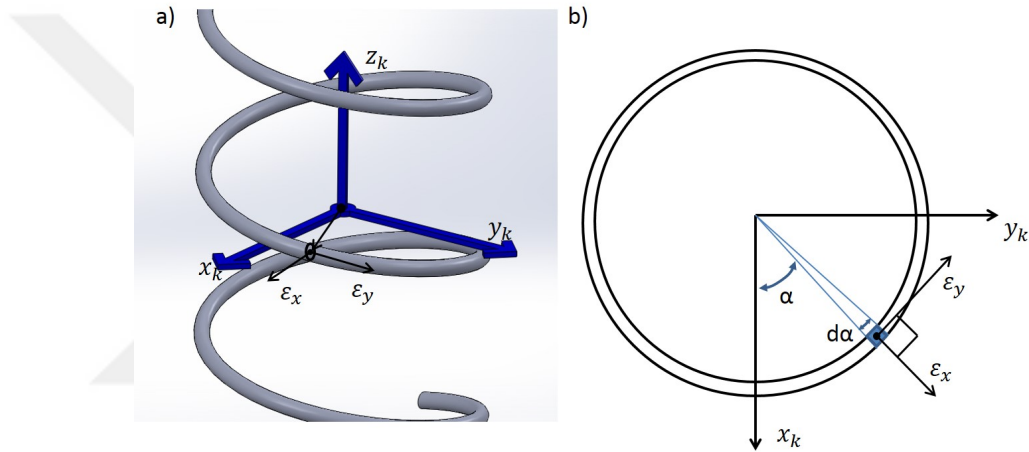


Figure 2.7 : a) Local frames on spring and infinitesimal element b) Top view of a spring coil.

spring. Since there are two parameters on both side, the stiffness is no longer expressed with a scalar, but a 2x2 matrix. To obtain the stiffness matrix, a similar approach is employed as in [98] where each coil is treated separately. Beyond the decomposition of the coils, each coil is divided into infinitesimal elements, too.

The frame $x_k y_k z_k$ is attached to the bottom center of each coil where k denotes the coil number starting from the bottom and increasing to the top. The total bending is divided into equal parts and reflected the z_k axes of each coil. The origin of every coil is shown by \mathbf{N}_k . As well as coils, 2D frames are defined on infinitesimal elements of which to define strength properties. The vector $\boldsymbol{\varepsilon}_x$ is placed on the tangential direction and the vector $\boldsymbol{\varepsilon}_y$ is placed on normal direction. The frame and variable definitions which are utilized in the analysis are shown in Figure 2.7.

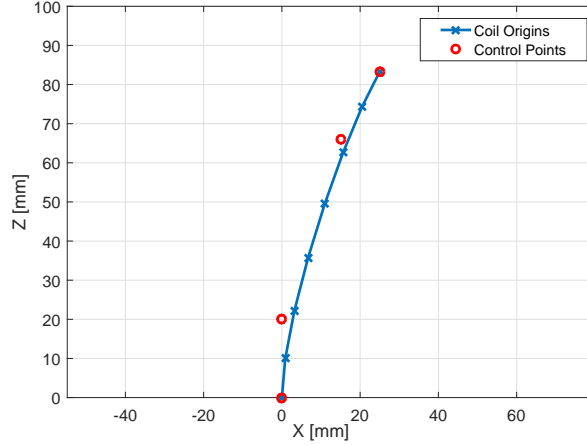


Figure 2.8 : Coil origins and control points of Bezier curve.

Cubic Bezier Curves are used to calculate the curve of coil origins. The starting and ending control points (C_0 and C_3) are defined at the origin points of the lower and upper planes. The other two control points (C_1 and C_2) define start and end directions of the curve which are selected as arbitrary points on the direction of normal vectors of the lower and the upper plates. Four control points are calculated as given in equation (2.9).

$$\begin{aligned}
 C_0 &= [0 \ 0]^T \\
 C_1 &= [0 \ \frac{d_1}{2}]^T \\
 C_2 &= [d_2 - \frac{d_1}{2} \cos(\frac{\pi}{2} - \rho) \ d_1 + d_2 \sin(\frac{\pi}{2} - \rho)]^T \\
 C_3 &= [d_2 \cos(\frac{\pi}{2} - \rho) \ d_1 + d_2 \sin(\frac{\pi}{2} - \rho)]^2
 \end{aligned} \tag{2.9}$$

Then the coil origins can be calculated as follows:

$$\begin{aligned}
 N_k &= (1 - v_k)^3 C_0 + 3(1 - v_k)^2 v_k C_1 + 3(1 - v_k) v_k^2 C_2 + v_k^3 C_3 \\
 &\text{for } k = 1, 2, \dots, 8
 \end{aligned} \tag{2.10}$$

The variable v_k is a vector between 0 and 1 and divided equally into n parts. Control points and all coil origins are given for an arbitrary (30°) bending in Figure 2.8. After obtaining the curve, the strength of infinitesimal elements on the spring can be formulated. The tensions on cables which pull the upper plate from different directions are denoted by \mathbf{T}_1 , \mathbf{T}_2 and \mathbf{T}_3 . These unidirectional tensions can be simplified to a generalized forces definition. Since there are two degrees of freedom in motion, i.e. the bending and the compression, generalized forces are defined in the same axes. Therefore, the equivalent forces are described as \mathbf{F}_{eq} in \mathbf{z}_{n-1} direction and moment \mathbf{M}_{eq} around \mathbf{x}_{n-1} axis. To calculate the effects of the equivalent force on the bending

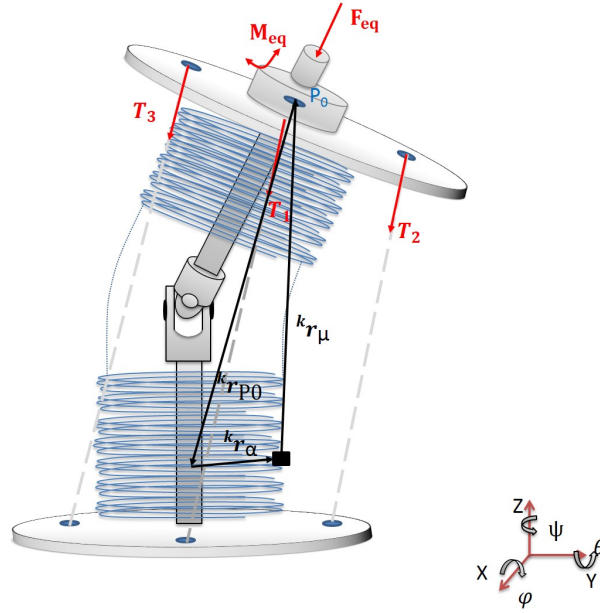


Figure 2.9 : Spring and cable forces acting on the mechanism.

angle, the distance between origins of the upper plate and the infinitesimal elements are defined. The position vector of the upper plate origin point P_0 with respect to frame k is represented as ${}^k\mathbf{r}_{P_0}$. The position of an infinitesimal element ' μ ' on k^{th} coil of the spring, ${}^k\mathbf{r}_\mu$, is defined as in equation (2.11),

$${}^k\mathbf{r}_\mu = {}^k\mathbf{r}_\alpha + {}^k\mathbf{r}_{P_0} \quad (2.11)$$

where ${}^k\mathbf{r}_\alpha$ is the position vector of the infinitesimal element in the particular coil and is defined as given in Eq. 2.12.

$${}^k\mathbf{r}_\alpha = \begin{bmatrix} R\cos(\alpha) \\ R\sin(\alpha) \\ \frac{N_{k+1,z} - (N_{k,z})\alpha}{2\Pi} \end{bmatrix} \quad (2.12)$$

The effect of the equivalent force on bending, which is acting on the element μ , is calculated by using the moment vector, ${}^k\mathbf{M}_\mu$, as follows:

$${}^k\mathbf{M}_\mu = {}^k\mathbf{r}_\mu \times {}^k\mathbf{F}_{eq} \quad (2.13)$$

As a result, the total moment acting on the element (${}^k\mathbf{M}_{\mu t}$) can be computed as given in equation (2.14).

$${}^k\mathbf{M}_{\mu t} = {}^k\mathbf{M}_\mu + {}^k\mathbf{M}_{eq} \quad (2.14)$$

The infinitesimal element specific frame $\varepsilon_x\varepsilon_y$ is taken into account in order to use Castigliano's Formula. The moment is transformed into the element specific frame

after a rotation α about \mathbf{z}_k axis is performed. The resulting moment vector (${}^k\mathbf{M}_c$) is calculated as in equation (2.15).

$${}^k\mathbf{M}_c = Rot_z(\alpha){}^k\mathbf{M}_{\mu t}. \quad (2.15)$$

The energies are calculated by using the Castigliano's Theorem for bending in two axes ($(U_{b1})_k, (U_{b2})_k$) and torsional ($(U_t)_k$) strain which are given in equation (2.15). The symbols E and G stand for the material specific strength properties, modulus elasticity and shear modulus. The geometry of the helical spring such as area moment inertia, polar moment inertia, and radius are represented by $I, J,$ and R_{spring} , respectively.

$$(U_{b1})_k = \int_0^{2\Pi} \frac{({}^k\mathbf{M}_{c,y})^2}{2EI} R_{spring} d\alpha \quad (2.16)$$

$$(U_{b2})_k = \int_0^{2\Pi} \frac{({}^k\mathbf{M}_{c,z})^2}{2EI} R_{spring} d\alpha \quad (2.17)$$

$$(U_t)_k = \int_0^{2\Pi} \frac{({}^k\mathbf{M}_{c,x})^2}{2\bar{G}J} R_{spring} d\alpha \quad (2.18)$$

Equation (2.20) gives total strain energy $((U)_k)$ for a single coil. Total strain energy (U) is the sum of the total strain energies of all coils and calculated as in equation (2.20).

$$(U)_k = (U_{b1}) + (U_{b2}) + (U_t)_k \quad (2.19)$$

$$(U) = \sum_{k=0}^{n-1} (U)_k \quad (2.20)$$

The compression distance Δd_2 and the 2D bending angle ρ is calculated by the derivation of the strain energies with respect to equivalent force and moment according to Castigliano's Theorem:

$$\Delta d_2 = \frac{\partial(U)}{\partial F_{eq}} \quad (2.21)$$

$$\rho = \frac{\partial(U)}{\partial M_{eq}} \quad (2.22)$$

Finally, the 2x2 stiffness matrix of the helical spring can be written in given form in equation (2.22).

$$\begin{bmatrix} F_{eq} \\ M_{eq} \end{bmatrix} = [K] \begin{bmatrix} \Delta d_2 \\ \rho \end{bmatrix} \quad (2.23)$$

To form a look-up table for 2x2 stiffness matrix, Δd_2 and ρ are swept in a range of 0-32 mm and 0° and 40° with increments of 1 mm and 1° . All the parameters used in the analysis are given in Table 2.2. The numerical values are obtained with the help

Table 2.2 : Simulation parameters in helical spring analysis.

Variable	Value [unit]
Compression distance Δd_2	0, 1, 2...30 [mm]
Bending angle ρ	0, 1, 2...40 [°]
Spring wire radius r	0.75 [mm]
Spring radius R	8 [mm]
Material	ASTM A227

of Matlab Symbolic Toolbox. The analysis results are given in Figure 2.10 according to the definition given in equation (2.24). It is worth noting that the elements K_{12} and K_{21} are the same due to the symmetry in the stiffness matrix. Therefore, instead of showing both of them in the figure, only one of them is given.

$$[K] = \begin{bmatrix} K_{11} & K_{12} \\ K_{21} & K_{22} \end{bmatrix} \quad (2.24)$$

K_{11} and K_{22} are the relations between compression-reaction force and bending-reaction moment of the spring. On the other hand, K_{12} and K_{21} , are equal because of the symmetry of the stiffness matrix, express cross relations between compression-reaction moment and bending-reaction force. When bending angle is zero, it is assumed to be a singular position for stiffness change, because the stiffness does not vary with the change in translational motion, according to the Figure 2.10. For constant bending angle, increasing values of compression reduces all the elements of the matrix. Therefore, compression makes spring softer. For constant compression, bending has similar affect. However, the spring gets stiffer for rotation with increasing values of bending angle due to K_{11} . Bending angle affects stiffness of the mechanism. In spite of the fact that the translational motion of the upper plate adjusts stiffness, bending angle of the mechanism has more effect on the stiffness. However, the stiffness of the mechanism is adjustable, because the compression also changes the stiffness.

Experimental validation of the stiffness value is a challenging task due to lack of direct measurement techniques. To overcome this problem, Finite Element Analysis (FEA) which is a proven and prevalent tool, especially in structural mechanics. Therefore, the results which are given in this section is compared to the results of FEA method which is implemented in Ansys software. The upper and lower plates are set as rigid components to isolate their elasticity effects from the spring. Besides, the spring is

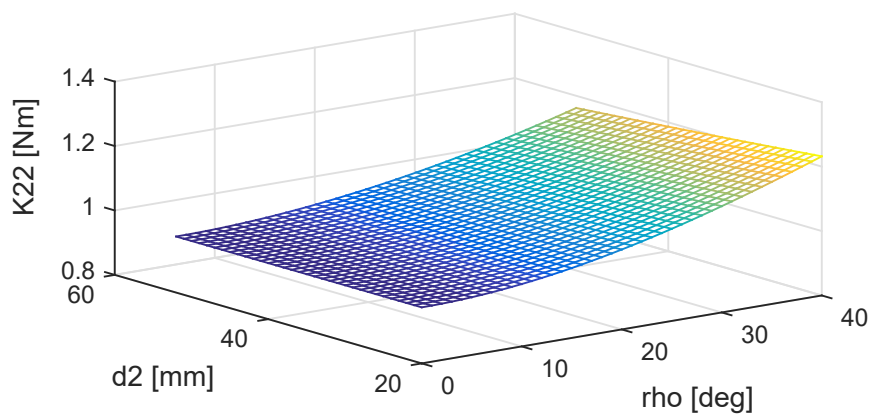
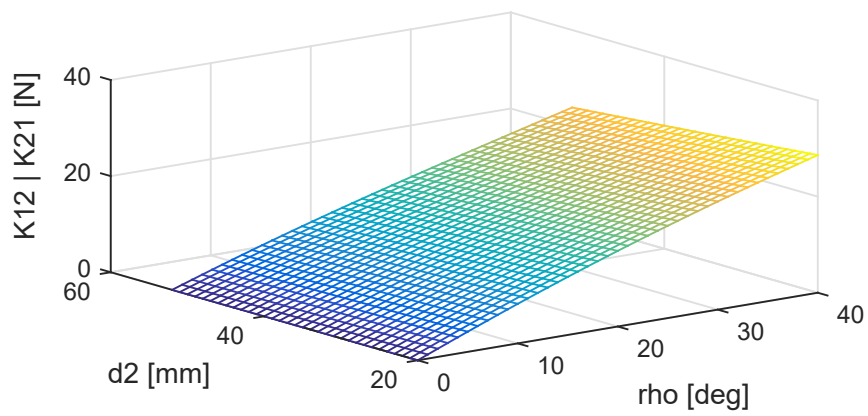
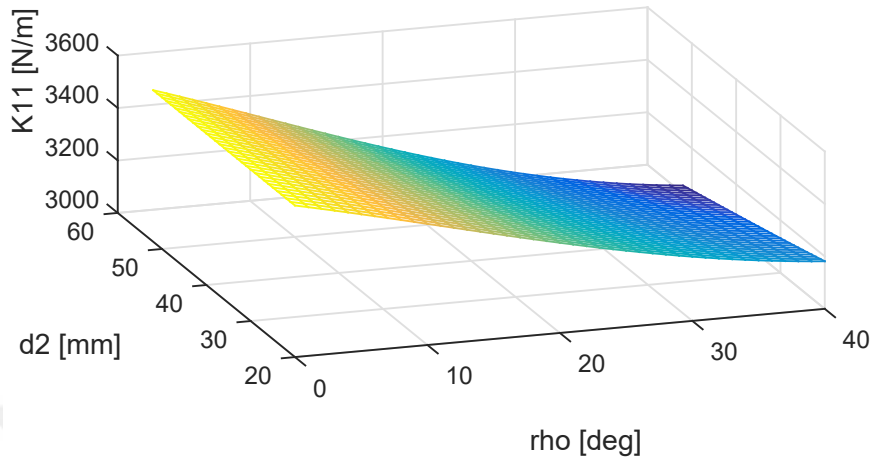


Figure 2.10 : Stiffness matrix change with respect to bending angle and compression length.

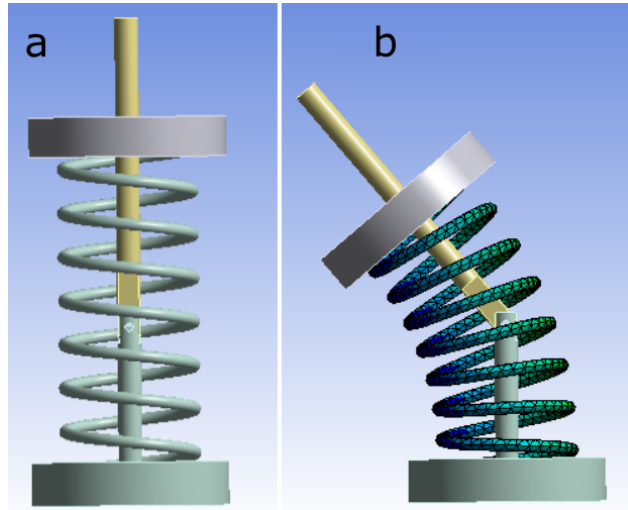


Figure 2.11 : The models of the mechanism in finite element analysis a) initial b) deformed.

fixed to both plates. Revolute and prismatic joints are defined between the upper-lower shaft and upper shaft-plate, separately. Initial position excludes all deformations and the simulation starts at the free-length of the spring. Then 10 mm compression and 40° bending are applied at the same time. Consequently, the reaction forces and moments are obtained, and they are compared with the results which were obtained from the proposed analysis technique. The set of values obtained from dynamic analysis and from FEA are shown together in Figure 2.12. Also, the images of initial and deformed shapes with meshes from the FEA software are given in 2.11.a and 2.11.b. In Figure 2.12 the results of the proposed method and the FEA are plotted with red and blue. Since the bending and compression motions are applied at the same time, with a ramp function, they are shown both on the x-axis in mm and degree units. The reaction forces obtained from both methods are plotted in Figure 2.12.a. and the mean difference is calculated as 2.2%. Similarly, the reaction moment plots are given in Figure 2.12.b and the proposed method yields an error of 1.5%. However, at the beginning of simulation, there is a convergence problem occurs in FEA analysis. It can be inferred from the figures that a quadratic relation arises for both the force and the moment when the combination of bending and compression loads are applied to a linear helical spring without the use of any additional mechanism.

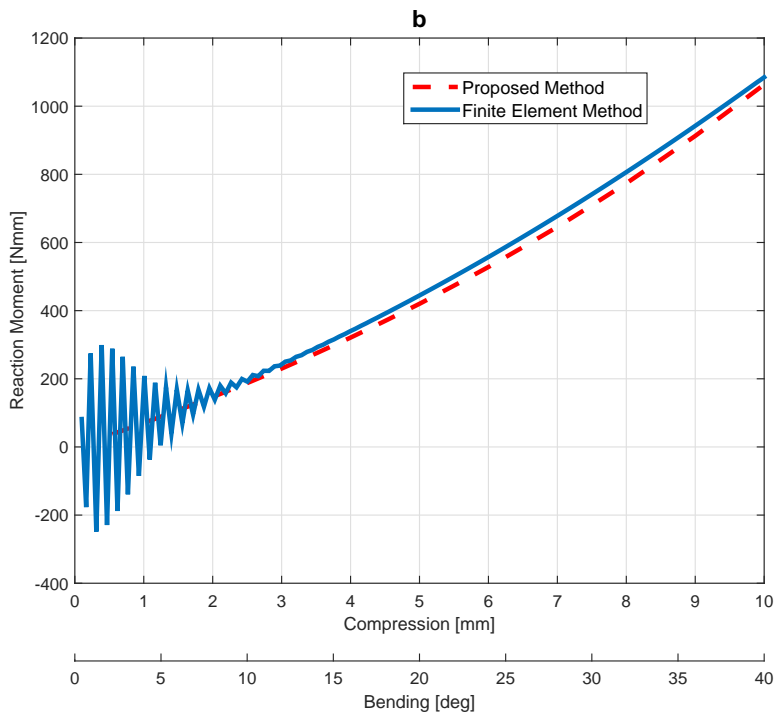
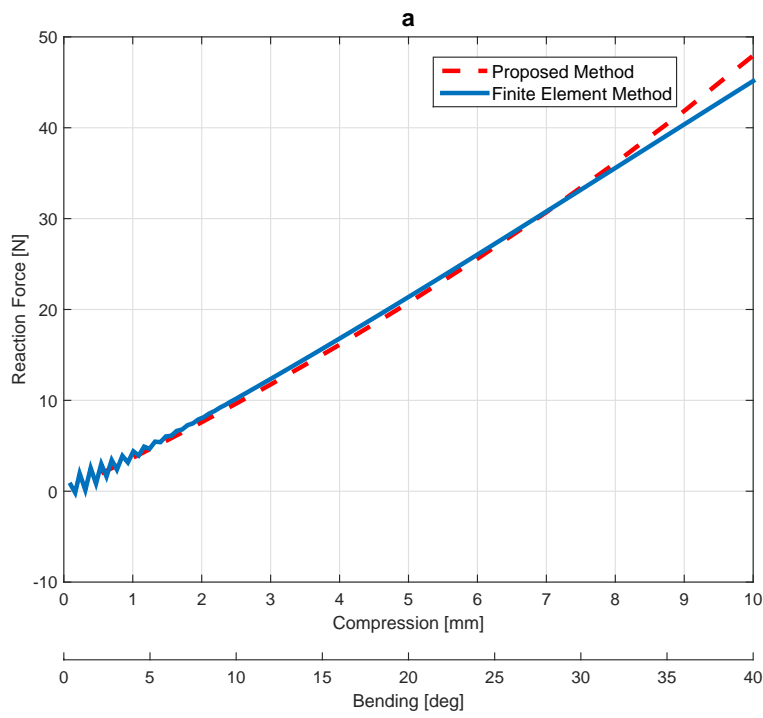


Figure 2.12 : Behaviour of the spring under compression and bending effects a) Reaction force b) Reaction moment.

2.3.3 Complete dynamic model

The equation of motion of a serial manipulator is described as in equation (2.25).

$$M(\mathbf{q})\ddot{\mathbf{q}} + C(\mathbf{q}, \dot{\mathbf{q}})\dot{\mathbf{q}} + G(\mathbf{q}) = B(\mathbf{q})\mathbf{T} + \mathbf{F}_s(\mathbf{q}) \quad (2.25)$$

The vector \mathbf{q} is the generalized coordinates vector $[\theta, \phi, d_2]^T$, $\dot{\mathbf{q}}$ and $\ddot{\mathbf{q}}$ are the velocity and acceleration vectors, respectively. M is the mass matrix, C includes Coriolis and centrifugal forces and G is the gravity matrix. There are no motors connected joints directly. Cable tensions are taken into account with a mapping matrix B which is given in equation (2.26). \mathbf{F}_s is the generalized force vector of helical spring and \mathbf{s}_i is the unit vector on the i^{th} cable direction. The variables $P_{i,x}$, $P_{i,y}$, $P_{i,z}$ are the positions of connection points of upper plate and each cable.

$$B(\mathbf{q}) = \begin{bmatrix} s_{1,z} & s_{2,z} & s_{3,z} \\ -P_{1,z}s_{1,y} + P_{1,y}s_{1,z} & -P_{2,z}s_{2,y} + P_{2,y}s_{1,z} & -P_{2,z}s_{2,y} + P_{2,y}s_{2,z} \\ P_{1,z}s_{1,x} - P_{1,x}s_{1,z} & P_{2,z}s_{2,x} - P_{2,x}s_{2,z} & P_{2,z}s_{2,x} - P_{2,x}s_{2,z} \end{bmatrix} \quad (2.26)$$

2.4 Experiments and Results

The performance of the proposed mechanism is evaluated through the experiments in which the mechanism performs a certain motion pattern which is controlled by an algorithm/schema based on the kinematic model. In order to perform the experiments, first, the mechanism is mechanically implemented. In the experimental setup, the mechanical construction and the components are introduced. The electronic components such as sensors, microprocessors are presented together with the control algorithm. In section 2.4.2, the experiment is detailed and performance is analysed in terms of kinematic and dynamic models.

2.4.1 Experimental setup

The mechanical construction of the mechanism is retained as simple as possible and implemented with ubiquitous components. The mechanism is constituted using these machine elements: the upper/lower plates, cables, two-part shaft, the helical spring, the revolute joint. The plates are made of Aluminum (7075) material while the material of the shaft is specified as chromed steel (AISI E 52100) in order to increase wear resistance against the linear bearing motion. The actuation is provided by four Robotis Dynamixel MX-28 motors with 2.5 Nm stall torque at 12 V. One of the motors are

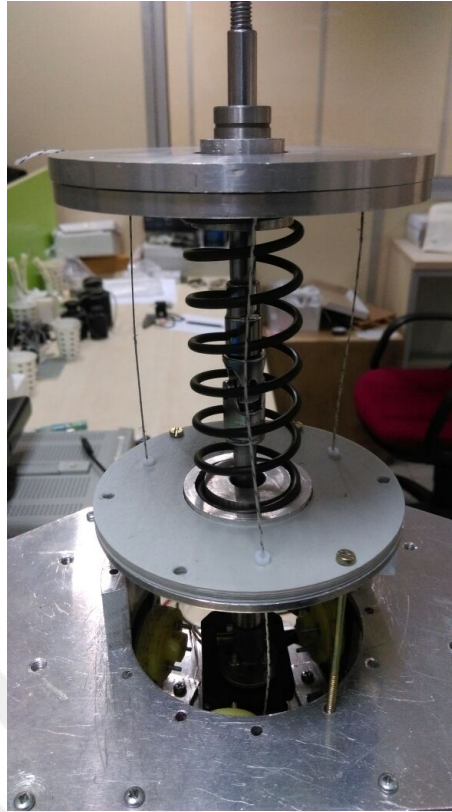


Figure 2.13 : UMay neck mechanism.

directly coupled to the shaft and drives in the yaw axis. The other three motors provide the motion by pulling the cables via 14 mm capstans on their shafts. Even though the cables are made of fishing lines with 0.5 mm radius, they can carry 100 N payload. PFTE tubes are assembled to the holes through which the cables pass on the lower plate. In addition to the picture in Figure 2.13, a video of the experiment is uploaded to the journal website as supplementary material [99]. The motions in the video contain randomly selected pitch and roll combinations. Although the translation motion in starting position (zero-position) has no influence neither on stiffness nor on the orientation, it is highlighted in the video for the demonstration purposes. To achieve this motion, three cables are pulled with same rate and amount synchronously.

There are two measurement units in the experimental setup. The first one is Razor 9 DOF inertial measurement unit (IMU) which gives the orientation of the upper plate and utilised as a truth table. The other measurement units are the encoders of Dynamixel motors. The data which is collected from these encoders are fed back to the control system. Therefore, the orientation of the mechanism can be estimated by using the motor positions and the forward kinematic model. At the end of the experiment, the estimated values are compared with IMU readings to validate kinematic models.

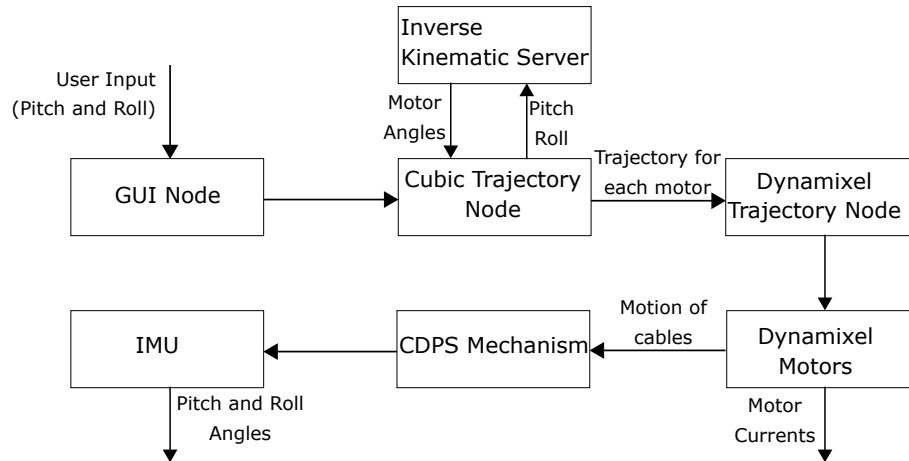


Figure 2.14 : Control structure used in experiments.

A kinematic-model based position control scheme is implemented in Robot Operating System (ROS) to drive the mechanism to reach the desired orientations. A graphical user interface (GUI) node gathers the desired orientation from the user. Then, the orientation commands are evaluated by the cubic trajectory node which enquires the necessary motor angles from inverse kinematic server. The simplified inverse kinematic model is executed herein and the resulting motor angles are sent back to cubic trajectory node. The cubic trajectory node calculates a third order polynomial to reach the desired motor angles smoothly. The total trajectory time is assigned as 2 seconds for each trajectory which is a feasible amount of time for given workspace and motors. Finally, the calculated trajectory is transferred to Dynamixel trajectory node which transforms the commands into motor motion. The position control scheme is given in Figure 5.3.

2.4.2 Results

The results which are given in this section are taken from the same experiments, which makes all the figures in this chapter comparable or related. The focus of the results is on the pitch and roll motions and their relevant motor control. The motions on yaw axis are not considered because the stiffness and the motion of the upper plate are not affected. The experiment is conducted for 80 seconds which is an arbitrary long enough time period to validate the kinematic and dynamic models and the position control performance in terms of orientation error. The user sends random orientation commands that are consistent with the ROM via GUI. The experiments are evaluated from two different perspectives. Firstly, the motor positions are fed into forward

kinematics and the orientation of the upper plate is estimated which are compared with the IMU measurements to validate the kinematic model. This experiment also shows the accuracy of the motion controller. Secondly, the cable tensions are estimated by using the inverse dynamic model. The same estimation is computed with the help of motor currents and two datasets are compared to verify the dynamic model.

The orientation results of the experiment are given in Figure 2.15 in pitch and roll axes including IMU (blue line), forward kinematic outputs (green dot) and user commands (red dash). As it can be seen from the figure, the user commands are randomly generated step functions. It can be interpreted that the upper plate can follow the desired orientation trajectory smoothly while preserving the stiffness at the minimum level. Furthermore, both the tracking results and the forward kinematics outputs are similar to IMU results which verifies the kinematic models.

Three cable tensions during the experiment are estimated from both the inverse dynamic model and the motor currents. The kinematic quantities are fed to the inverse dynamic model and the cable tensions are calculated. Moreover, Dynamixel motors provide load information to the user with regards to current levels consumed for the motion. Two estimation results are compared to validate the dynamic model as can be seen in Figure 2.16. The general behaviours of these data are similar for each motor, but there are errors in particular areas. Three reasons can be listed to explain the areas in which the error is higher. First, the motors are driven by the way of pulse width modulation (PWM) which induces noisy current readings. Second, the friction in the gearbox and between the cable and the PTFE parts are neglected in the inverse dynamic model, however, in the experiment, their effects cannot be ignored which contributes the error. Finally, DC motors have no load current which is not taken into account in this estimation.

2.5 Conclusion

A cable-driven parallel-series hybrid variable stiffness joint mechanism is presented in this section. First, the mechanism and the working principles are explained. Next, the kinematic analysis both in full and simplified forms are given considering the mechanism as a serial manipulator. Furthermore, the workspace of the mechanism computed and drawn utilizing the forward kinematics. After derivation of the

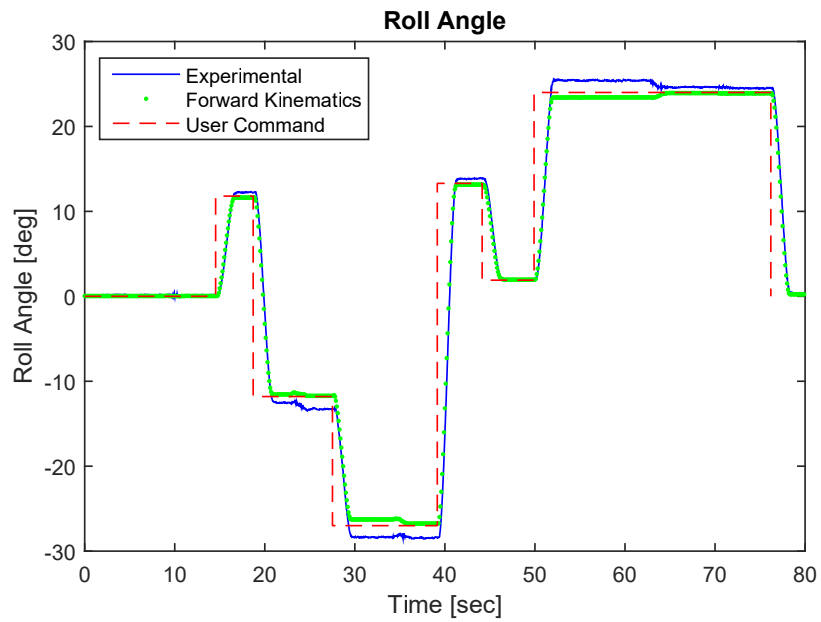
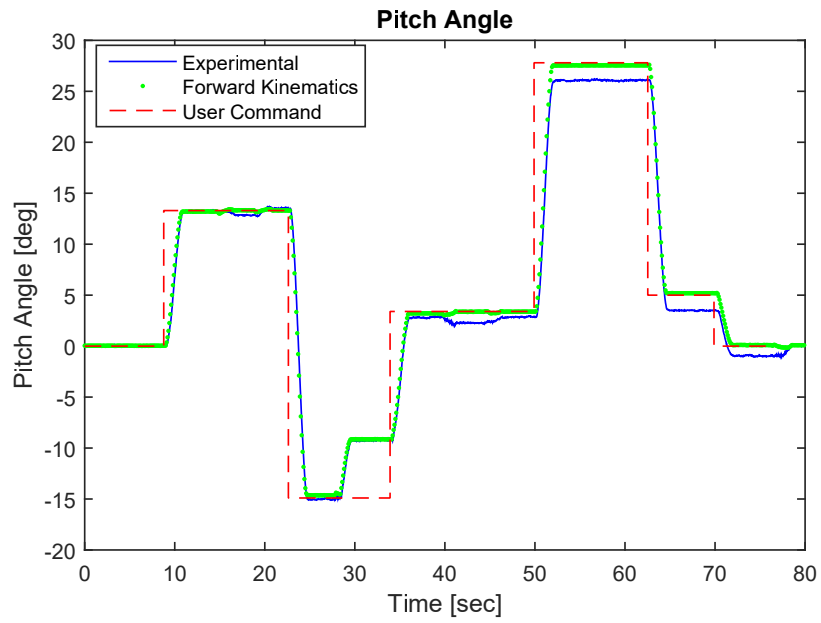


Figure 2.15 : Angular positions of the output shaft in pitch and roll axes.

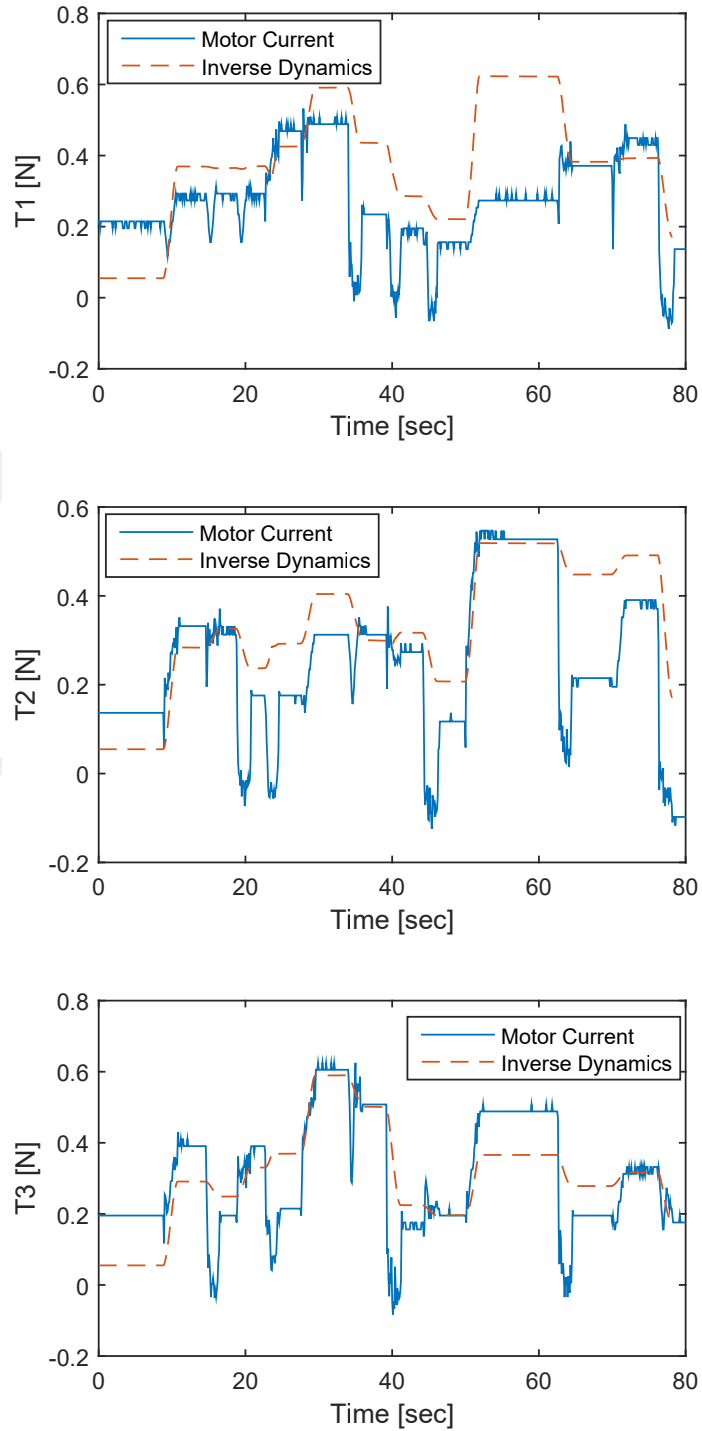


Figure 2.16 : Cable tension estimations from inverse dynamics and motor currents.

kinematic models, the dynamics are examined in three separate main steps: i) dimension reduction without information loss, ii) the helical spring analysis and iii) derivation of the complete dynamic model. In dimension reduction step, the pitch and roll motions are dealt with by combining the two motions in their effect, which is bending. The helical spring analysis takes the bending and the compression as input parameters and calculates the reaction moment and force where the relation is named as stiffness matrix. The reaction force results are validated by comparing to FEA results. At the end of this step, the look-up table for the experimental setup is created for a specified range of inputs. By using the knowledge of kinematics and the spring reaction forces, the complete dynamics model is presented.

The neck mechanism is manufactured and assembled to validate the kinematic and dynamic models. The same experiment, which consists of random user orientation commands for 80 seconds, is used for two different perspectives. The orientation of the upper plate is measured by an IMU and is estimated through the forward kinematics model. The results are compared to validate the forward kinematic model. Additionally, the IMU data and the user commands are compared to evaluate the inverse kinematic model and the controller performance. In addition to successful trajectory tracking, the forward kinematic model can also estimate the orientation. The second perspective in the experiments is to confirm the inverse dynamics model. For this reason, the cable tensions are estimated by using this model. Furthermore, the same quantities are computed from the motor loads and two data are compared. The results show that inverse dynamic calculations are similar to motor current values.



3. ELBOW - KNEE JOINT (VRP-VSJ) DESIGN AND ANALYSIS

A cable-driven variable stiffness 2 DOF joint mechanism is presented in this chapter. The mechanism resembles human elbow and knee joints regarding its one DOF rotation capability which is considered as a revolute joint. The second freedom is the result of compliance. The elastic behavior of this mechanism is obtained by a structure that resembles human antagonistic muscle-tendon-bone system. The motor and capstan pair imitates the muscle as it behaves like the energy source of the mechanism. The muscles are connected to the skeletal system with the tendons, providing the energy storage and the elasticity, which is imitated by a mechanism called as variable radius pulley (VRP). Besides the structural and functional similarity concerning actuation, the external forces/torques are estimated through the deflection measurements from VRP likewise the spindle organ in human muscles. Beyond the structural and functional similarity with humans, VRP-VSJ mechanism reduces the complexity and the cost remarkably. A simple schematic view of the VRP-VSJ is illustrated in Figure 3.1.

The biological and original version of this type of joint has the ability to change their stiffness value thorough co-contraction of agonist and antagonist muscle pair. Researchers in [62], are inspired by this natural aspect and designed a VSA in a similar structure. Besides, it is shown that non-linear springs are required to obtain a variation in stiffness. The necessity of quadratic spring profiles to attain a linear stiffness relation, which is a property of human muscles, is also shown in the same study. Additionally, stiffness variation of a robot joint is not limited to linear relations; a custom designed force-deflection function can be desired. The same study also states that despite the great effort on the design of non-linear spring mechanisms in the literature, they are mostly inaccurate without feedback and not easy to calculate. However, the researchers suggest a cam mechanism featuring quadratic spring behavior and the design is somewhat simpler than previous examples. Also, they included an antagonistic VSA experiment set-up with the help of proposed cam

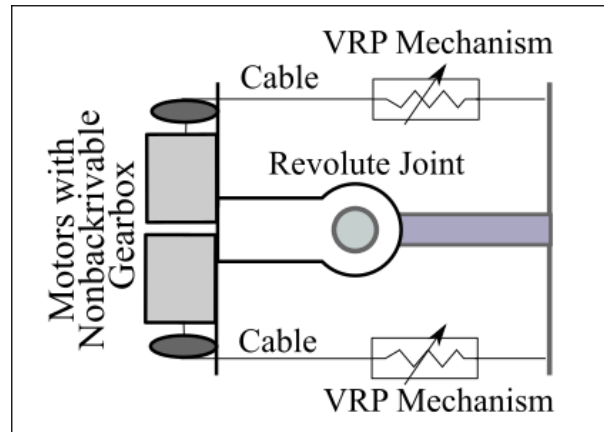


Figure 3.1 : Schematic representation of the mechanism and components.

mechanism yielding a linear stiffness profile. Beyond this, the cam mechanism offers a possibility of obtaining any desired force-deflection profile theoretically. Nevertheless, the mechanism covers a large area and is not suitable for an anthropomorphic arm design. The contact between the cam and the follower generate an excessive amount of friction. Besides, backlash and difficult implementation are the other issues to be tackled by designers. Alternatively, the use of variable radius pulleys (or non-circular pulleys) is a promising way to obtain a nonlinear spring. This idea is applied both in translational [100, 101] and rotational [102, 103] spring mechanism designs. The superiority of this approach is simplicity in its design which has less moving parts and can be fit into smaller spaces. The simplicity is not the only advantage of this design, but also cable-pulley mechanisms are subjected to friction far less than cam mechanisms are.

The name of VRP mechanism, which can be seen schematically in Figure 4.2, can vary such from wrapping cam mechanism to variable radius drums and non-circular spools. Similar to variation in names, the VRPs are used to fulfill many different purposes in various system designs. For instance, it is utilized in gravity compensation [104–106], VSA [107, 108] and specific motion profile generation [109] studies. The main focus of these studies is generating a custom non-linear force/torque-deflection relation by the synthesis of pulley profile. The pulley profile synthesis problem is tackled in an analytical manner in [100, 106, 110], whereas in [104] a numerical approach is taken. If we compare all these studies, in contrast to complicated calculations in the analytical method, a simple and efficient numerical solution technique is proposed in [104]. Another possible approach to the synthesis problem is considering it as an optimization

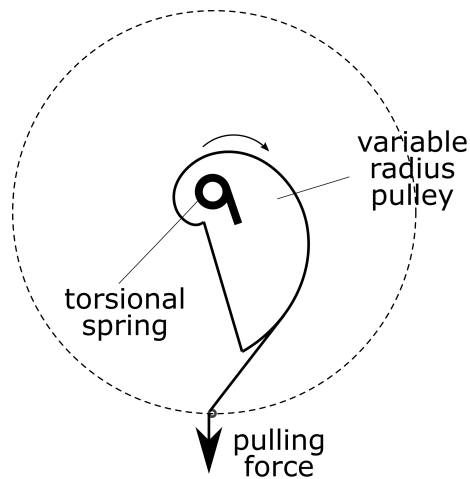


Figure 3.2 : Simplified view of VRP mechanism.

problem which attempts to minimize the desired and the generated torque in [107]. In a broader context, this technique can be widened to include whole series elastic actuator (SEA) design and tries to minimize the energy consumed by the motors. A more detailed analysis can be performed in [109] in which the idler pulley and the cable thickness effects are considered. Even though there are detailed studies on synthesis of VRPs, all the given methods are implemented to obtain a rotational non-linear spring by using a helical spring; however, in this thesis, a translational spring is generated by the VRP. Only limited number of studies are interested in this type of VPRs, and the synthesis methods are absent. For example, the study in [102] focuses on passive noise reduction and passes VRP synthesis without analysis. Another example is given in [103]; a synthesis method is presented which permits only the use of some non-linear functions.

The major contribution of this chapter is to propose a methodology for the synthesis of small size translational VRP mechanisms. Three methods are presented to synthesize VRPs to attempt to extend the current literature. Also, a low-cost, easily customizable, energy-efficient and safe VSJ that is based on translational VRP mechanisms are presented herein. In addition to synthesis and detailed VSJ design, three external force/torque (F/T) estimation technique are applied to the mechanism.

Since the VRP has a great influence on the proposed mechanism design, this chapter first describes VRP mechanism and presents three synthesis methods, after giving the current state-of-the-art studies. Following the experimental verification of these methods, the proposed VSJ is introduced with kinematic and dynamic models. Next,

the control method and the experimental setup is explained with the conducted position /stiffness control experiments. Then the external F/T is estimated via three methods, and the experimental results of these algorithms are given. Finally, the conclusions are drawn, and the future directions are presented.

3.1 VRP Mechanism Description and Synthesis Methods

The VRP mechanism offers a great range of applications regarding its simplicity. The VRP mechanisms can be implemented to generate a spring behavior in two contrary ways: translational or rotational. In order to obtain a translational spring (see in Figure 3.3.a), it includes a linear torsional spring connected to the pulley. When the cable which is wrapped around the pulley is stretched, the torsional spring is twisted. The torque generated by linear torsional spring is balanced with the product of pulling force on the other end of the cable and the radius where the cable leaves the pulley. Varying radius values creates a possibility of generating custom pulling force- cable elongation relationship/ mapping. In contrast, the same pulley-cable pair can be used as a custom non-linear rotation spring mechanism. In order to achieve the rotational spring features, a helical spring is connected to the end of the cable. Thus, the external torque exerted on the pulley is balanced with the linear helical spring elongation. Although both mechanisms are similar, the synthesis of the pulley profile differs in one design from the other. Despite of the various methods in the literature in terms of synthesizing pulley profiles for the rotational VRPs, however far too little attention has been paid to the synthesis of translational VRPs. Knowing the pulley profile alongside with the rotation angle, computation of the deflection of the helical spring and generated torque is straightforward for rotational VRP. On the other hand, the pulley profile and the cable elongation data is not enough to fully define the configuration, and further operations are needed to calculate the tensile force and the pulley rotation. In this section, an analytical method, originally developed for rotational VRP [110], is presented with its implementation to translational VRPs and a feasibility condition is defined to draw the boundaries of designs which are suitable for implementation. Following this method, two new numerical methods are proposed for same synthesis purpose.

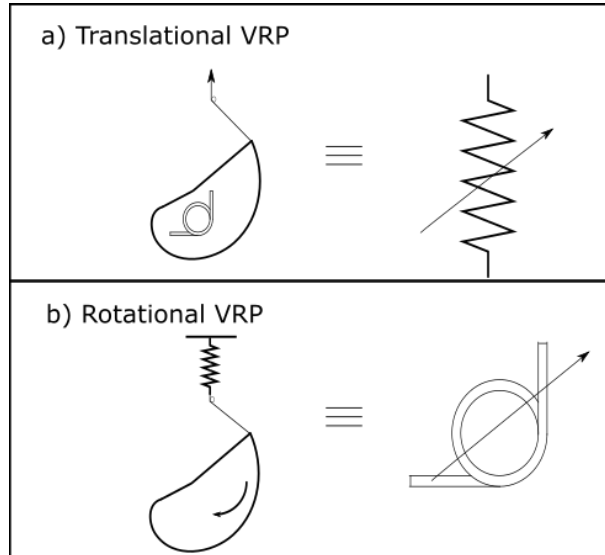


Figure 3.3 : Two possible use of variable radius pulleys to obtain a desired nonlinear spring: a) translational, b) rotational.

3.1.1 Analytic solution and feasibility condition

Even if the analytical solution of the pulley synthesis problem makes use of force and geometric quantities symbolically, resulting in a pulley profile as a function is presented in the literature, all of them are applied to rotational VRPs. Nonetheless, the contrast between two mechanisms has arisen not from the pulley but from the spring types. The translational mechanism utilizes a torsional spring which generates the reaction torque against the pulling force input, whereas the rotational mechanism makes use of translational spring to generate balancing force opposing to the torque input on the pulley. Therefore, analytical relations remain same, the perspective of the problem differs, the input is not torque on the pulley but is the pulling force on the cable. So a simplified version of the solution given in [110] is used to synthesize the pulley profile in this thesis. Also, the convergence of the solution is guaranteed due to given feasibility condition at the end. The geometric representation of the variables used in the analytical method is shown in Figure 3.4.

The relation between the pulling force ($F(u)$), the elongation of the cable (u), torque generated by the linear torsional spring ($M(\alpha)$) and the pulley rotation (α) can be given in equation (3.1) as a result of the principle of virtual work [146].

$$F(u)du = M(\alpha)d\alpha \quad (3.1)$$

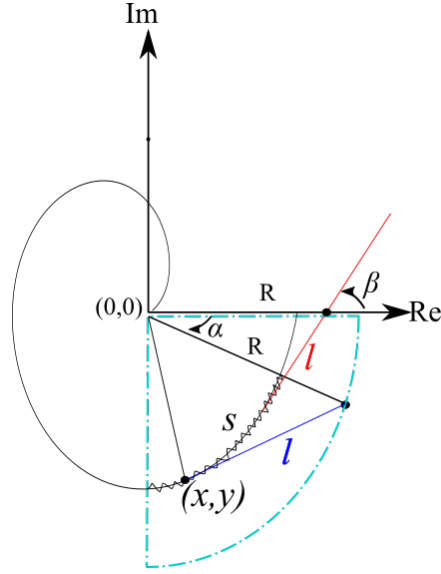


Figure 3.4 : Variables used in the analytical solution.

Re-organizing the equation (3.1) gives the derivative of the cable elongation with respect to the pulley rotation as in the equation (3.2).

$$\frac{du}{d\alpha} = \frac{M(\alpha)}{F(u)}. \quad (3.2)$$

If both sides of the equation (3.2) are integrated, the cable elongation can be expressed as a function of pulley rotation ($u(\alpha)$). It is worth noting that unlike the original method, torsion is generated by a linear source: the constant coefficient of the linear torsional spring is k_{spring} .

$$\int_0^u F(u)du = \int_0^\alpha M(\alpha)d\alpha = k_{spring} \frac{\alpha^2}{2}. \quad (3.3)$$

The elongation can be defined by using other geometric quantities as given in equation (3.4):

$$u = s + l - s_0 - l_0. \quad (3.4)$$

where wrapped cable length is denoted with s . The symbol l represents the free cable length. Departure angle β defines the derivative of departure point (x,y) with respect to wrapped cable length:

$$dx = ds \cos(\beta), \quad (3.5)$$

$$dy = ds \sin(\beta). \quad (3.6)$$

Loop closure method is used to define the equation between geometric quantities as in equation (3.7).

$$x + iy + le^{i\beta} = Re^{i\alpha}, \quad (3.7)$$

where R is the distance between the center of rotation and outlet point. Using necessary operations from Eqs. (3.4) and (3.7), the derivative of u w.r.t. α is calculated as in equation (3.8):

$$\frac{du}{d\alpha} = R\sin(\beta - \alpha). \quad (3.8)$$

By using the equations (3.3) and (3.8), β can be calculated as follows:

$$\beta = \sin^{-1}\left(\frac{1}{R}\frac{du}{d\alpha}\right) + \alpha. \quad (3.9)$$

The free cable length l can be obtained as given in equation 3.10.

$$l = \frac{R\cos(\beta - \alpha)}{\frac{d^2u}{d\alpha^2} \frac{1}{R\cos(\beta - \alpha)} + 1} \quad (3.10)$$

Finally, the pulley profile is obtained as given in the following equations.

$$x = R\sin(\alpha) - l\cos(\beta), \quad (3.11)$$

$$y = R\sin(\alpha) - l\sin(\beta). \quad (3.12)$$

As it can be seen from the equation (3.9) β is constrained between -1 and 1 in the light of the limits of the sine function. In other words, the convergence/divergence angle of the pulley cannot be less/more than $-90^\circ / +90^\circ$. Therefore, all arbitrary $F(u)$ functions cannot be obtained for any given k_{spring} values, physically. Hence, the choice of correct R and k_{spring} values is the key point in the synthesis problem. In order to select proper spring constant, the feasibility condition is defined as given in equation 3.13, describing the relation between the spring constant, desired pulling force and the outer radius of the mechanism.

$$k_{spring} < \frac{F(u)R}{\alpha}. \quad (3.13)$$

Because only positive values are implementable, the positive side of the equation is considered.

3.1.2 Numerical methods

Even though the analytical result is the preferable solution due to its precision, the convergence of it is not guaranteed, or the desired function cannot be expressed by an explicit function. Hence, defining the pulley profile and the force-elongation curve as discrete points, two iterative numerical algorithms are presented to overcome these

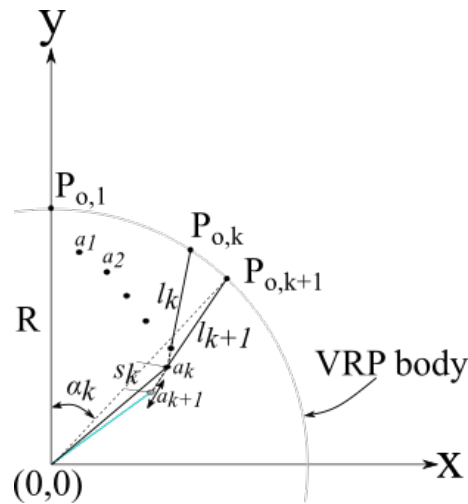


Figure 3.5 : Variables used in simple iterative method.

problems. The first method presents a solution which considers the tangency condition and calculates the pulley profile point-by-point iteratively. On the other hand, the second algorithm attempts to minimize the error between the desired and the simulated force-elongation curves by changing the positions of the points which constitute the pulley profile. For this reason, a simulation algorithm is necessary to analyze the given pulley profile. Albeit the analytical method approaches problem likewise in the rotation spring, the examination of the translational spring mechanism is not as simple as the rotational version. The principal difference between them is the determination of the cable departure point position. When the rotation angle of the pulley is known, which is the scenario in rotation spring mechanism, it is straightforward to calculate departure point position. In contrast, further calculations are needed to find the position when the amount of the cable pulled is known in lieu of pulley rotation.

3.1.2.1 Simple iterative method

Using the tangency property, which means the cable always leave the pulley with the tangent angle at the departure point, the pulley profile is synthesized for a given initial point and torsional spring coefficient. Unless the convergence is achieved, then the initial point-spring coefficient pair is changed to attempt solution again. The variables used in the method are given in Figure 3.5.

The algorithm starts with the specified initial point to be assumed as the first departure point (a_k). The index k denotes the iteration step and corresponds to discrete points on the pulley profile. Consequently, the force-elongation curve (F_{des}, u_{des}) is defined in a

discrete way and decides the number of points on the pulley profile. So, if a precise definition of the profile is required, then the force-elongation curve should incorporate as many points as possible. Supposing the first elongation amount is equal to the first distance (l_k) between the outlet point ($P_{o,k}$) and the departure point (a_k), the next departure points are calculated as given in equation (3.14).

$$a_{k+1} = a_k + \frac{a_k - P_{o,k}}{|a_k - P_{o,k}|} (s_k). \quad (3.14)$$

It should be noted that s_k is the wrapped cable length between two consecutive departure points. It should be remembered that the points are connected with lines, not splines. Thus, s_k is simply calculated by taking the distance between consecutive points. Because it is unknown in a calculation step initially, it is assumed to be equal to Δu_{des} . As a result, the value of l_{k+1} can be calculated as follows:

$$l_{k+1} = l_k + \Delta u_{des} - s_k. \quad (3.15)$$

To calculate the pulley rotation between successive desired elongation points, first, a circle is drawn around a_{k+1} with a radius of l_{k+1} . The intersection between this circle and the virtual circle around the center point with a radius of R representing the VRP body defines the next outlet point ($P_{o,k+1}$). The rotation angle is calculated as in the following equation.

$$\alpha_k = \tan^{-1} \left(\frac{P_{o,k+1,x}}{P_{o,k+1,y}} \right). \quad (3.16)$$

The force equivalence can now be calculated by the help of the geometric definitions. Expressing the unit vector between $P_{o,k+1}$ and a_{k+1} as $\mathbf{l}_{k+1,u}$, the tensile force can be calculated with regard to $\mathbf{l}_{k+1,u}$ and α_k as follows:

$$F_{vrp,k} = \frac{k_{spring} \alpha_k}{\alpha_{k+1,x} \mathbf{l}_{k+1,u,y} - \alpha_{k+1,y} \mathbf{l}_{k+1,u,x}}. \quad (3.17)$$

If the error between $F_{vrp,k}$ and $F_{des,k}$ is smaller than a threshold, k is increased by one. Otherwise it determines the next s_k and iteration returns to the equation (3.13) and repeats all the steps with a new s_k . The next s_k is calculated with a step size h factor as follows:

$$s_k = s_k - h(F_{des,k} - F_{vrp,k}). \quad (3.18)$$

The iteration stops when all the desired force-elongation points are paired with departure points on the pulley surface. Depending on the initial point selection and

the feasibility condition, the solution may not converge. However, the algorithm runs very fast which allows numerous attempts.

3.1.2.2 Optimization method

This method treats the synthesis task as a nonlinear constrained optimization problem which is defined as in the equation (3.19).

$$\begin{aligned}
& \underset{k_{spring}, r}{\text{minimize}} && \sum_{k=1}^{n_f} [f_{des,k} - f_{vrp,k}]^2 \\
& \text{subject to} && r_{i+1} - r_i \geq 0, \quad i = 1, \dots, m-1, \\
& && 0 < r_i < R.
\end{aligned} \tag{3.19}$$

At the beginning of the algorithm, an arbitrary pulley profile is specified, such as a circle. For the sake of simplicity, m points are placed around the center of rotation evenly spaced in polar coordinates. The desired force-elongation curve is defined as vectors having the same length in F_{des} and u_{des} . Unlike the previous methods, the torsional spring coefficient is not specified by the designer, and it is calculated in the algorithm alongside with the pulley profile. As expected, it can be excluded from the algorithm, if the coefficient is known. After simulating the completely-defined VRP, the force-elongation curve is generated. The resulting curve is compared with the demanded curve, and optimization algorithms decide, how to slide the positions of r_i on the lines drawn out from the center of rotation and change the spring coefficient, to minimize the difference between the curves. The iterative cycle of analysis and changing the features in turn continues until a local minimum is reached. The variables and the geometric representation can be seen in Figure 3.6.

After the initial definitions, the algorithm calculates the departure point (p_n) and the wrapped cable length (s). In addition to this, the distance (l_k) between the outlet point (P_o) and the departure point (p_n) is computed initially. Since a stretched cable can exclusively wrap around a convex geometry, only the points on the convex hull influence the calculations. The center of rotation (0,0) is also included within the convex hull. Denoting by P_i , the points included by the convex hull are sorted by their angles in increasing order. Straight lines are drawn between P_o and p_i and the number of intersection with the convex hull is found, repeating for every interior points of the convex hull. The departure points for the current configuration are identified when the intersection number stays as one, and they are shown by p_n . Besides, wrapped cable

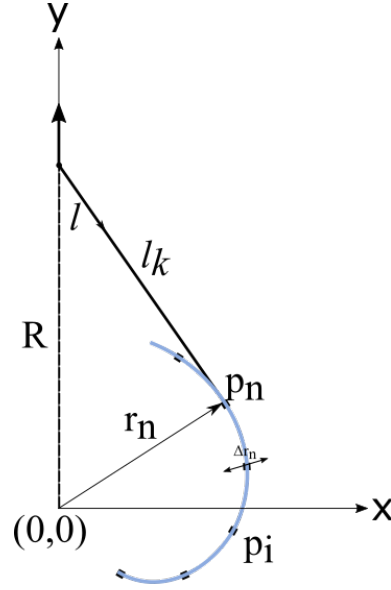


Figure 3.6 : Variables used in optimization based method.

length (s) can be calculated initially as follows:

$$s_0 = \sum_{i=1}^n ||P_{n,i+1} - P_{n,i}||. \quad (3.20)$$

Determination of the initial location is followed by an analysis for each $u_{des,k}$, so that $F_{vrp,k}$ is obtained. Similar to previous method $(.)_k$ stands for the index of force-elongation curve elements. The analysis requires the correct determination of rotation of the pulley α_k for a given cable elongation $u_{des,k}$. In the initial stage of the algorithm, departure point index (n) is assumed to be 1, considering the farthest point to the outlet point. In k^{th} step, the idle cable length inside the mechanism is computed as in the equation (3.21).

$$l_k = l_0 + s_0 - u_{des,k} - s_k. \quad (3.21)$$

The cable length wrapped around the pulley, s_k , can be calculated similarly to the s_0 , at its initial pose. Great care must be taken at this point of the algorithm to calculate the rotation α_k when the l_k is known. A circle with a radius of l_k is drawn around the P_o , and a circle with radius r_n is drawn around $(0,0)$. In case of correct dimensions, these circles intersect at two points. Since the operation is performed in the first quadrant, positive coordinate values both in x-axis and y-axis are taken into account from these points. All points in the convex hull which represents the pulley profile are rotated by an angle that is calculated as the angular difference between p_n and the selected intersection point. Like in the initial setup, a straight line is drawn between P_o and p_n , and the intersection between the convex hull is counted. If the intersection is equal to

1, then the rotation angle and departure index are determined as α_k and 1 respectively. Otherwise, the assumption for n is increased to 2 and the calculations are repeated until the number of intersection equals to 1.

After completing the geometric calculations, one can now calculate the force value according to the elongation. The position vector \mathbf{r}_n and the unit vector in cable direction \mathbf{l} are necessary to be calculated to determine the force value.

$$\mathbf{r}_n = \begin{bmatrix} p_{n,x} \\ p_{n,y} \end{bmatrix} \quad (3.22)$$

The direction of the tensile force is indicated by the unit vector \mathbf{l} and it is calculated as in the equation (3.23).

$$\mathbf{l} = \frac{\mathbf{p}_0 - \mathbf{r}_n}{\|\mathbf{p}_0 - \mathbf{r}_n\|}. \quad (3.23)$$

Considering the static equilibrium, the moment generated by the torsional spring equals with the moment exerted due to the tensile force $F_{vrp,k}$, as given in equation 3.24.

$$\mathbf{M} = \mathbf{r}_n \times F_{vrp,k} \mathbf{l}. \quad (3.24)$$

The assumption of linear torsional spring, the equation can be modified as given in the equation 3.25, noting that the rotation is defined around the z-axis.

$$M_z = K \alpha \quad (3.25)$$

In this case, the tensile force is obtained as follows:

$$F_{vrp,k} = \frac{M}{r_{n,x}l_y - r_{n,y}l_x}. \quad (3.26)$$

Since the non-convex points are dysfunctional in the pulley profile, non-strictly increasing or decreasing function is admissible for the force-elongation curve. Thus, the restriction is reflected as a constraint to optimization method according to the characteristics of F_{des} . Even though the computational cost of the proposed method is higher than the previous approaches, it is possible to widen its scope by incorporating with the specific working constraints of the VRP-VSJ mechanism in the future studies. For instance, the energy consumption of VRP-VSJ can be used to define the cost function in the optimization method/algorithm and the pulley profile can be calculated to reduce this value most.

3.1.3 Implementation of VRP

In this section, the presented algorithms are compared when the quadratic force-elongation curve is treated as a benchmarking problem as given in equation (3.27).

$$F_{des} = 0.003u_{des}^2 + 0.2u_{des}. \quad (3.27)$$

It should be noted that units of F_{des} and u_{des} are defined as N and mm respectively. Experimental quantities are used in this comparison. The radius of the VRP main body is $17.5mm$ defining the maximum radius of the pulley. On the other hand, bearing radius determines the minimum radius of $8mm$. The stiffness of the torsional spring is calculated as $0.96Nmm/rad$ by using the procedure detailed in the experimental setup.

The commercially available software Matlab symbolic toolbox is utilized to calculate the analytical solution. Since the function $u(\alpha)$ is highly nonlinear, it is not easy to obtain $\alpha(u)$ function as a closed mathematical representation. Henceforth, the numerical values are substituted with the symbolic ones. The feasibility check determines the range of allowable α whereas the final values are established by trial and error. The implementation is given in Algorithm 1.

Algorithm 1 Analytical Method

- 1: Calculate symbolic $u(\alpha)$ by using equation (3.3)
 - 2: Derive $u(\alpha)$ to find $\frac{du(\alpha)}{d(\alpha)}$ and $\frac{d^2u(\alpha)}{d(\alpha)^2}$
 - 3: Compute β and l via equations (3.9) and (3.10)
 - 4: Pick a range for α and form a vector
 - 5: Determine range of u , if it is not achieved change the range
 - 6: Check feasibility condition, if it is not satisfied change α range
 - 7: **for** each α_j in α **do**
 - 8: Evaluate equations (3.12) and (3.13)
 - 9: **end for**
 - 10: Return the pulley profile (x,y)
-

The simple iterative method, for which the complete procedure is shown in Algorithm 2, is run in Matlab Environment. The choice of the initial departure point affects the convergence of the solution; therefore, several attempts are required most of the time in order to get a convergent solution. The technique results solely for feasible points as in analytical method; otherwise, the points on the pulley profile get extreme values, constituting the extremity of the algorithm for any given force-elongation curve.

Algorithm 2 Simple Iterative Method

```
1: Set a random  $a_1$  on the first quadrant
2: for each  $F_{des,k}$  in  $F_{des}$  do
3:   Define  $s_k$  as  $\Delta u_{des}$ 
4:   while Absolute value of  $F_{des} - F_{vvp} < \text{threshold}$  do
5:     Determine  $a_{k+1}$  via equation (3.14)
6:     Calculate  $l_{k+1}$  by using equation (3.15)
7:     Draw two circles: 1) Center:  $P_{o,k+1}$ , Radius:  $l_{k+1}$  2) Center:  $(0,0)$ , Radius:  $R$ 
8:     Use intersection of two circles to find  $\alpha_k$ 
9:      $F_{vvp,k}$  is calculated as given in equation (3.17)
10:    Set new  $s_k$  according to the error
11:   end while
12: end for
13: Return the pulley profile  $a$  points
```

The nonlinear optimization based method is implemented using Matlab '*fmincon*' function as given in Algorithm 3. the selection of the initial points have less influence on the solution convergence; therefore they are merely placed on a half circle incorporating 0.1radian increment. The algorithm simulates the behavior of the mechanism for every different pulley profile try and reduces the error. Unlike the other methods, regardless of whether it is feasible or not, this algorithm attempts to calculate pulley profile in the best available manner.

The same computer, which has Intel i7-6500U CPU and 8GB RAM, executed the algorithms that yielding discrete points representing the pulley profile. Increasing the number of discrete points did not affect the computation time since the profile is analytically known, the analytical method completed the calculation in 5.76 seconds. On the other hand, the simple iterative method is the best in computation time-cost with 0.016 seconds, because only numerical function evaluations are included within the algorithm which leads faster operation compared to symbolic calculations. The nonlinear optimization method is far slower than the other two methods with a duration of 202.6 seconds. The computation time exponentially grows with the increasing number of discrete points in this method, whereas it is proportional to the simple iterative method. The resulting pulley profiles vary depending on the algorithm which is demonstrated in Figure 3.7. To emphasize how the profiles play a role in implementation, the 3D printed pulley, which is obtained from optimization method, is placed to the VRP body center in Figure 3.7.

Algorithm 3 Optimization Method

```
1: procedure ANALYZE( $p$ )
2:   Set error = 0
3:   Determine convex hull of  $p$ 
4:   for each  $p_i$  in  $p$  do
5:     Draw line between  $p_i$  and  $P_o$ 
6:     if (Number of line intersection with convex hull = 1)
7:        $n=i$ 
8:       break
9:     end if
10:  end for
11:  Calculate  $s_0$  and as shown in equation (3.20)
12:  for each  $F_{des,k}$  in  $F_{des}$  do
13:    for each  $p_i$  in  $p$  do
14:      Compute  $l_k$  and  $s_k$ 
15:      Draw two circles: 1) Center:  $p_n$ , Radius:  $l_k$  2) Center: (0,0), Radius:
16:       $R$ 
17:      Determine  $\alpha_k$  from circle intersection
18:      Rotate  $p$  by  $\alpha_k$ 
19:      Draw line between  $p_n$  and  $P_o$ 
20:      if (Number of line intersection with Convex Hull != 1)
21:         $n=n+1$ 
22:        break
23:      end if
24:    end for
25:    Calculate  $r_n$ ,  $\mathbf{l}$  and  $F_{vrp,k}$ 
26:     $error = (F_{des,k} - F_{vrp,k})^2 + error$ 
27:  end for
28:  Return error
29: end procedure
30: Set initial  $p$  vector
31: while Optimization criteria are not satisfied do
32:   ANALYZE( $p$ )
33:   Determine new  $p$  via optimization method
34: end while
35: Return convex hull of  $p$ 
```

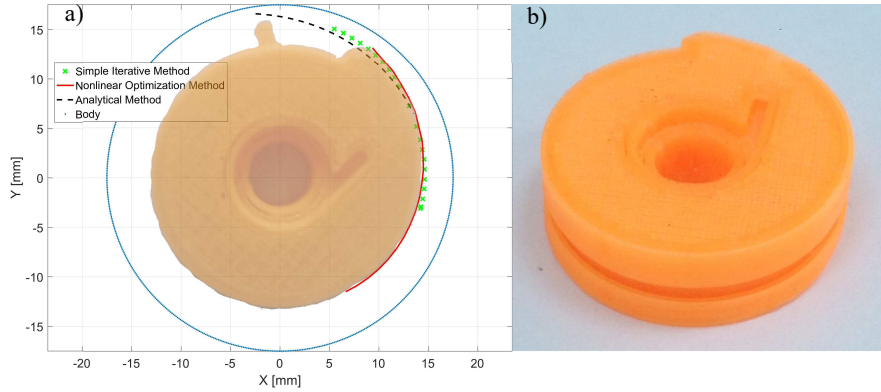


Figure 3.7 : Synthesized pulley profiles: a) from three methods and b) 3D printed pulley image for optimization method.

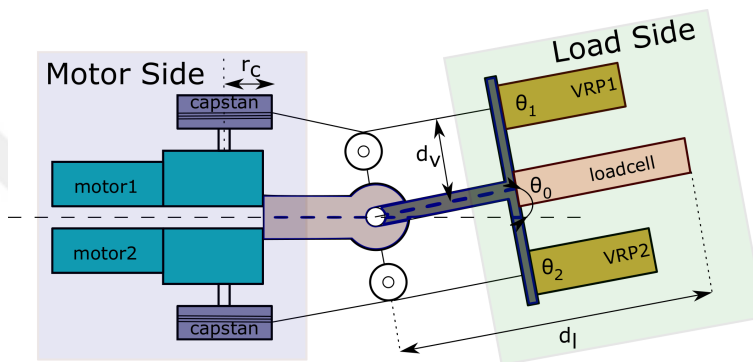


Figure 3.8 : Schematic view of VRP mechanism.

3.2 VRP-VSJ Mechanism

A cable-driven 2 DOF variable stiffness joint mechanism VRP-VSJ is explained in this section. At least two parameters, which are namely the position and stiffness, are needed to describe the configuration of the mechanism. Because it is driven by two motors, VRP-VSJ is a fully-actuated mechanism. A simple drawing of the mechanism with the variables used in the analysis is illustrated in Figure 3.8. As it can be seen from the figure, a revolute joint restricts the motion as a rotation whereas 2 DC motors, by pulling the cables via the capstans fixed to each motor shaft, actuates the mechanism. The remaining ends of the cables are wrapped around the pulleys in VRPs. When the motors move in opposite directions, the position of the mechanism changes. On the contrary, to adjust the stiffness value, both motors rotate in the same direction, i.e., pull or release the cables at the same time. The stiffness variation arises from the nonlinear spring mechanisms (VRP) that are detailed in the previous section. The position and stiffness of the mechanism are measured by the encoders coupled with the revolute joint and VRPs respectively.

Substantially, the VRP-VSJ mechanism is designed to be utilized as elbow or knee joint in humanoid robots, which are able to work in environments where unfavorable working conditions for people can exist. As a natural result of the inclusion of passive compliance by the mechanism, it contributes significantly towards human-robot interaction safety. Thanks to the ability of variable stiffness, the mechanism can work in the necessary configurations for different types of daily tasks or different situations (acceleration, stop, etc.) in the same task.

Despite the fact that the significant VSJ/VSA designs have been presented in recent years, they are complicated, heavyweight, expensive and hard-to-produce. The proposed mechanism in this chapter, suggests a solution to these problems without losing essential features such as compliancy, variable stiffness, and controllability. The mechanism can be considered as a good combination of off-the-shelf products, and 3D printed part from low-cost FDM printers, alleviating the total cost that is given in Table (3.1).

A prominent asset of the system is its back-drivability while the actuation units are motors with non-backdrivable gearboxes, providing passive gravity compensation alongside with the compliance. This unique feature increases the energy-efficiency so that when the mechanism at rest, energy consumption decreases to zero, which is crucial for humanoid robots with energy supplies as batteries. It is known that presence of gearboxes in joint designs poses a problem due the backlash in the gearbox. This problem is defeated to a certain level as a result of the cable tension which tries to close the gap between adjacent teeth. The simple design helps the modeling and control, and pave the way for external F/T estimation which is examined at the end of this chapter. As a result of these benefits, it has a potential of usage in humanoid robots.

3.2.1 Dynamic model

Since it is fixed to prior links of the robot or a base, the motor side is assumed to be at rest and out of interest in the dynamic model. Since the DOF for motion is 1 for this system, a basic dynamic model is calculated. The forces and torques acting on the mechanism are illustrated in the free body of the mechanism, given in Figure 3.9. Since the rotation center of the load side is the center of the revolute joint, the equation

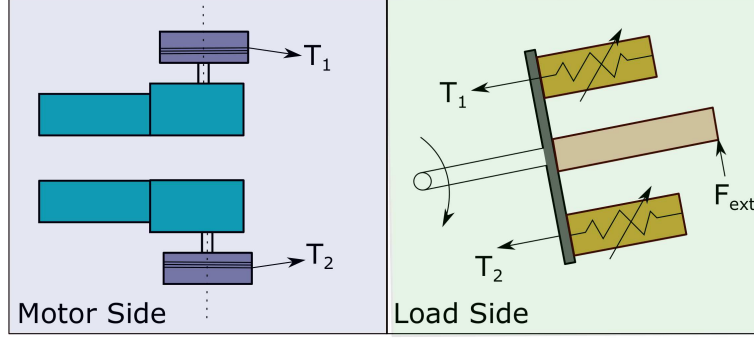


Figure 3.9 : Free body diagram of the mechanism.

of the motion is expressed by calculating moment equilibrium around this point as given in equation (3.31).

$$\bar{J}\ddot{\theta}_0 = T_1 d_v - T_2 d_v + \tau_{ext}. \quad (3.28)$$

The inertia of the load side is denoted by \bar{J} . The symbol θ_0 stands for the joint angle. The cable tension forces are described as T_1 for left and T_2 for right side. The idler pulleys connected to the revolute joint ensures that the cables are always retained parallel to each other, and the distance to the link is d_v for each one. The external effects are reduced to the generalized force definition and presented as torque which is denoted by τ_{ext} .

$$T_i = f_{vrp_i}(\theta_i) \quad i=1, 2. \quad (3.29)$$

The cables are directly connected to VRPs; thus the tension forces can be computed from the elastic properties of them. The rotation of pulleys θ_1 and θ_2 in VRP mechanism depends on the twist of the torsional springs. In the design stage of the VRP, the pulley geometry constitutes a non-linear relation between pulling force and the pulley rotation. Although it can be obtained from the aforementioned calculations explained in VRP design section, another way to obtain the same relation is to collect data from a tensile test with a physical setup. The relation is defined as a function f_{vrp} for both VRPs. It is worth noting that, two VRPs are designed symmetrically, however in practice, they are not completely same because of imperfect manufacturing and assembly. Consequently, they are treated as different functions to account small variations. Thus the motor side of the equation is calculated as follows:

$$\tau_{m_i} = f_{vrp_i}(\theta_i) r_p \quad i=1, 2, \quad (3.30)$$

where r_c is the radius of the motor pulley.

3.2.2 Stiffness adjustment ability

In order to define the stiffness of the mechanism, general definition of stiffness for one DOF system can be referred, which is known as the displacement according to applied force along the same DOF. The mathematical expression for this definition is the derivation of the force with respect to the displacement. In this way, the overall stiffness of the mechanism is described as the derivative of the reaction moment M_{spring} w.r.t. the revolute joint angle θ , reducing the VRP-VSJ mechanism to a torsional spring. As a consequence of unilateral tension forces on cables, one of the cables is active in the stiffness calculation according to the motion direction. Recapping the constant distance between the link and the cables d_v , the stiffness (K) is formulated as a function of active cable tension as given in equation (3.31).

$$K = \frac{dM}{d\theta} = \frac{dF}{d\theta} d_v \quad (3.31)$$

From a geometrical point of view, elongation of the cable u depends on θ and d_v with an infinitesimal displacement assumption shown in equation (3.32).

$$d_v d\theta = du \quad (3.32)$$

By applying chain rule and inserting equation (3.31) into equation (3.32) to obtain K value, stiffness formula becomes as it is seen in equation (3.33):

$$K = \frac{dF}{d\theta} d_v = \frac{dF}{du} \frac{du}{d\theta} d_v = \frac{dF}{du} d^2. \quad (3.33)$$

It can be inferred that VRP-VSJ mechanism stiffness is proportional to the derivative of VRP force-elongation curve. For example, if a quadratic curve is preferred, then the stiffness becomes linear, verifying the results given in [62].

3.2.3 Position and stiffness control

Considering the symmetrical structure and unidirectional force application capability of the cables, symmetrical two-part control is applied to the mechanism. In this control scheme, depending on the motion direction, each motor is assigned to control stiffness or position. In fact, if a position command tries to rotate the joint to left from its current position, left motor and right motor are assigned to position and stiffness control tasks,

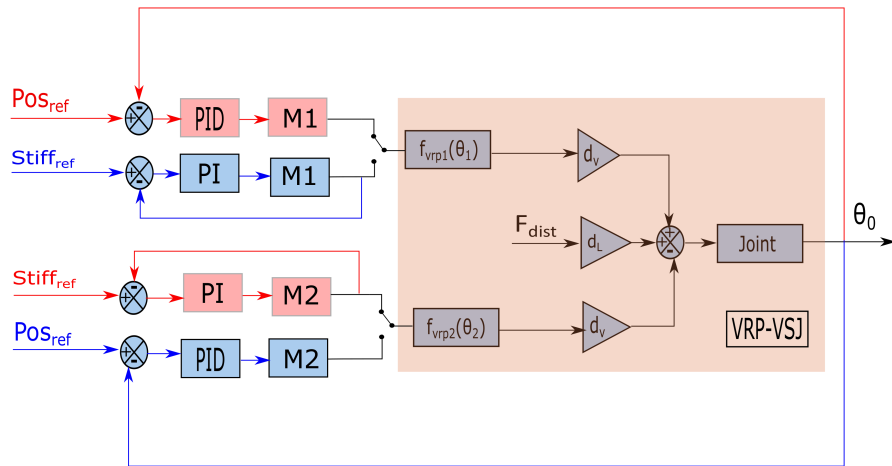


Figure 3.10 : Controller block diagram.

respectively. On the contrary, if a position command tries to rotate the joint to the right, left and right motors are assigned vice versa. Position and stiffness controls are maintained by using PID and PI controllers respectively. The block diagram of the control structure is illustrated in Figure 3.10. As can be seen from the figure, position and stiffness references follow either blue or red paths with regards to motion direction.

3.3 Experimental Setup and Results

In this section, two different experiments are conducted. The first experiment is to measure the performance of the synthesis algorithms, and the results are presented in terms of the tension on the cable, the pulley rotation and the elongation. On behalf of the experiment, a tensile test platform is manufactured which measures these three quantities at the same moment. The second experiment is performed to test the VRP-VSJ and the control algorithm performance.

3.3.1 Tensile test of VRP mechanism

A custom experiment equipment is built for tensile test in which the sample is subjected to a controlled pulling force to a certain level. This platform, which is made of PLA material and steel bars, is given with components in Figure 3.11. To complete the tensile test, firstly the VRP is fixed to the base. The remaining end of the cable belonging to VRP is knotted to the grip part which is connected to a load cell, measuring the pulling force. The moving part carrying the load cell is translated via leadscrew manually by the help of hand wheel in which a nut is fixed. Thus the rotation

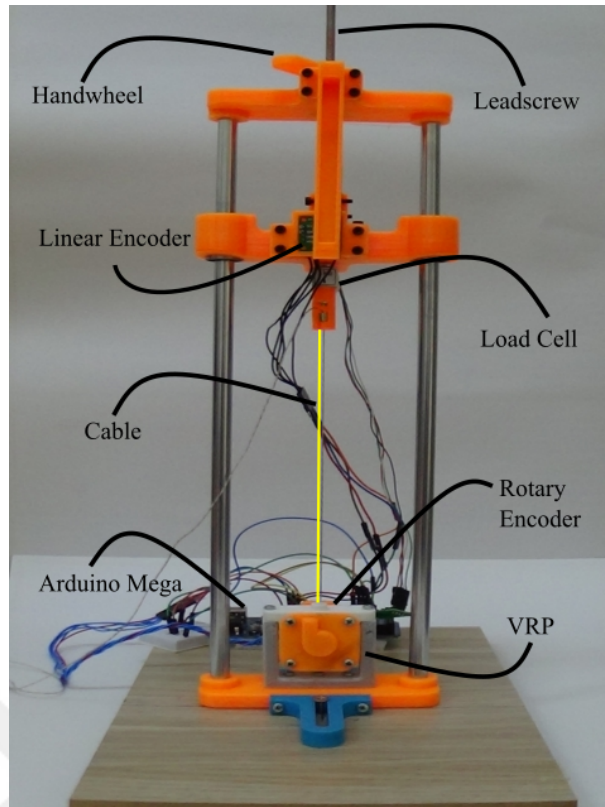


Figure 3.11 : The tensile test equipment.

of the hand wheel translates this part. A linear encoder (AMS AS5410) captures the translation of the moving part whereas rotary encoder (AMS AS5405) measures the rotation of the pulley. All data from three sensors are acquired by using an Arduino Mega2560 simultaneously.

VRP is manufactured and assembled to compare the accuracies of the proposed synthesis algorithms for a case study. Later the best algorithm is used to synthesize desired pulley profile, and it was utilized within the VRP-VSJ mechanism. The bounding box for the VRP design is assigned as $40 \times 40 \text{ mm}$. Exploded view of the complete assembly of the experimental setup can be seen in Figure 3.12. For examining the performances, the pulley profiles are taken from the outputs of the algorithms and manufactured using a 3D printer. The shaft is fixed to the pulley and connected to the VRP body with a rotational ball bearing to minimize the friction in between. On the other side of the shaft, a magnet is placed to the end on instead of the rotary encoder that measures the angle without touching the shaft. The torsional spring is connected between the pulley and the cover, and only rotational motions are allowed. The output hole is either covered with a Teflon tube or connected to an idler pulley, to reduce the friction between the body and the cable.

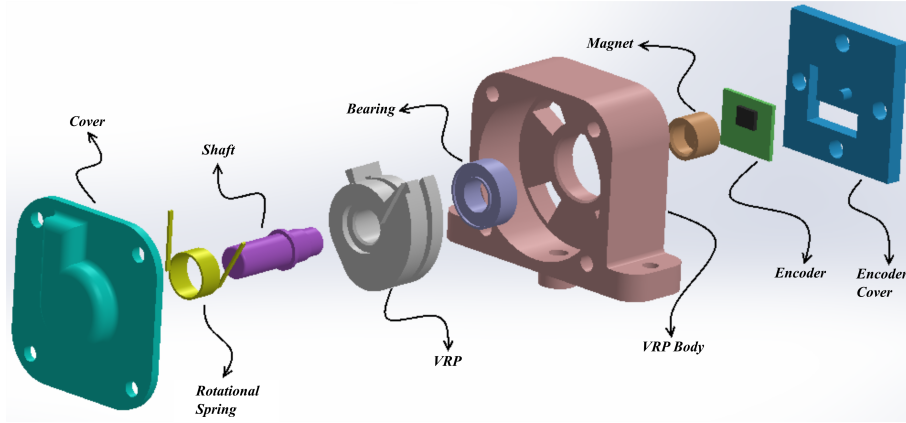


Figure 3.12 : Exploded view of VRP mechanism.

The torsional spring coefficient is determined via a fully-circular pulley within the test rig. The multiplication of the measured tensile-force with the constant pulley radius gives the moment generated by the spring. The value of the spring coefficient is also validated using spring formulas given in the textbooks according to its material and geometry.

After completing the tensile test for three synthesis methods, force-elongation curves for each algorithm is obtained which are given in Figure 3.13. In this figure; blue, green and red lines show experimental, desired and simulation results successively. As can be seen from the figure, the most accurate results are obtained by using the nonlinear optimization method with 13.3% RMS error. The errors for analytical and simple iterative methods are observed as 42.7% and 29.3%, respectively. As it is stated in previous part in this chapter, the analytical method and simple iterative method cannot give reliable results unless feasibility condition is satisfied, whereas, the optimization based method can always search for better profiles to minimize the error.

In order to emphasize the stiffness change, a new VRP design is synthesized accompanying increased value of the quadratic component of the case study force-elongation function. The new quadratic function is specified as given in equation (3.34).

$$F_{des} = 0.02u_{des}^2 + 0.1u_{des} \quad (3.34)$$

Force-elongation (a), force-rotation (b) and elongation-rotation (c) plots can be seen in Figure 3.14 for the final pulley design. The RMS error between the desired function and the experimental result is calculated as 0.3469N in view of the fact that uncertainty in torsional spring coefficient, lack of precision of FDM type 3D printer and the friction

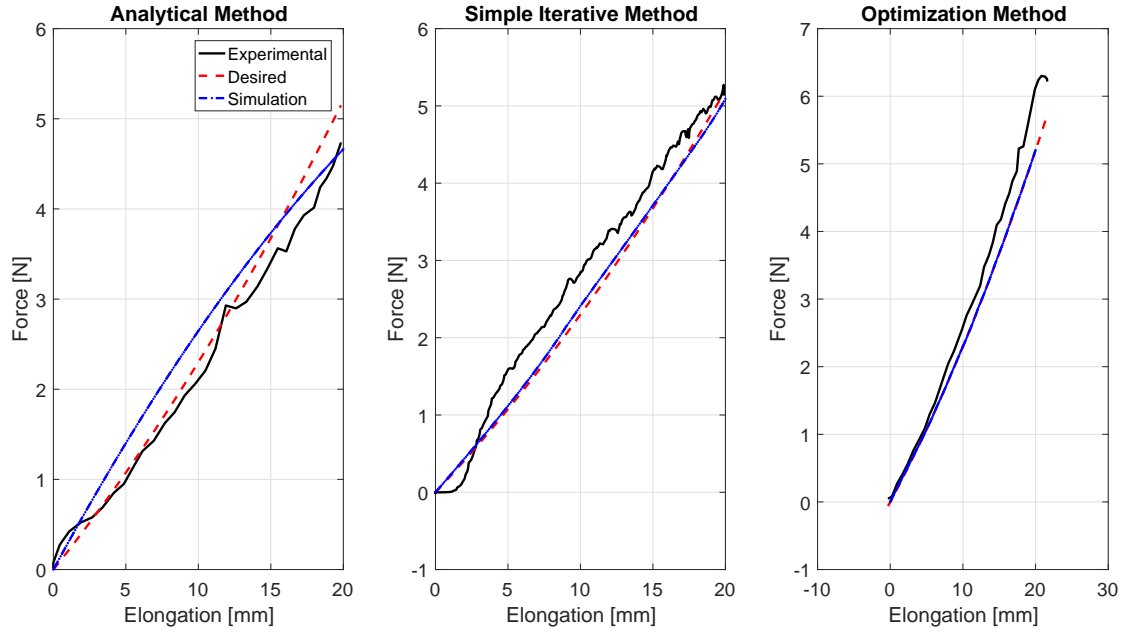


Figure 3.13 : Force-elongation curves for three proposed methods from left to right: analytical, simple iterative and nonlinear optimization.

forces are not included in the model. Furthermore, the noise in both the load cell and the encoder measurements can reflect as an error in the results. Force-rotation and elongation-rotation curves serve as relation maps since solely rotation can be measured in the VRP-VSJ mechanism.

Because the antagonistic setup is symmetrical, two identical VRP mechanisms are required to complete VPR-VSJ assembly. Although the same geometrical identities are used in manufacturing process, the force-elongation curves of two such mechanisms are not completely same, as observed in Figure 3.15. Unfortunately, hysteresis occurs due to friction between adjacent coils of the torsional spring according to these curves so the force values are different for pulling and releasing directions. As a result, further care should be taken to estimate the VRP-VSJ mechanism stiffness depending on the "pull" or "release" mode.

3.3.2 VRP-VSJ mechanism control test

An experimental setup for the VRP-VSJ mechanism is manufactured including final design and implementation of agonist-antagonist VPRs. In this setup, the actuation is provided by two low-cost DC motors with worm gear reducers. The angular position of the revolute joint is measured by the same encoders used in VRPs. All of the

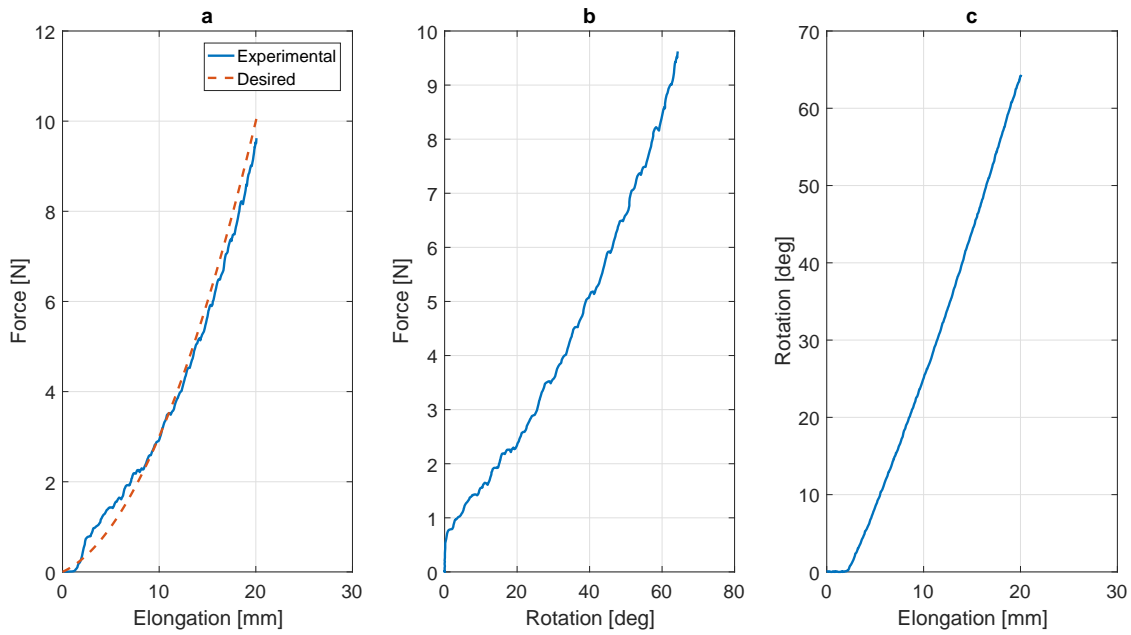


Figure 3.14 : Experimental results for the VRP mechanism synthesized to use in VRP-VSJ: a) force-elongation b) force-rotation c) rotation-elongation relations.

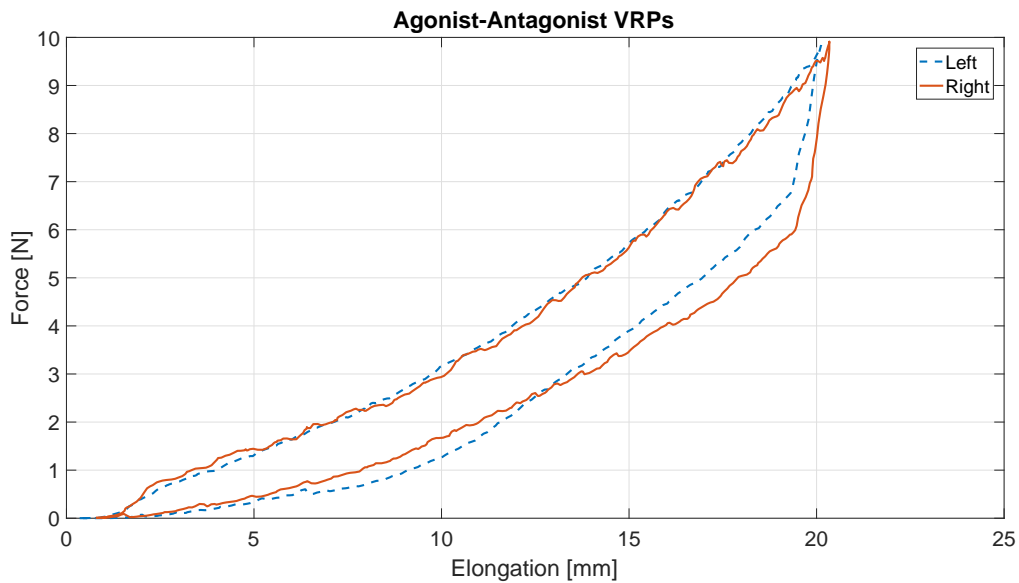


Figure 3.15 : Agonist-antagonist VRP pair force-elongation curves showing hysteresis.

Table 3.1 : Total cost of experimental setup for VRP-VSJ mechanism.

Component	Cost per item
DC motor	8.50 \$
Encoder	12.53 \$
Arduino Mega	7.35 \$
PLA	1.5 \$
Other mechanical	2 \$

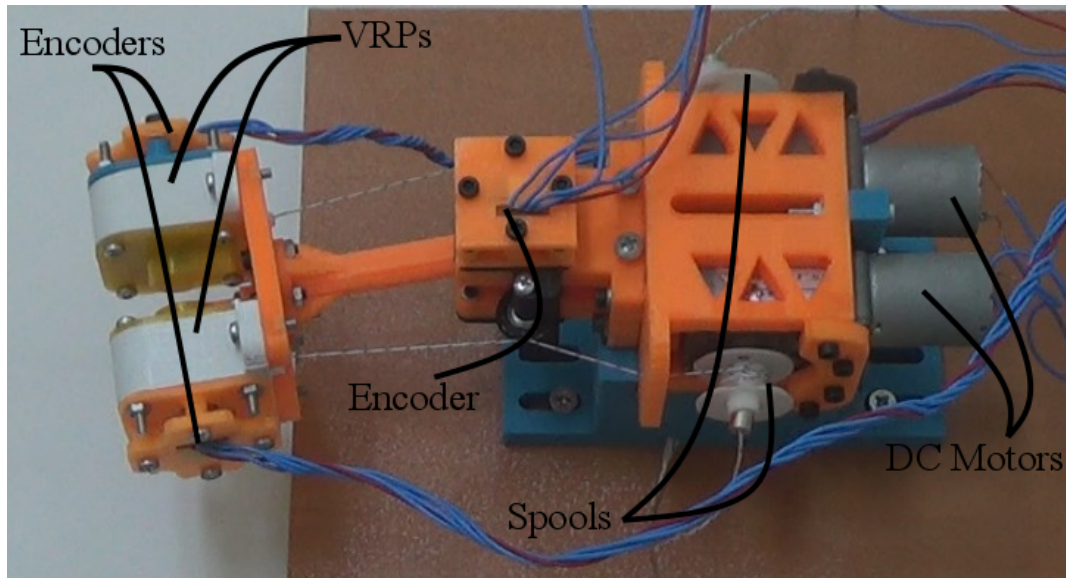


Figure 3.16 : Experimental setup for VRP-VSJ mechanism.

components are 3D printed from PLA material with the exception of bolts, nuts, bearings, encoders, and motors. Arduino Mega2560 and an L298N driver circuit are used as the main controller and motor driver respectively. Total cost is calculated as 65.44 USD. A detailed table for the cost of the components can be seen in Table 3.1 and experimental setup is shown in Figure 3.16.

The aforementioned PID based control algorithm is coded into Arduino Mega2560 board to evaluate the complete system. A sequence of control signals for both position and stiffness are sent to the controller. The position control signals are formed as 10 seconds step inputs with 10° shifts between $+30^\circ$ and -30° . On the other hand, stiffness values are fed by two different values resulting in a square wave. As it can be seen from Figure 3.17(a), the mechanism follows the reference inputs successfully with an RMS error of 4.20° . In contrast, Figure 3.17(b) and (c) show the rotation pulley angles in terms of stiffness. Although the stiffness values fluctuate based on the change in the control inputs, the error decreases noticeably to a certain level. The RMS error values of VRPs are 7.34° and 5.68° . It is worth to note that controllers restrict the mechanism motion with an error of $\pm 2^\circ$ because of the excessive amount of friction in the gearbox.

3.4 External F/T Estimation

Sensing external effects plays a key role in interaction with the environment in robotics. Although the highly accurate and expensive force/torque sensors are commercially

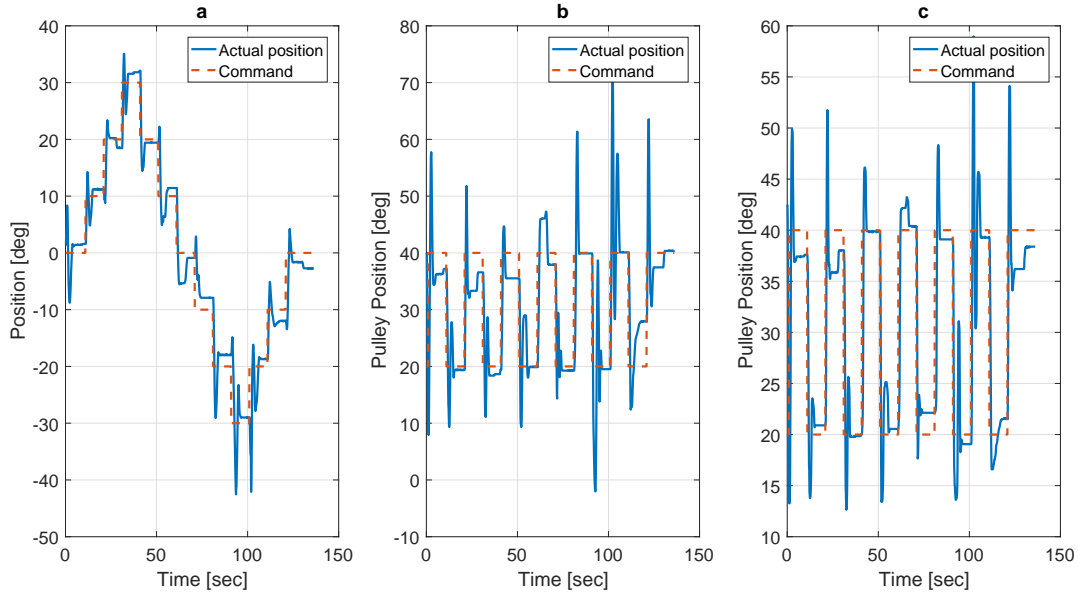


Figure 3.17 : Control scenario outputs: a) Joint position control, b) Left pulley stiffness control, c) Right pulley stiffness control.

available, elastic robot joints can provide a basis for estimating the external F/T due to its deformations besides their safety and energy-efficiency advantages. As it is mentioned in Chapter 1, human muscles have also the perception of exerted forces on themselves, through the spindle organs. In this section, three different methods are presented to estimate external F/T by taking the deformation measurements into consideration. In addition to increasing the resemblance with the human muscle functions, external F/T estimation brings the ability to acquire information about the contact environment in a cost-efficient way. Before detailing the methods, a literature survey is presented in the remaining part of this section to have a better insight into the state-of-the-art techniques in external F/T estimation in robotics. Following the literature, the slight modifications in the experimental setup, which are applied to increase the quality and variety of measurements, are revealed. Next three methods are explained in detail. Finally, the experimental results are given and discussed.

Estimation of non-measurable states by using the other measurements is a prominent problem in robotics; the algorithms attempting to solve this problem are called as the observer. A deterministic observer takes measurements as input, and by the help of the system model, it returns the estimations of the states which are not directly measured. It models the system as a random process, the groundbreaking observer method Kalman Filter (KF) [111] has achieved remarkable results, which is mostly used in filtering,

estimation and signal processing. However, the original theory deals with the linear systems, numerous variants are derived appropriate for nonlinear systems. Extended Kalman Filter uses a linearised model at the most recent estimate. Among its various applications in robotics area, far fewer applications utilize the algorithm to estimate external disturbances. In [112], external torques are estimated for 1 DOF flexible robot through the measurements of a joint torque sensor with EKF. Similarly, EKF algorithm is applied to the same problem in [113], based on the measurements of tip position, reflecting the shape of the robot, for a hyper-redundant flexible mechanism. In fact, instead of the motor current measurements [114] in rigid robots, the shape modification or the deformation has been used for this purpose in the elastic robot, but the measurements are essentially not practical. For example, the shape of the hyper-redundant structure is measured by the vision in [115] and magnetic trackers [116].

Disturbance observer (DOB) is a tool to compensate undesirable external effects by using filters [117]. Explaining the importance of tuning filter bandwidth, the purpose of DOB is defined as to compensate uncertainty in the system in [118] and [119]. Since most of the systems are nonlinear using DOB such as the SEA, the performance of DOB is evaluated in [120]. For various compensation and estimation necessities in different systems, variants of the method are derived and named according to their intention of use. For example, in [121] and [122], reaction force observer (RFOB) and three degrees of freedom control based multiple disturbance observers (TDOF-DOB) are proposed to compensate for disturbance effects from the environment and modeling errors. Additionally, in [123], another variant which is concentrated on solely estimation of external effects, such an observed named 'external force observer' EFOB is applied on a surgical tool within a similar experimental setup to present one in this chapter. The method is used to estimate external F/T in particularly where safe human-robot interaction is required while having limited space for an extra sensor such as in a surgical robot [123] and an exoskeleton system [124].

Beyond the filter and observer approaches, one can treat the problem as function approximation. Artificial neural networks (ANNs) are inspired by the biological neural networks constituting the human brain; approximates a highly nonlinear function to a given dataset or in other words "learn" the input-output relation. Its model-free nature

is superior to the model-based methods in terms of modeling errors and uncertainties in the measurements due to the dynamic working conditions. The study in [125] reveals that the success of ANNs to handle nonlinearities in dynamical systems. In [126], successful tracking results of a 2 DOF robotic are shown although the performance of ANN substantially depends on quality and quantity of the data. Similarly, [127] trains a neural network with two hidden layers to estimate the payload of a series manipulator using trajectory data for both single joint and multi-joint cases. Moreover, ANN-based F/T observers using only position and torque data are presented in [128], in order to estimate the contact force without expensive devices.

Treating the estimation problem from three different perspectives; filtering, application of stochastic observer/sensor fusion and function approximation/regression, powerful tools in robotics are evaluated in this section. KF and EFOB are preferred to detect the environmental effect and estimate external F/T value in the VRP-VSJ mechanism, by using system model and encoder measurements. Due to the simple design of the mechanism, KF is applied to the linear system with three states. Furthermore, to increase the estimate accuracy, multiple EFOBs are used for each VRPs. Beyond acceptable force/torque estimation, tracking and control instances of ANNs using simulation and/or measured data from various sensors in robotic systems, this study proposes to estimate external force/torque values of a VRP-VSJ mechanism using solely measured encoder data with ANN models.

3.4.1 Modifications in experimental setup

The estimation experiment is performed by using the VRP-VSJ mechanism, yet with three slightly modifications which are not in concept but implementation. First one is related to the data augmentation, considering the importance of the data for ANN method. Two encoders are coupled to the DC motors to be used in the model-free method so that influence of an increase in the data dimension to the accuracy can be observed. The second modification is about the hysteresis of VRPs. An idler pulley is assembled to the outlet point instead of Teflon tube. In addition to this replacement, a small piece of helical spring is substituted the original torsional spring to avoid the friction between adjacent coils. By taking these cautions, the hysteresis uncertainties in new agonist-antagonist VRPs are not completely disappeared but reduced to an

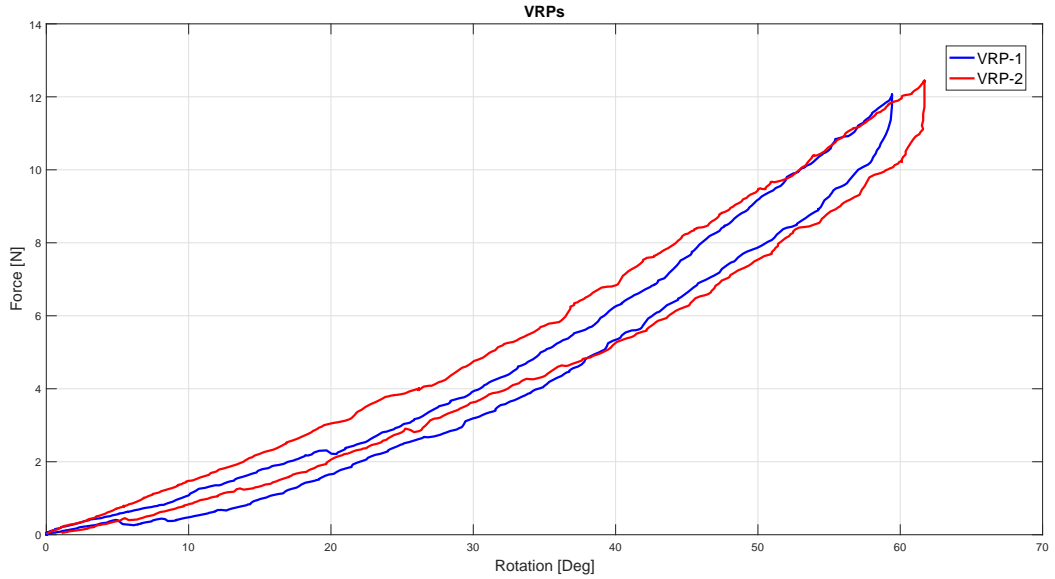


Figure 3.18 : Force-rotation curves for VRPs.

acceptable level. As a result of the capability of measuring only the pulley rotation on VRP-VSJ setup, the force-rotation curve is given in Figure 3.18. The final one is the addition of load cell to the experimental setup which serves as ground truth.

3.4.2 The estimation methods

The estimation approaches presented herein is divided into two categories: i) model-based and ii) model-free methods. The first category consists of KF and EFOB methods. These methods are supposed to use a dynamic model of the system; however, due to the negligible inertia and acceleration terms, a quasi-static model is taken into consideration which neglects the first term in the equation (3.31). The second category includes ANN method to constitute a regression model. To make a fair comparison between the algorithms, few free parameters to be decided in model-based methods are optimized using training data as ANN does for an excessive amount of parameters. At the end of the experiment, the same test data, which are entirely different than the training, are used in comparison for three methods.

3.4.2.1 KF approach

According to the linearity of the system model, KF method is implemented to estimate external F/T. The method is defined in two steps: i) prediction via system model and

ii) estimation w.r.t. measurements. To be consistent with the literature, this method is presented with the notation as used in [129].

The rotation of both pulleys (θ_1 and θ_2) are taken as first two states, for they yield cable tensions by using look-up table, and they are directly measurable variables via encoders. The final third state is considered as the external force F_{ext} , applying directly to tip point of load cell connected between VRPs.

$$x = \begin{bmatrix} \theta_1 \\ \theta_2 \\ F_{ext} \end{bmatrix} \quad (3.35)$$

For the sake of simplicity and due to the quasi-static behavior of the mechanism, the states are assumed as constants which yields a state transition matrix (A) as given in the following equation.

States are assumed to be constant due to quasi-static behavior and simplicity which results in a transition matrix (A) as given in equation (3.36).

$$A = \begin{bmatrix} 1 & 0 & 0 \\ 0 & 1 & 0 \\ b & -b & 0 \end{bmatrix} \quad (3.36)$$

where b is defined as follows:

$$b = \frac{d_v}{d_l}. \quad (3.37)$$

Similarly to the transition matrix, the measurement matrix (H) is also simple as follows:

$$H = \begin{bmatrix} 1 & 0 & 0 \\ 0 & 1 & 0 \end{bmatrix} \quad (3.38)$$

Prediction step includes state and covariance updates as given by the following equation.

$$\begin{aligned} \hat{x}_k^- &= A\hat{x}_{k-1}^- \\ P_k^- &= AP_{k-1}^-A^T + Q \end{aligned} \quad (3.39)$$

The predicted state vector is denoted by \hat{x} where current time step is represented with $(.)_k$. The covariance matrix P is calculated with the additional process noise covariance Q . The symbol R stands for the measurement noise covariance. To complete measurement step, Kalman gain K is calculated as given by the following equation.

$$K_k = P_k^- H^T (H P_k^- H^T + \bar{R})^{-1} \quad (3.40)$$

The states and the covariance matrices are updated by using the measurements (z_k) from both encoders and the Kalman gain.

$$\begin{aligned}\hat{x}_k &= \hat{x}_k^- + K_k (z_k - H\hat{x}_k^-) \\ P_k &= (I - K_k H) P_k^-\end{aligned}\quad (3.41)$$

Proper choice of Q and R matrices are crucial for the accuracy of the method, and to specify best possible values, sequential quadratic programming (SQP) algorithm is used within the training data.

3.4.2.2 EFOB approach

EFOB is the second model-based method to obtain estimations of external F/T. Although original DOB methods feedback the estimations of uncertainty and disturbance to achieve robust control, EFOB merely tries to obtain disturbance. An extraction operation and a low pass filter are executed in EFOB method to carry out this goal. Extraction operation makes a distinction between the reference input and the cable tension in VRPs. The resulting signal from the extraction operation is processed in a low pass filter (LFP) to attenuate high-frequency noise components. Since LFP cancels out the signals based upon a cut-off frequency level, the choice of the cut-off frequency level plays a decisive role and should be tuned properly. In Figure 3.19, the block diagram of the VRP-VSJ mechanism with EFOB, position and stiffness controller is illustrated.

External force equation can be easily obtained by using the block diagram of the VRP-VSJ mechanism in Figure 3.19, after achieving the cable tension forces. Estimated tension force for each VRP mechanism is calculated by the following equation;

$$F_i(s) = \frac{cf_i}{s + cf_i} (F_{ref} - f_{vrp_i}) \quad i = 1, 2, \quad (3.42)$$

where cf_i represents the low pass filter frequency value, F_{ref} indicates the computed force which is required to change the joint stiffness value. Total force is given as f_{vrp_i} which includes the system uncertainty and the external force. Moreover, computed external force is given in equation 3.43.

$$d_L F_{ext}(s) = d_v (F_1(s) - F_2(s)) \quad (3.43)$$

Two EFOBs, one for each VRPs, are used in order to estimate external F/T, and first-order LPFs are performed to retain the simplicity of the observers. The adjustment

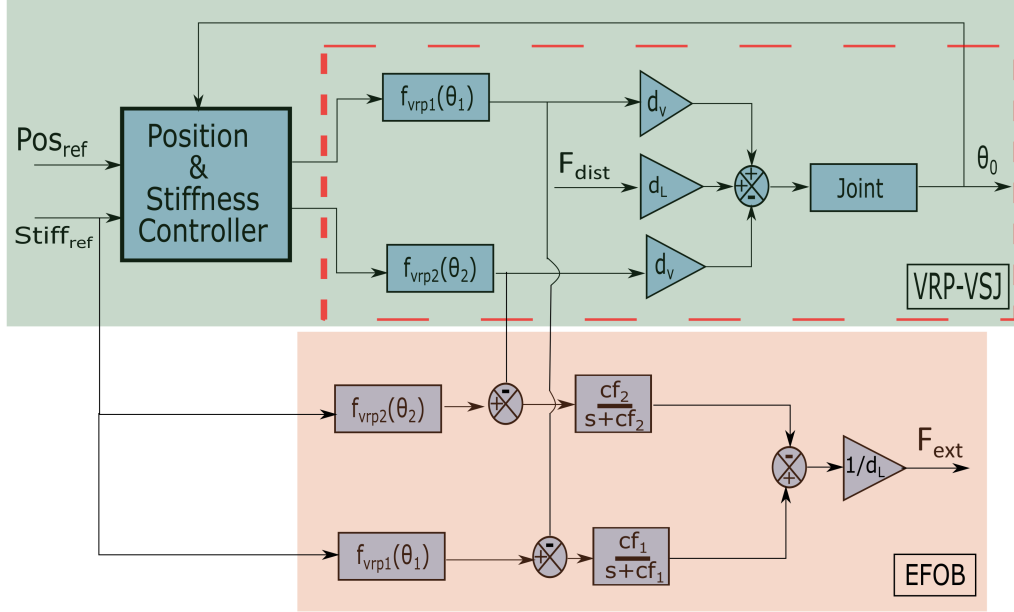


Figure 3.19 : External force observer structure.

of cut-off frequencies of the filters is treated as an optimization problem. The interior-point algorithm is executed for the training data, and the total error is tried to be minimized.

3.4.2.3 Model-free approach

ANNs are based on connected building blocks which are inspired by biological neurons, namely perceptrons, and learn a given input-output relation by optimizing the parameters by the help of a method called backpropagation. The perceptrons, which can be seen in Figure 3.20, they consist of inputs, weights, bias term, activation function and the outputs. The formulation of a single perceptron is given as follows:

$$y = \sum_{i=1}^n x_i * w_i + b \quad (3.44)$$

where x_i s stand for the inputs, w_i s, b and y denote the weights, the bias term, and the outputs, respectively. The weights are initially set small random numbers before the start of the learning process, and they are updated backpropagating the errors. Similar to other numerical algorithms, the learning process stops when a pre-defined performance criterion is reached such as epoch number, error rate, etc.

The model-based estimation methods are prone to errors due to the system parameter uncertainties and the assumptions made in modeling. On the contrary, it is unlikely to see these errors in the results of ANN estimations, because solely input-output data,

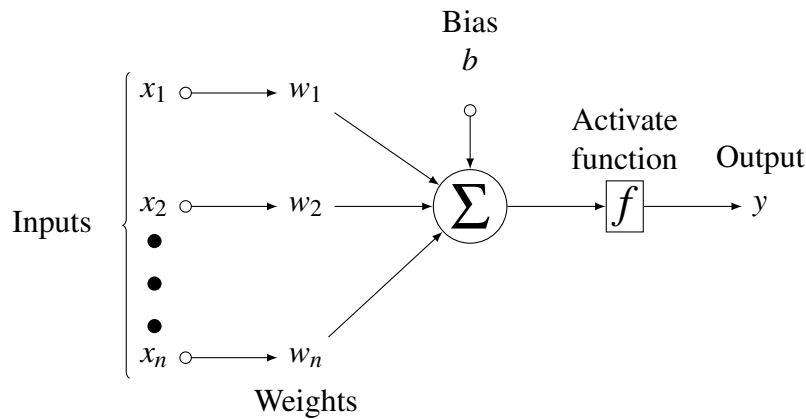


Figure 3.20 : Fundamental neuron structure.

named as training data, are fed into and modeling is left to the algorithm. Although the resulting model is not explicitly expressed, it has the ability to generate outputs when new inputs are fed. In addition to these advantages, it can cope with the noise in training data. In this study, despite the model-based methods, the hysteresis and friction involving VRP tensile test data are not used in training of ANN algorithm, the relation is inherently obtained by using only data which is collected from VRP-VSJ experimental setup. Two ANN models with respect to the number of inputs are applied to this estimation problem which is treated simply as a regression problem. The first model considers only encoders of VRPs and revolute joint as inputs. The output is the collected data from the load cell which serves as a truth-table. This model yields comparable results with model-based methods, as having the same inputs. The second model benefits from five encoders data, which takes motor encoders into account, for comparing the performance of ANN with three and five encoders.

ANN training procedure can be summed up in five steps: i) preparation of data to training, ii) feeding data to neurons for training, iii) execute the model by provided inputs until the last layer, iv) obtain results or outputs, v) backpropagation of outputs by an optimization method. The steps given between three and five are repeated until a pre-defined performance criterion is met. Preparation of the data before training is crucial for having accurate results. To be ready for the training, a standardization operation is performed to data which is rescaling the whole data with zero mean and standard deviation of unit variance as 1. This process does not change the relationship between input and output as a result of treating all data together. After this process, input signals are fed into ANN model; activation functions decide how they pass

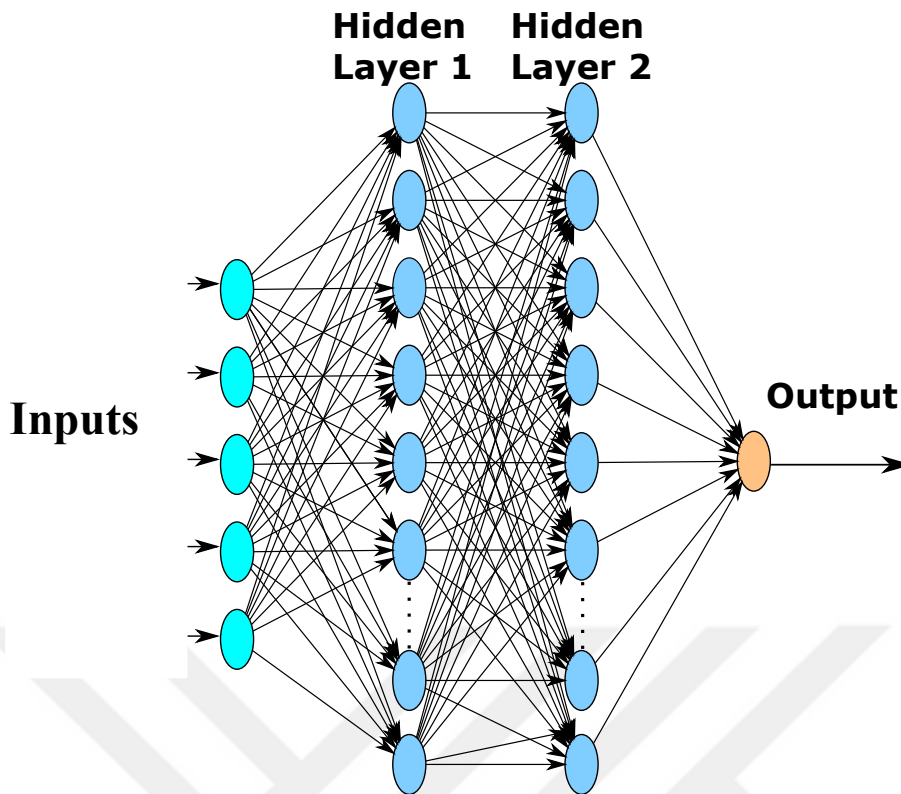


Figure 3.21 : Relation between the system and artificial neural network model.

through the neurons. In the end, the outputs are generated; thus the accuracy is determined by a loss function. In case of over an expected accuracy is obtained, then the training process is terminated.

3.4.3 Results

The experiment within this study is conducted by sending the control signals as a specified motion and stiffness profile for 175 seconds. Despite the fact that the experiment carried out continuously in one-piece, the first 120 seconds includes a motion pattern that starts from an initial position of 0° according to the joint and sweeps a range between $\pm 30^\circ$ with 10° increments/decrements. While the positions of VRPs are changed by 20° and 40° repetitively, that causes the variation in the joint stiffness. The system attempts to preserve its initial position with constant stiffness for the last 55 seconds. The encoder measurements belong to the experiment as being 5 angle values can be seen in Figure 3.22. During the experiment, random forces are applied to the system onto the tip of load cell so that they are measured directly to be ground-truth data.

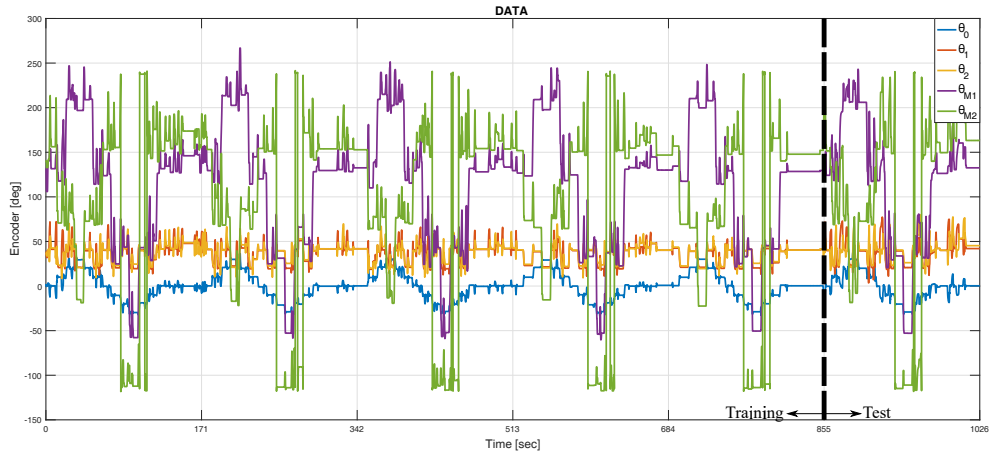


Figure 3.22 : Encoder measurements used as the training and test data.

Model-based methods estimate external F/T via three encoder inputs and the linear model of the system. Parameters of Q and R matrices are optimized by using training data to minimize the estimation error. The concluding matrices are $Q = [0.0009 \ 0.0026 \ 0.1]^T$ and $R = [0.0066 \ 0.0137]^T$. Similarly, the optimization results of first-order LPFs in EFOB equal to 0.3312 for cf_1 and 0.3718 for cf_2 .

The final ANN model has three input features and is composed of 2 hidden layers having 100 neurons at each hidden layer with "relu" as activation function for each neuron with "purelin" at output neuron. The loss function of the model is mean square error (MSE), and Levenberg-Marquadt method is used as the optimizer.

Model-based methods are implemented in Matlab and Matlab Simulink software. Since training on a single CPU takes the excessive amount of time, our ANN models are trained on a laptop computer with a CPU of Intel i7 and a GPU of Nvidia GTX-570m that runs Linux Ubuntu 16.04. We implemented the codes with Keras, which is a high-level neural networks library, written in Python and runs on top of Tensorflow. In Figure 3.21, the 5-input ANN model is symbolically represented. Correspondingly, the 3-input ANN model can be obtained by excluding the last two input features. The results of the experiment are given in the Figure 3.23.

The best method according to the accuracy of the results is KF method with an RMS error of 0.1108 N. The RMS errors of EFOB method and the ANN with three encoder inputs are similar, 0.11365 N and 0.11317 N, respectively. Also, even though it is not better given in the results graphs, ANN which is trained including five encoder inputs results not better than three inputs. The five input model yields 0.13740 N and 0.13737

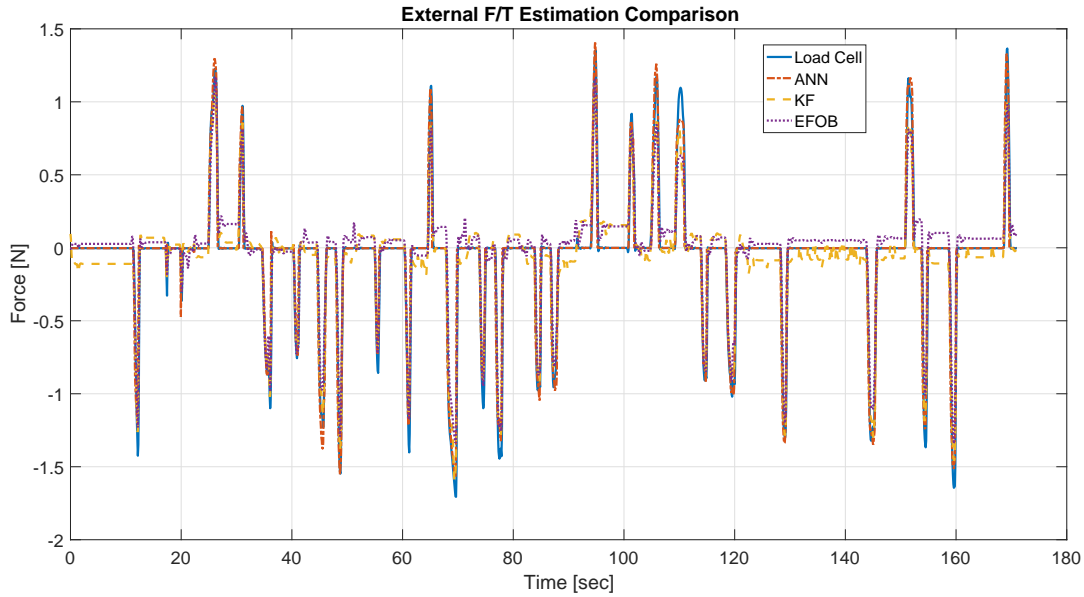


Figure 3.23 : Comparison of external F/T methods.

N for two and three hidden layers. As can be seen from the Figure 3.23, the ANN method gives very accurate results when no external forces are applied according to load cell measurements. In contrast, errors of KF and EFOB are larger when compared to ANN in the absence of external force, because of the hysteresis in VRP causes the pulleys stop in different positions. When a force is applied, the best results are obtained by KF method, especially for negative forces.

KF and EFOB methods simple, methods are simple yet effective methods for such a simple system model. When the system has more states and the linearity is lost, the KF method becomes difficult to implement in small-sized and low-cost microcontrollers, but in this study, both methods can be implemented in such a device. On the contrary, the ANN requires sophisticated hardware for both training and the estimation only collected data is enough without a model of the system, even VRP tensile test in this study. Subsequently, it is seen that the accuracies are limited with the quality of the sensors and the component of the implemented mechanism; however, the results of three methods are similar at about 0.1 N.

3.5 Conclusion

A low-cost antagonistic cable-driven VSJ mechanism design, suitable for particularly elbow and knee joints in humanoid robots, capable of 1 DOF motion and a human-like

actuation mechanism, is proposed in this chapter. The cost is reduced by a considerable amount by exploiting 3D FDM printing technology and low-cost components. Two DC motors with non-backdrivable gearboxes are responsible for the actuation of the system which brings energy-efficiency. The motors are connected to nonlinear spring mechanisms, namely VRP, in an antagonistic manner; the variable stiffness is achieved by the motions of motors together. In addition to being simple and compact, VRPs are highly versatile and can be synthesized for any custom defined force-elongation function. The synthesis of these translational nonlinear spring mechanisms is dealt with in both analytical and numerical methods. Besides the implementation guides of algorithms, a fair comparison is presented alongside with the experimental results by using a custom-built tensile testing platform. The conducted experiments reveal that nonlinear optimization based method yields minimum error for a given benchmark problem. It is remarkable that infeasible regions for specific torsional spring and force-elongation curve compels solution method to be optimization based. After comparing the results, the final VRP designs are implemented to be used in the VRP-VSJ mechanism. These VRPs are assembled in antagonistic setup to compose the VRP-VSJ mechanism. Position and stiffness control experiments are conducted on the proposed system. The agonist-antagonist structure of the system is controlled using PID and PI controllers for position and stiffness, respectively. The results of position and stiffness control experiments show successful results of controlling both attributes. Similar to human muscles, the ability of the mechanism is extended to have not only actuation but also perception. For this reason, three external F/T estimation methods are presented, i.e., KF, EFOB, and ANN. The experiments affirm that such a variable-stiffness mechanism can calculate the external effects by only measuring the deflections of elastic elements, without any additional sensor. These both model-based and model-free methods are also compared regarding their accuracy, implementation difficulties, and computation costs.

The findings highlight that such a mechanism can respond to a wide range of robot interaction tasks, which require varying compliance. Also, this study proves that the suggested synthesis methods are relevant to generate customizable VRP designs in low-cost and compact form, corresponding to various applications. In addition to VRP synthesis algorithms, the external F/T methods contribute alleviating the cost problem

by using existing sensors. The proposed mechanism provides a low-cost solution to safety, stiffness adjustment, compactness, easy-to-manufacture requirements of the current approach to humanoid robot joint designs with its simple structure. As well as being a ready solution for elbow/knee joint, it forms a basis for the next multi-DOF joint, VRP-VSJ3.



4. SHOULDER - HIP JOINT (VRP-VSJ3) DESIGN AND ANALYSIS

The joint design presented herein is the overall combination of the mechanisms explained in previous chapters. The mechanism which is presented in Chapter 3 is improved to have 3 DOF motion ability in the design. The revolute joint which connects the fixed part to moving part in VRP-VSJ mechanism is substituted with a spherical joint. With the increasing motion freedom, two cables and two motors are now insufficient to perform desired motions. As stated in [130], it is compulsory to have at least $n + 1$ cables when n DOF cable-driven mechanism is actuated. Although more number of cable can expand the workspace is reported in [131], the minimum number of cables and motors sufficient for actuation is used, since the aim of this thesis is increasing similarity with human functions while maintaining simplicity. The 3 DOF serial kinematics for neck mechanism is presented in Chapter 2, a similar approach is used in this chapter due to the similar linkages between the upper and lower plate. Unlike the CDPS mechanism, VRP-VSJ3 is fully compliant in pitch, roll and yaw axes. Therefore, the mechanism is resulting in a combination of neck and elbow mechanisms which can be employed in the humanoid robot joint requiring multi-DOF in one place.

Despite the great effort in the last decade to design VSAs with various attributes, there are only few studies on multi-DOF VSAs. Most of the multi-DOF limbs consist of serially connected single-DOF VSAs, as given in [132]. Additionally, for serial connection purposes, modular VSA designs are presented in [66]. In contrast, multi-DOF VSAs are emerging need for robotics, particularly humanoid robots, considering the human joints such as shoulder, hip, wrist, and ankle. In [131], design of a 3 DOF cable-driven VSJ module is demonstrated. Although the mechanism is similar to the mechanism proposed in this chapter, VSD is not well defined and the absence of the synthesis methods limits the mechanism implementation. Additionally, 6 cables are employed in actuation to expand the workspace in their work, additional cables necessitate extra motors; thus increases the weight, size, and cost. In contrast to VSA literature, an inspiring study is reported a cable-driven multi-DOF joint based

Table 4.1 : Cable routing map between the lower and upper plate.

Lower plate	Cable ID	Upper Plate
O_3	1	P_1
O_1	2	P_2
O_1	3	P_3
O_2	4	P_1

humanoid arm in [27]. Having less number of cables and actuators, the study in [133] obtains 3 DOF orientations with only 3 cables. The pitch and roll motions are obtained by the sum of yaw and tilt motion; which differentiates the motions of the mechanism from human natural motions.

Following the brief introduction about the joint mechanism and the literature, the mechanism proposed in this thesis is described in detail. Then the kinematic and dynamic analysis are presented. After having models, a simulation model is presented to validate the models and control approach. Consequently, the results of the simulation are drawn and the future directions are given.

4.1 Description of VRP-VSJ3

The design of the mechanism consists of the upper and lower plate, spherical joint and four motor-gearbox-capstan-cable-VRP groups. The spherical joint restrains the motions of the upper plate, enabling it to be treated as a serial mechanism during the kinematic and dynamic modeling. Four cables connect three points on both the upper and lower plate to obtain pitch, roll and yaw motions. So, there is one special point on each plate to which two cables attached, unlike the other points connecting to a single cable. The existence of these special points give 'v' and '^' shape to the cables, this allows to perform yaw motions, in other words, rotation around the longitudinal axis. On the other hand, the pitch and roll angles, rotations about 'x' and 'y' axes, are maintained by pulling and releasing of the reciprocal cables. All the motors are encapsulated in a separate box and placed under the lower plate. A schematic representation of the mechanism is as given in Figure 4.2. Additionally, since the cable routing is consequential, it is given in Table 4.1.

Considering the large range of motion of the spherical joint in three dimensions, the moment arm between the rotation center and the cables changes with the movement

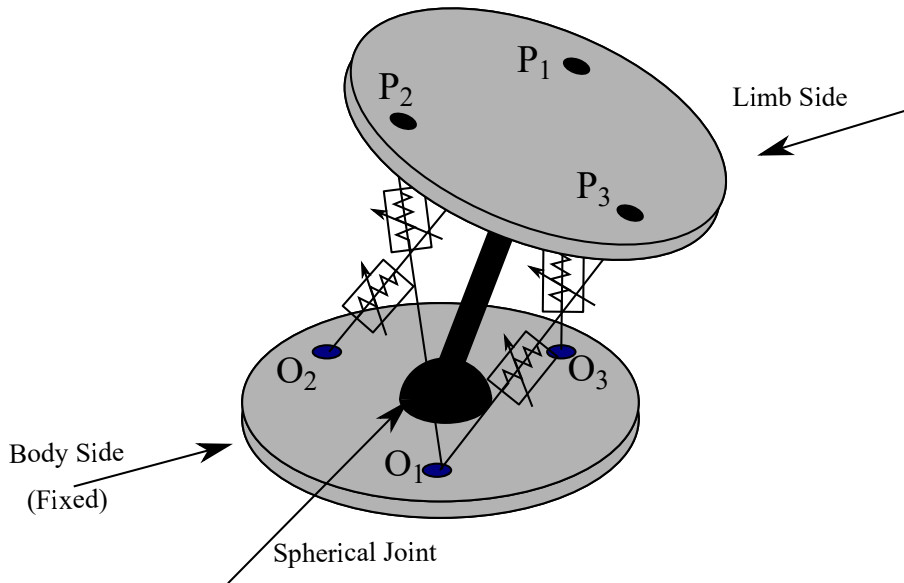


Figure 4.1 : Point and cable definitions of the lower (left) and upper (right) plate.

when joint is located between the upper plate and the lower plate. This, especially in extreme angles, reduces the ability of actuation by pulling the cable, almost or completely disables the cable that is attached to the reverse side of the rotation. In order to preserve the moment distance above a certain level, the spherical joint, as a rotation center, is positioned to the center of the lower plate. Hence, the moment arm is fixed to the distance between the center of the lower plate and the cable attachment points. In fact, although being located on the lower plate limits mechanism motion structurally, it contributes to widen the dynamically feasible workspace.

The proposed mechanism has four DOF in total; three of them are related to the compliant rotations, namely pitch, roll, and yaw. The last DOF corresponds to the stiffness of the joint. Similar to the orientation, the stiffness of the mechanism is adjusted by cable lengths. Although three stiffness values can be described around three axes, for this design, they are interdependent so that it can be assumed as only one stiffness value that is the combination of the effects of three axes. Therefore, stiffness can be adjusted in a preferred direction, and the rotational stiffness value around other axes become uncontrollable. Since four motors are connected to the system, controlling four parameters is plausible, when the system is considered as a full-actuated system. Provided that six actuators and VRPs are included in mechanism design, the stiffness in three rotation becomes controllable, detailed in [134]. The response of the human arm, however, is a stiffness change in the opposite direction to perturbations. Although experiments are carried out to show the effects of arm position

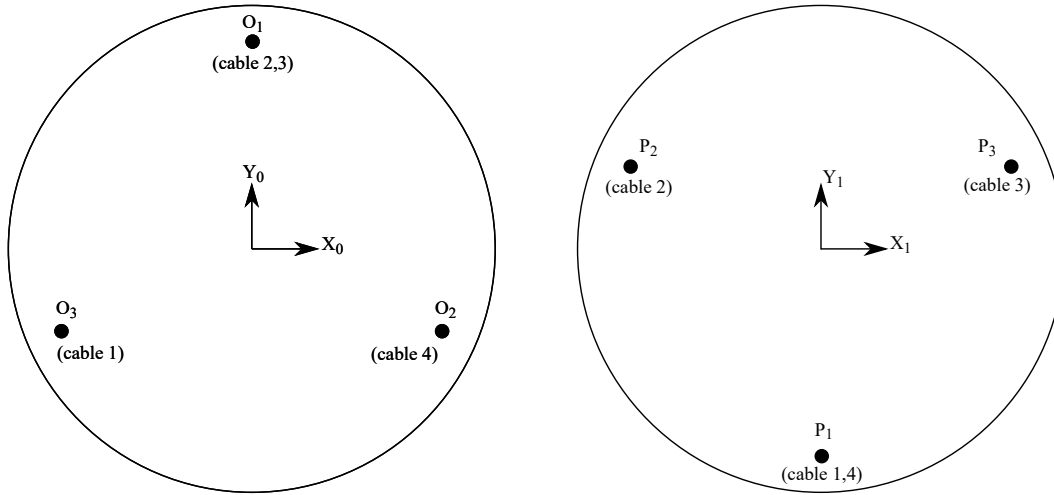


Figure 4.2 : Point and cable definitions of the lower (left) and upper (right) plate.

on stiffness change in [135] human arm stiffness characteristics during the maintenance of posture, the directional behavior can be observed from the polar stiffness ellipses. In the light of this information about the humans, controlling stiffness in a direction rather than all directions is satisfactory, when the humanoid robot motions are concerned.

The joint mechanism offers a wide range of robotic applications, especially for humanoid robots due to its compactness, simplicity, low-cost manufacturability and customizability. In addition to these advantages, the joint has multi DOF structure and preserves energy-efficiency through non-backdrivable gearboxes which do not consume energy when the joint is at rest, providing varying compliance. The cable-driven nature and non-backdrivable motors contribute to these advantages, but the VRP plays a decisive role. Since it is detailed and synthesis methods are presented with experimental results, no further explanation is given in this chapter.

4.2 Kinematic Model

Before deriving the kinematic model, firstly, the necessary variables should be defined. The output motion is described as the 3D orientation of the upper plate, as pitch (θ), roll (ϕ) and yaw (ψ) angles. The origin O_0 in the lower plate is assumed to be the center of rotation for spherical joint and the structure is completed with a link just after the spherical joint. The cable departure points on the lower plate is denoted with O_i where the index $(.)_i$ represents the point or cable identity. The points on the upper plate are shown with P_i . The cable lengths are denoted with l_i where the indices end at 4, unlike the plates. Since the spherical joint constrains the motion, the kinematic

model can be formulated by treating mechanism as a serial structure. Considering the humanoid shoulder joint, the home position in which the coinciding frames $X_0Y_0Z_0$ and $X_1Y_1Z_1$ are in entirely same configuration is assumed to be straight open arm position. The frame $X_0Y_0Z_0$ is essentially fixed to the lower plate and at rest, on the other hand, $X_1Y_1Z_1$ rotates with adjoining link. The superscript at the left top side identifies the frame in which the variable is defined. Firstly, the initial length of the cables are calculated as given in equations (4.2-4.4).

$$l_1 = |{}^1P_1 - {}^0O_3| \quad (4.1)$$

$$l_2 = |{}^1P_2 - {}^0O_1| \quad (4.2)$$

$$l_3 = |{}^1P_3 - {}^0O_1| \quad (4.3)$$

$$l_4 = |{}^1P_1 - {}^0O_2| \quad (4.4)$$

At the home position, the frame $X_1Y_1Z_1$ and $X_0Y_0Z_0$ are the same, the rotation matrix transforming variables from frame 1 to 0 is an 3x3 identity matrix, the extraction operations can be performed directly. The rotation matrix 1_0R is defined in Euler 'ZYX' convention as given in equation (4.5).

$${}^1_0R = \begin{bmatrix} c\phi c\psi & c\theta s\psi + c\psi s\theta s\phi & s\theta s\psi c\theta c\psi s\phi \\ -c\phi s\psi & c\theta c\psi - s\theta s\phi s\psi & c\psi s\theta + c\theta s\phi s\psi \\ s\phi & -c\phi s\theta & c\theta c\phi \end{bmatrix} \quad (4.5)$$

The inverse kinematic problem is the calculation of essential cable lengths to attain the desired position, for the mechanism orientation. Therefore, the requested pitch, roll, and yaw angles are substituted in the rotation matrix 1_0R to transform the positions of the points on the upper plate to the base frame.

$${}^1P_i = {}^1_0R {}^1P_i \quad (4.6)$$

Consequently, the new cable lengths are calculated by the distance between points on the upper and lower plate as given in the equations below.

$$l_{1n} = |{}^0P_1 - {}^0O_3| \quad (4.7)$$

$$l_{2n} = |{}^0P_2 - {}^0O_1| \quad (4.8)$$

$$l_{3n} = |{}^0P_3 - {}^0O_1| \quad (4.9)$$

$$l_{4n} = |{}^0P_1 - {}^0O_2| \quad (4.10)$$

The cable length adjustment is explained in the previous part, however, if the implementation is concerned, the motor shaft angles are required to be calculated

accurately. For a stiff configuration, simpler calculations than the ones used in this mechanism could be possible. The amount of motor rotations from the home position is found by directly taking the difference of new l_{in} and home l_i cable lengths. Nevertheless, great care must be taken to control motors synchronously because of the non-backdrivability of the gearboxes. A possible failure in the synchronization causes a broken cable or even a malfunctioning joint. On the other hand, the compliance in the mechanism compensates such effects, but an additional component is included in the calculations. The elongation amounts of cables in VRP ($f_{vrp,i}$) are required to be added to the cable lengths. Additionally, a chosen cable elongation is held at a constant desired position to set stiffness. Determining one of the stiffness values sets all of them implicitly, as a result of dynamic equivalence.

The forward kinematics of this mechanism also resembles the kinematics in the neck mechanism. When we have the cable lengths, and the orientation is to be calculated, gradient-descent optimization methods (like Newton-Raphson method in FK of neck) can be employed. Then the FK problem turns into an optimization problem that can be described as in equation (4.11).

$$\underset{\theta, \phi, \psi}{\text{minimize}} \sum_{i=1}^4 [l_{in} - l_i]^2 \quad (4.11)$$

4.3 Dynamic Model

The dynamic model of the system can be formulated by using the serial manipulator EOM, in general with an arbitrary actuation torque τ_a , and it is given as in the equation (4.12).

$$M(q)\ddot{q} + C(q, \dot{q})\dot{q} + G(q) = \tau_a \quad (4.12)$$

where q stands for the generalized coordinates, in vector form $[\theta, \phi, \psi]$, \dot{q} and \ddot{q} are the first and second derivatives, respectively. The actuator in the mechanism pulls the upper plate from specified points through the cables. The tension force ($F_{vrp,i}$) on the cables reflect the motor torques. As a result of having spherical joint coinciding with the lower plate, the moment arm of cable tensions fluctuates between certain levels regarding the configuration, yet never equals to zero or negative values. Therefore, the moments of each cable tension are computed as given in the equation (4.13).

$$\tau_i = {}^1\mathbf{P}_i \times \mathbf{F}_{vrp,i} \quad (4.13)$$

Skew-symmetric form of the vector product can be used to generate a mapping matrix between cable-tension-induced moments (τ_i).

$$\tau_i = \begin{bmatrix} 0 & -{}^1P_{i,z} & {}^1P_{i,y} \\ {}^1P_{i,z} & 0 & -{}^1P_{i,x} \\ -{}^1P_{i,y} & {}^1P_{i,x} & 0 \end{bmatrix} \begin{bmatrix} F_{vrp,i} s_{1,x} \\ F_{vrp,i} s_{1,y} \\ F_{vrp,i} s_{1,z} \end{bmatrix} \quad (4.14)$$

where s_i denotes unit vector along the cable direction. The $(\cdot)_x, (\cdot)_y, (\cdot)_z$ indices show x, y and z components of the corresponding vector respectively. Using the equations (4.13) and (4.14), now the mapping matrix between cable tensions and the moments in generalized coordinates can be written as in equation (4.15).

$$B = [B_1 \ B_2 \ B_3 \ B_4] \quad (4.15)$$

where B_i is defined as follows:

$$B_i = \begin{bmatrix} -{}^1P_{i,z} s_{i,y} + {}^1P_{i,y} s_{i,z} \\ {}^1P_{i,z} s_{i,x} - {}^1P_{i,x} s_{i,z} \\ -{}^1P_{i,y} s_{i,x} + {}^1P_{i,x} s_{i,y} \end{bmatrix} \quad i = 1, 2, 3, 4 \quad (4.16)$$

Consequently, the final form of the EOM is obtained as given in equation (4.17).

$$M(q)\ddot{q} + C(q, \dot{q})\dot{q} + G(q) = B(q)F_{vrp} \quad (4.17)$$

where F_{vrp} is the vector which has cable tension elements.

$$F_{vrp} = \begin{bmatrix} F_{vrp,1} \\ F_{vrp,2} \\ F_{vrp,3} \\ F_{vrp,4} \end{bmatrix} \quad (4.18)$$

4.4 Simulations

In this thesis, the simulations are not explained in detail until this chapter. In this section, how such mechanisms are modeled in a simulation environment is illustrated. Then the inverse kinematic model-based control approach is given with the simulation results.

4.4.1 Simulation environment

To analyze the mechanism motions, and validate the kinematic model with the control algorithm, simulations are performed. In this section, the simulation environment and modeling the mechanism within the environment is explained.

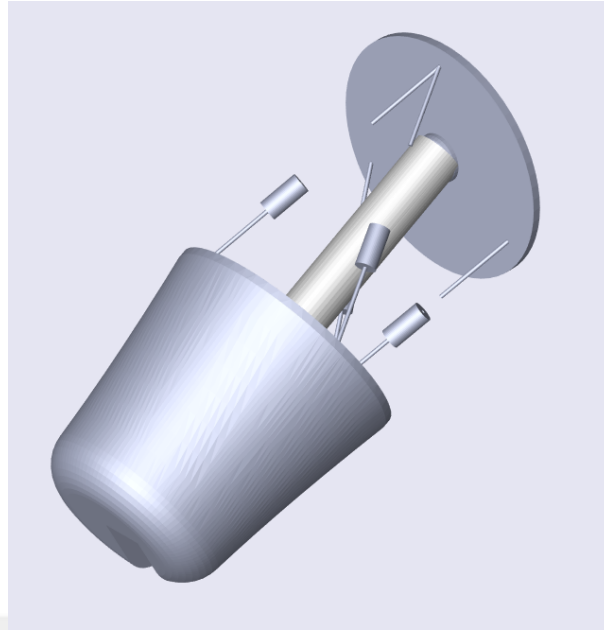


Figure 4.3 : VSR-VS3 in an arbitrary position in simulation environment.

The simulations are performed within Matlab SimMechanics software which includes various joint types, sensors, and actuators. The software is able to communicate with Matlab Simulink in which the control algorithms are also developed. Even though the mechanical definitions can be defined manually, the direct transformation from CAD model is preferred to avoid numerical errors. The simplified CAD model of the mechanism is designed in Solidworks software.

The mechanism is mainly composed of three segments, the lower plate, the adjoint link and the upper plate. The spherical joint is placed between the lower plate center and the adjoint link. The upper plate is connected to the link with a weld joint in the simulation environment. The cables, which are outside of the conventional scope, are defined as the rigid links considering the strained cables. Accordingly, the cable is modeled as the connections of three links with four joints. The cables at the attachment points on the upper and lower plate can rotate freely in three dimensions, so the connection is included in the simulation by the assumption of the spherical joint. The lower segment is connected to middle one with a prismatic joint which represents the cable wrapped around the capstan. Additionally, another prismatic joint is located between the upper segment and the middle segment, to simulate the elongation of the cable in VSR. The visual representation of the robot is shown in Figure 4.5.

The points on the lower plate (O_i) and the upper plate (P_i) are aligned around a circle with a radius of 25mm. In the home position, the distance between two plates is defined

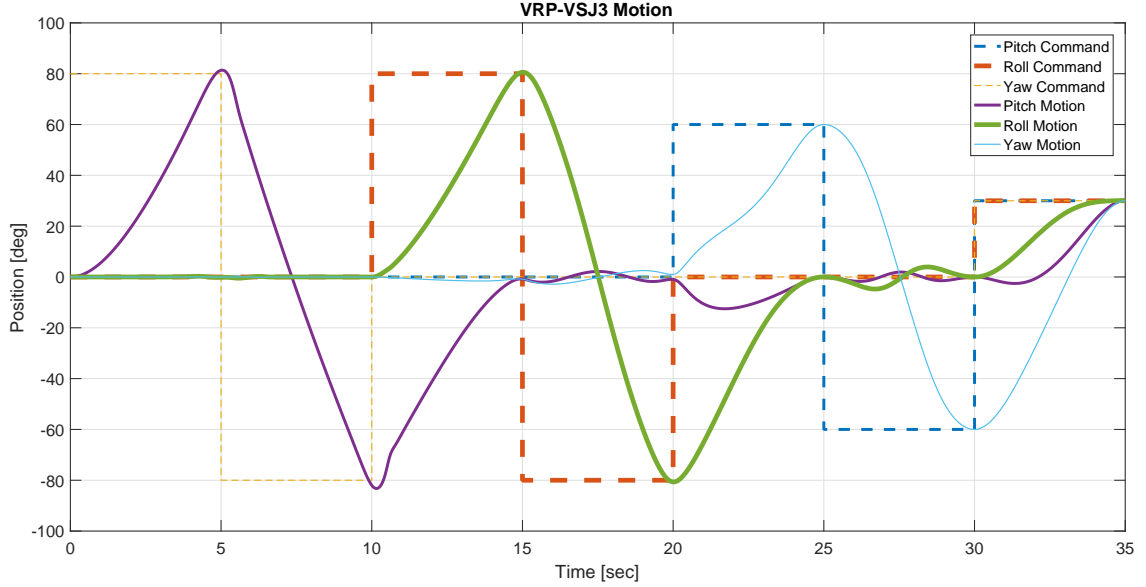


Figure 4.4 : VRP-VSJ3 simulation results.

as 55 mm. The load side is assumed to be manufactured plastic (Delrin) to define the inertial features. The VRP mechanisms in simulation is specified to show the behaviour of a quadratic spring and a linear damping. The relation between pulling force of VRP (F_{vrp}) and the elongation (u) is defined as follows:

$$F_{vrp} = u + 0.01 u^2 + 0.1 \dot{u} \quad (4.19)$$

4.4.2 Results

The inverse kinematic model based position control is applied to the simulation model of the mechanism. In order to obtain desired orientations, the inverse kinematic model given in the previous section is employed. The desired orientation parameters (pitch, roll, and yaw) are fed into the algorithm to compute necessary cable lengths between each point on the upper and lower plate. The desired orientations are arbitrary values within the workspace of the mechanism and generated as a step input with five-second durations. Once a new orientation command is sent, the inverse kinematic algorithm calculates the new cable lengths. According to these cable lengths, a cubic polynomial is fit to the trajectory to obtain a smooth motion profile. Position, velocity and the acceleration values regarding cubic polynomial is sent to joint motors connected to each cable in the simulation. The execution of motors yields an orientation change on the upper plate. The results of the simulation are given in Figure 4.4.

It can be interpreted that the mechanism performs rotations in a wide ROM successfully in accordance with the Figure 4.4. Firstly, single axis orientation commands are followed, then finally, a multi-axis rotation is completed. All the motions are carried out in five seconds, following a cubic polynomial and arriving the desired location at the end of the duration. When a task is over, the velocity becomes zero and the next task is started. The oscillations during motions are primarily influenced by the arbitrary selection of damping coefficient.

4.5 Experiments

4.5.1 Experimental setup

The VRP-VSJ3 mechanism is implemented as a humanoid shoulder joint to evaluate the performance while validating the aforementioned models. Similar components to VRP-VSJ are used in the mechanical assembly, for it is an advanced version of the 2 DOF VRP-VSJ mechanism.

The body is manufactured from PLA material with the help of FDM 3D printing technique. The same nonbackdrivable geared motors and capstans used in VRP-VSJ implementation is assembled to provide actuation. The spherical joint between the upper and lower plate is the combination of a steel ball and magnetic socket. The steel ball is subjected to magnetic field, the holding force is up to 40 N. The magnetism in the joint structure allows rotations of 180° in pitch/roll axis and 360° in yaw axis, because it eliminates the necessity of shape bonding between the socket and ball, in other words, necessity of socket to be more than a half sphere for gripping the ball. At the load side, VRP design remains same, the encoder is changed to AMS AS5048B to benefit from I2C bus which enables daisy-chain mode with connecting up to four encoders. In the daisy-chain mode, four encoders are serially connected and the encoder, in the end, is connected to Arduino Mega board. Additionally, Razor 9 DOF inertial measurement unit (IMU) is placed at the end point on the upper plate to measure the orientation of the mechanism. It is worth to note that, the IMU measurements are not included in control method, the purpose is only to evaluate the error of the mechanism in terms of orientation.

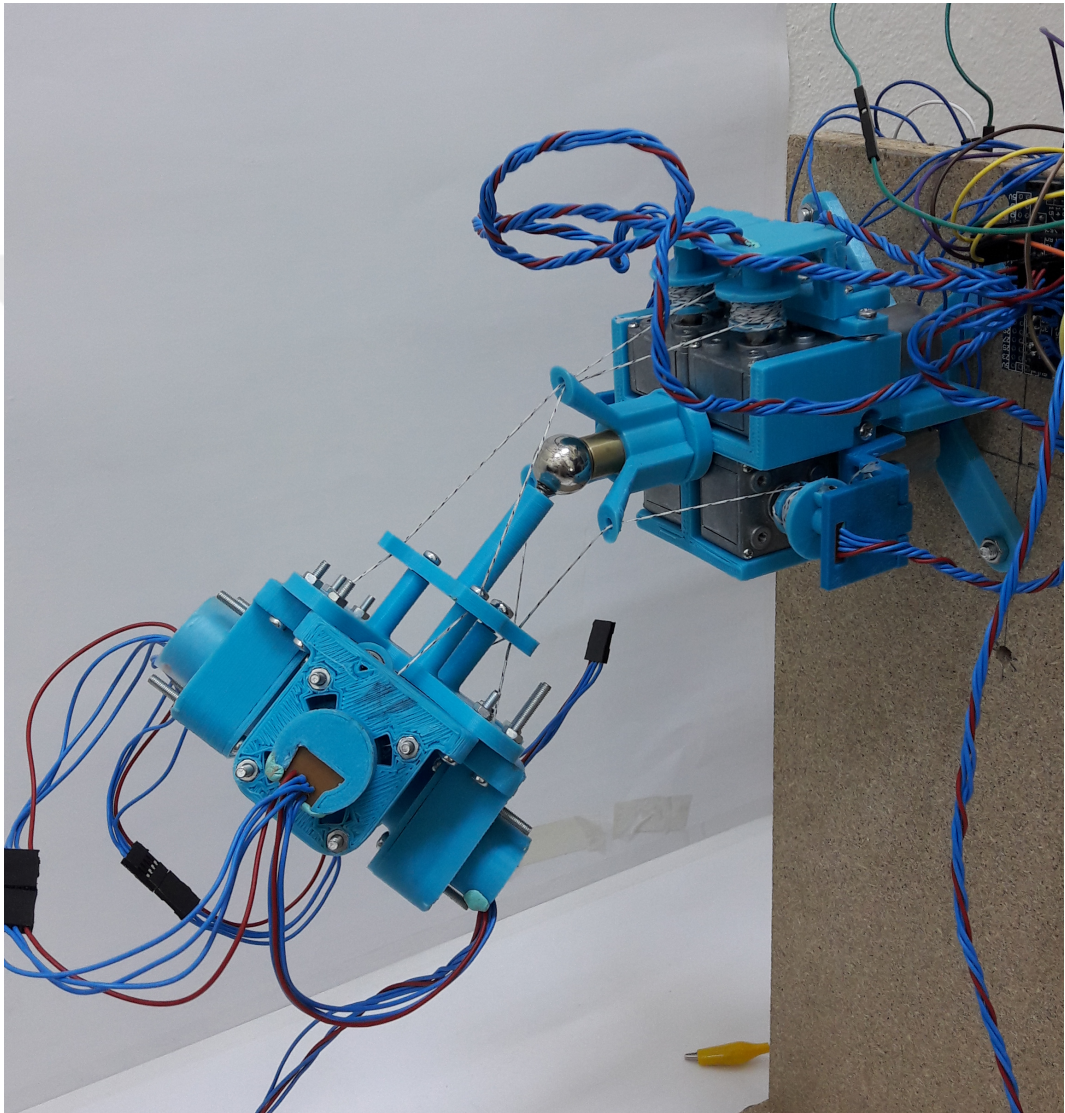


Figure 4.5 : VRP-VSJ3 experimental setup.

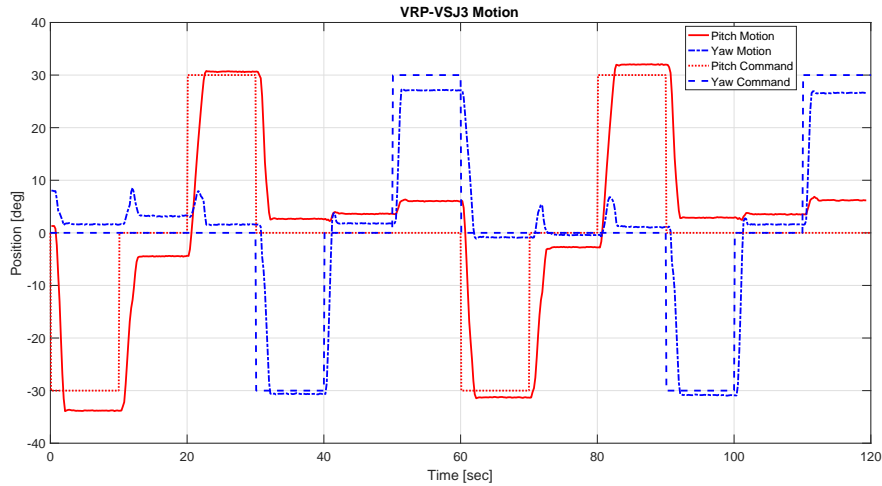


Figure 4.6 : IMU measurements in VRP-VSJ3 single-axis motion experiment.

4.5.2 Experimental results

The first experiment is carried out for single axis motions. For testing, step input commands between -30° and 30° which lasts 10 seconds are sent to the controller. After the first minute, the same inputs are sent again to analyse repeatability. Unlike the cubic polynomial trajectory generation in simulations, the experiments are based on pure PID control. When the step inputs are applied, the controller calculates the necessary motor rotations by executing the inverse kinematic model, and set reference rotations for each motor. The resulting motions of this experiment can be seen in Figure 4.6.

In Figure 4.6, the pitch and yaw motions are given with red and blue lines, respectively. The dashed lines with the same colors show the input commands. It can be seen that the mechanism can achieve desired orientations within an error range of $\pm 2^\circ$. In contrast, the mechanism cannot repeat the outputs with same inputs, when first half and second half of the figure is compared. The cause of this error can be the friction sources such as gearbox, VRPs and the points on the plates that cables pass through. Another prominent observation on this experiment is the change in the yaw position when the mechanism tends to move in the pitch axis. This error is induced by two reasons: i) control algorithm and ii) calibration failures. The control algorithm attempts to reach the desired positions without taking the intermediate points into account; this can affect the rotations about the other axes. Additionally, the determination of the home position and initial cable lengths are essential for the mechanism to perform successful motions.

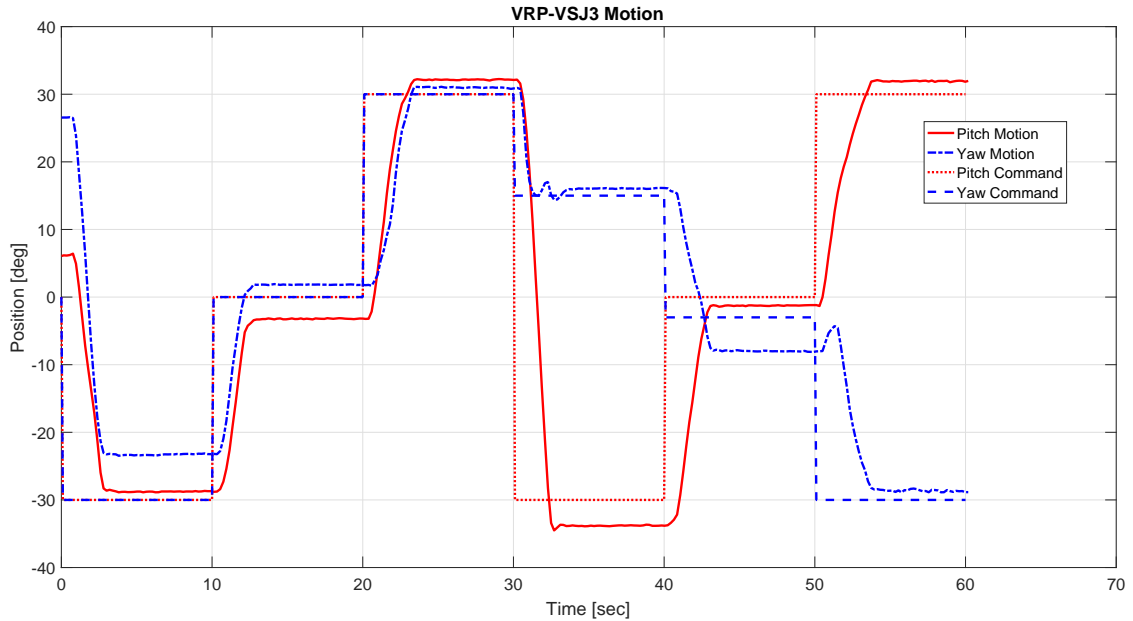


Figure 4.7 : IMU measurements in VRP-VSJ3 multi-axis motion experiment.

Deficiency in calibration may cause steady-state errors since the only feedback is the encoders for the mechanism.

In addition to the single-axis experiment, another experiment is conducted to analyze multi-axis rotations. The resulting motions of the mechanism in this test are shown in Figure 4.7. In addition to single-axis motions, the mechanism can perform multi-axis motions successfully. In Figure 4.8, each motor and VRP encoders are also presented. It can be seen from the motor position errors in Figure 4.8.(a) that PID controller eliminates errors in the motor position immediately after receiving new commands. The Figure 4.8.(b) shows the motor positions which reveals the relation between the motors and orientation when it is considered with the Figure 4.7. In this figure, home position corresponds to 0° motor angles. The positive and negative angles mean pull and release respectively. The Figure 4.8.(c) shows the measurement of the VRP encoders. As a side note, the springs are not deformed as much as in VRP-VSJ experiments, because the wire radius of the torsional spring is changed from 1.2 mm to 1.5 mm in this experiment.

4.6 Conclusion

The VRP-VSJ3 mechanism is a low-cost, compliant, variable-stiffness cable-driven 4 DOF mechanism. Additionally, the mechanism does not consume energy when it is

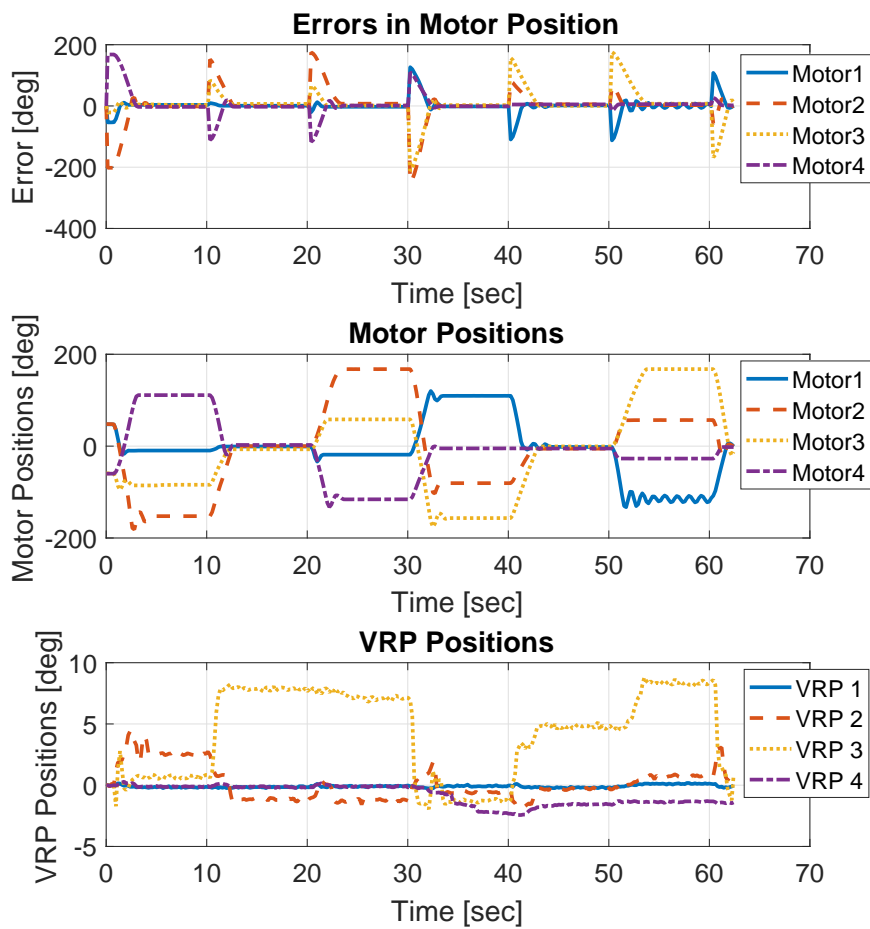


Figure 4.8 : VRP-VSJ3 multi-axis motion experiment, motor and VRP encoder measurements.

at rest due to nonbackdrivable gearbox coupled with the DC motors. In spite of the passive gravity compensation feature, the mechanism is compliant. The amount of the reaction to an external effect can be set via VRP mechanism which is customizable nonlinear spring device and detailed in the previous chapter. This property, in other words, variable stiffness, makes the joint versatile for various applications, especially humanoid robots. In addition to this, stiffness variation is a necessary feature for safe human-robot interaction. Despite these advantages, the implementation of the mechanism is easy and low-cost. All the components are off-the-shelf products and there is no advanced manufacturing techniques that are required to build the platform. Beyond these capabilities, the magnetic spherical joint in the middle of the mechanism permits a great range of motion which makes it suitable for the 3 DOF humanoid joints such as shoulder, hip, ankle, and wrist.

In this chapter, after the brief introduction about multi-DOF VSA, the proposed mechanism is described. Next, kinematic and dynamic models are given respectively. To validate the kinematic model, arbitrary orientations are obtained in the simulation environment. After the simulation part, the experimental setup is introduced. It is shown that the mechanism can complete single and multi-axis motions successfully which makes it suitable for various robotic applications, mainly humanoid robots.

As being an advanced version of the VRP-VSJ mechanism, the proposed mechanism herein has also the possibility to estimate the external F/T due to position sensors on VRPs. Furthermore, in future, the optimal design of the mechanism can be dealt with; the synthesis of VRP mechanism makes it possible. Even if it is an attempt to avoid moment arm changes by placing the spherical joint on the lower plate, there is still a variance as humans have. The change in the moment arm delimits the stiffness adjustment ability depending on the arm position. The mechanism can be improved to completely lock the distance with additional simple sub-mechanisms.



5. CASE STUDY: FEEDBACK-FEEDFORWARD CONTROL

Three joint mechanisms including revolute, universal and spherical connections with variable stiffness properties have been presented in previous three chapters. In these episodes, significant effort was spent to increase human-like functions and motion similarity. Following up the human behaviors of a humanoid robot is a two-sided problem; the first side is about the physical interaction or actuation. The other side is about intelligence/decision making. Although it is not the focus of this thesis, the decision of stiffness values is the intersection point to both sides. However all three mechanisms can adjust stiffness values, and the experimental results disclose that low-level control algorithms successfully achieve desired stiffness values, there is no algorithm to decide high-level commands to specify stiffness depending on the desired task.

Humans carry out the manipulation tasks accompanying the past experiences or intuition about the dynamics of the physical world. For example in [84], human estimations of time-to-contact in a simple ball catching task in both the World and Space where the gravity is not present. The experiments indicate that past experience with falling objects in the World conditions provisions the attitudes of humans. They fail at initial tries in space, but after a while, they adapt to no-gravity conditions in space. Similar to this study, a reaching and a slicing task are examined with a visual feedback delay to demonstrate influence in [136]. The resultant motions of human subject overshoot which can be assumed as the evidence of the existence of visual feedback; however, they adapt themselves to the situation after several tries. At the end of the experiment when the delay is removed that results in an undershot; so, the feedforward control or past experience also influences the motions. Furthermore, the anticipation of the weight of the object is prominent in manipulation tasks. In [137], the relationship between the object size/color and the estimated weight from human subjects are examined. Simple shaped objects are manufactured at the same weight but in different sizes and colors. It is observed that the human subjects fail to generate

appropriate force for smaller and brighter objects. This shows that even humans can be confused when the visual cues are illusive; however, in general, both feedback and feedforward controls affect the behavior.

State-of-the-art VSA/VIA mechanisms decide stiffness or impedance values in two distinct ways: optimization for the specified task or imitation from humans. In [138], a human wrist impedance is measured by using EMG signals and three ways are implemented on two different VIAs to imitate both position and impedance of the wrist. On the other hand, in especially explosive tasks, for example, ball throwing, the stiffness is determined by using an optimization strategy. In contrast to these two approaches, we attempt to imitate the way of human approaches manipulation problem rather than directly imitating by collecting signals from muscles or optimizing in a task-dependent way.

Rest of this chapter continues with explaining object recognition techniques from visual cues in order to acquire semantic information about the object to be manipulated. Afterwards, preparation steps and unique features of a novel image dataset which includes objects usually located on desktops and are manipulated by humans in daily activities are presented. Thereafter proposed control technique is illustrated with simulations results. Finally, the experimental setup is introduced, and the results are given with concluding remarks.

5.1 Object Recognition by DL

Computer vision algorithms seek for unique patterns stored in image pixels such as edges, corners, textures, which constitute the features as the smallest meaningful regions. In classical computer vision, the procedure of extracting features is performed in two consecutive steps as follows: *i*) The feature detection is described as obtaining the significant regions, where the highest variation in the appearance occurs, and *ii*) a feature descriptor is defined as assigning the relevant pieces of information involving size, orientation, location, color, texture, etc. to these regions. In computer vision, the object recognition problem is addressed to predict the labels of the separate items existing within the whole image. Furthermore, the object localization is to predict the bounding-box coordinates surrounding the objects properly. In other words, object recognition is the answer to what is inside the scene while object localization attempts

to find where the object is located in spatial coordinates. So that the detected features and the identical descriptors are employed to execute computer vision applications such as image aligning, stitching, etc. The main operations for a conventional computer vision can be summarized as follows in 5 steps: 1) Preprocess the input images from a convenient dataset. 2) Extract features from the inputs utilizing an appropriate feature detector/descriptor method. 3) Arrange the features plausibly for comparison and matching with each other. 4) Train a suitable classifier for recognition or regressor for localization and validate/test the performance until achieving a competent score. 5) Once the training and testing are over, then the model is ready to be deployed for instant comparisons. It is clear that conventional methods require computational intensity. Thus, they are inappropriate for real-time applications. Further detailed analysis and comparisons of the conventional feature detector and descriptor algorithms are given in [85].

In recent years, deep convolutional neural networks (CNNs) are declared for remedy the deficiencies of conventional methods that reach human-level performance scores in computer vision tasks. These type of architectures use convolution operation by sliding a filter over input images in addition to the ordinary artificial neural networks. The convolutional layer executes the mathematical operation as given in Equation (5.1):

$$\text{conv}(I, K)_{xy} = \sigma\left(b + \sum_{i=1}^h \sum_{j=1}^w \sum_{k=1}^d K_{ijk} * I_{x+i-1, y+j-1, k}\right) \quad (5.1)$$

where I is the image, and K shows the number of convolution filters, σ denotes the activation function, h, w, d indicate height, width, and depth, respectively, and x, y stand for the spatial pixel coordinates. In [139], primary deep neural networks and applications are reviewed in detail. This study states that the CNNs are better for the image, video, and speech processing applications. As long as training deep CNNs take much time even with expensive hardware, it is insufficient to train the whole networks from scratch and there exist base models for object detection and recognition those trained with great amount of data (e.g. 1.2 million images) for great number of categories (1000 classes) such as [87, 88, 140–144]. Hence, the transfer learning is asserted to employ CNNs for computer vision tasks practically because in much cases a limited number of categories are considered, and there are irrelevant object classes within base models. The transfer learning in deep CNNs is to keep earlier layers frozen, in other words stopping the learning or parameter update, and then continue

Table 5.1 : Complete object class list in ADORESET.

Ashtray	Candlestick	Fork/Spoon/Knife	Mouse	Teapot
Bag	Clock	Frying Pan	Pen/Pencil	Telephone
Book	Cooking Pot	Head Wear	Photo Frame	Vase
Bottle	Cup	Keyboard	Shoe	Wallet
Bowl	Desk Lamp	Laptop	Smart Phone	Webcam
Can	Eyeglass	Monitor	Speaker	Wrist Watch

the training of higher-level layers. The number of fixed-weight and updated layers are determined according to the number of classes and instances for each class to be used fine-tuning. In this way, the knowledge of pretrained CNN model is also employed together with the dataset concerned particularly.

5.2 ADORESET: A Hybrid Image Dataset

The accuracy of an object recognition algorithm based on ANN techniques is primarily affected by the quality of the training datasets in terms of quantity, labels, missing samples, variations, noise, outliers. Also the content of the dataset influence the performance with respect to the task dependency, in other words whether it is closely related to the task or not. For example, if the indoor objects are identified to perform a robotic mission in a house environment, then a dataset composed of outdoor images such as seas, forests, mountains is not appropriate to achieve successful results. Although there are various image datasets which are both rich in the number of classes and image per classes, there is an absence of an image dataset which mainly focuses on indoor, mainly desktop-manipulation surroundings. In this section an image data set including 30 classes which are the commonly used objects in the daily life is generated, thereby it can be used in manipulation tasks. The presented dataset is named as ADORESET, in long version annotated desktop objects real and synthetic images dataset. The complete list of the objects included in dataset is given in Table 5.1.

Construction of the dataset is started with downloading the images from search engines by using search term in multi-languages. After completing the downloads of enough number of instances for every class in the list, they are processed before training in the ANN algorithms. For this purpose, a graphical user interface, which is named as ITUrk GUI, is designed. The GUI takes the downloaded raw images and shows them



Figure 5.1 : Preprocessed real images.

to the user 24 instances at a page. Firstly, the user is asked to select delete command for irrelevant pictures with the object class. The users not only clear dataset from irrelevant images but also they provide bounding box and successor objects. As a second step in the same page, the user specifies the bounding box of all the object by left and right-clicking on the top left and bottom right corners. Finally, to acquire the semantic information about the relations of the objects, the user selects or writes the successor object name in the image if one or more exist. Then, when the user changes the page, the software saves the information received from the previous page. Preprocessed images for each class are shown in Figure 5.1.

In order to strengthen the diversity and the performance in the simulation environment, the dataset is enhanced with synthetic images. Preparation of this part begins with the downloads of CAD models for some objects like that of the real images. Since the scales of these models can vary, firstly a scaling is applied. Later, all models are oriented to have the meaningful side in the z-direction and bottom centers aligned to the origin. Following the CAD model arrangement, they are transferred to Gazebo Simulation Environment (GSE). Two prominent parameters influence the image variety in this environment. The color of the light is the first one which is adjusted by changing the sun object in GSE. The second important parameter is the 6D pose of the camera that captures the images. To obtain camera poses consistently framing the object, two nested half spheres are created around it. A random unit vector

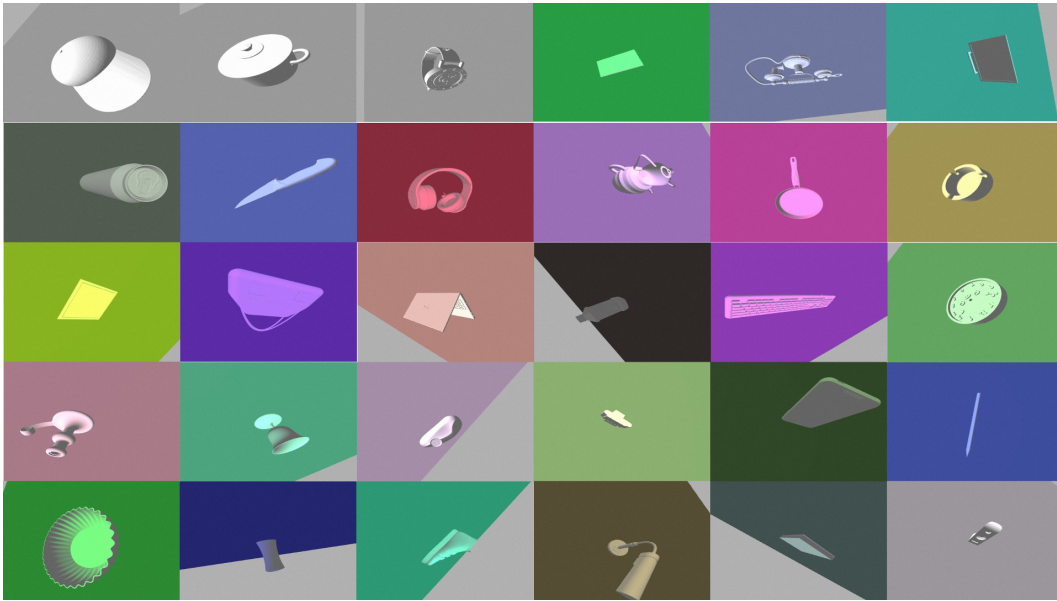


Figure 5.2 : Preprocessed synthetic images.

is generated with positive z-axis value, and it is then multiplied by an arbitrary distance value, assuring to be inside virtual volume between the spheres. The same sun is employed for 30 images whereas the poses are unique for every image. The synthetic images for each class are shown in Figure 5.2.

The dataset composed of 2500 real and 750 synthetic images for 30 classes, resulting totally 97500. All images are in RGB color format with 300x300 pixels size. The bounding boxes and successor objects are kept in separate text files with tab delimited format.

The dataset is trained through the real part and synthetic part separately, as well as together in hybrid form. Similarly, validation data composed of these combinations. VGGNet, InceptionV3, ResNet and Xception models are utilized to evaluate the performance of the dataset. All the algorithms are implemented in the Tensorflow framework. Consequently, if the train data consists of only real images, best validation accuracy for only real images is obtained by Inception V3 with 86.54%. However, the same algorithm fails to recognize objects in a hybrid (50.97%) and synthetic only (10.77%). Similar results are acquired for synthetic image training; great success for synthetic images (97.58%) and failure for others (86.54% for hybrid, and 86.54% for real). In contrast to these results, a training with hybrid dataset increases in almost all validation scenarios (86.03% for real only, 89.97% for synthetic only and 93.54%

for the hybrid). Consequently, a hybrid image dataset alongside with Inception V3 architecture performs object recognition in both real and simulation environment.

Because the main focus of this thesis is to propose novel mechanism designs and control techniques to bridge the gap between humanoid robots and humans, ADORESET, and computer vision techniques, to which partially contributed as a part of this thesis, are not presented in details; however, a more comprehensive study about this subject can be found in [145].

5.3 Proposed Control Approach

Semantic knowledge about the target object for manipulation task provides a priori data before the contact or grasp; therefore, the task can be planned including the object dynamics. Since our aim is to indicate the benefits of this approach, a very simple manipulation task is taken into consideration for the simulations and the experiments. An object which is located on a table is requested to be pushed a certain amount by the proposed variable-stiffness joint mechanism without overturning or damaging the object. To fulfill the relocation successfully, approximate object weight and center of gravity are considered to determine the joint stiffness and contact height. The proposed control block diagram is given in Figure 5.3. With reference to the figure, following the object to be put on the table, firstly, it is recognized with the help of the fine-tuned DNN models and ADORESET. A look-up table which holds the physical information about the thirty object included in ADORESET is utilized to gather the weight and the center of gravity of the object. Then required stiffness is determined according to object weight. The computer vision algorithm does not only specify the object type, but also it gives the bounding box. As a result of the depth cameras, the exact location and the height of the object is detected, and the contact point is calculated, especially in 'z' axis. The controllers of rigid Cartesian manipulator bring the end-effector to correct position while the VRP-VSJ carries out the pushing task with specified stiffness.

Considering the control structure proposed herein and the human in manipulation task, the similarities can be seen. As humans approach an identified object, they take the past experiences into account, which can be assumed as the feedforward path. Also, the shape of grasping or pushing is prominent for a successful operation; it is determined by the past experiences of the Newtonian dynamics. On the other hand, after the

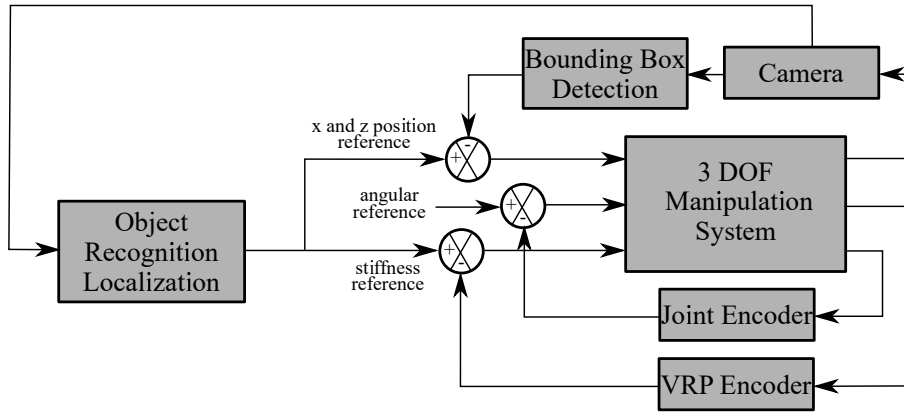


Figure 5.3 : Block diagram of the presented control approach.

contact, both the position and the F/T information is acquired by visual and tactile sensing units, and they are fed back to the main controller, brain, until the task is complete. Likewise, the proposed approach uses prior knowledge supplied by the look-up table before starting the task. Then it feeds back the visual and force data. If one of the feedforward or feedback paths are blocked, the performance of the controller either drops immediately or fails completely.

As it is stated in Chapter 3, both motors in the VRP-VSJ mechanism controls the position and stiffness independently. However, when its path is blocked, it is impossible to control the position and applied force in the same axis at the same time. Therefore, the coefficients of P controllers in both controller are considered as the weighting factors. To achieve the task, the dominance of the stiffness control is increased when compared to the position controller.

5.4 Simulations

5.4.1 Simulation environment

Unlike the simulation software used in the previous chapter, not only multi-body dynamics of the object but also the multi-object dynamics are taken into account in this chapter. Therefore, the simulations are performed in Gazebo Simulation Environment (GSE).

In GSE, a table is created to be a base for the manipulation task. Three depth cameras are located in front, right and top sides of the table. A light source is added inside the table environment to increase the image quality and avoiding shadows. A simple 2

DOF rigid robot arm is assembled to table which has the ability to move in longitudinal axis and rotation (Prismatic Revolute configuration), because of the impossibility of simulating variable stiffness joints in GSE. However, it is attainable to add any kind of sensor or motor with/without a specified amount of noise. Thus, an on-off torque control is applied to the rigid joint to resemble the VRP-VSJ mechanism.

5.4.2 Results

The objects are located at the center of the table before the simulation starts. Since the manipulation task is described as to move the visually recognized object from initial position to the desired position, first, images from depth cameras are processed, and the object is labeled by using fine-tuned VGGNet model and simplified version of ADORESET. The object location is determined via visual data; i.e., conventional color based methods favorably as a result of structured environment. Then the contact height and amount of torque to be applied to the revolute joint is determined by using the look-up table. Finally, the operation is completed with the actuation of the revolute joint. Figure 5.4 shows the simulation results. In Figure 5.4(a), the initial positions of the object on the table is shown by an image captured from the simulation environment. The labeled objects are given in Figure 5.4(b), and the images from the final position of the objects are illustrated in Figure 5.4(c). The final column in Figure 5.4 gives the position error in time.

The simulations reveal three possible cases i) successful manipulation, ii) overturn of the object due to wrong contact point determination or excessive torque application, and iii) rest at initial position regarding insufficient torque. The failures indicate the significance of the determination of correct contact point and torque.

5.5 Experiments

5.5.1 Experimental setup

To retrieve experimental results and validate the findings from the simulations, a test rig is manufactured. The test rig is composed of a 2 DOF Cartesian rigid manipulation equipment which is connected to the base of VRP-VSJ mechanism that is given in detail in Chapter 3. An end-effector arm is attached to the other end of the VRP-VSJ

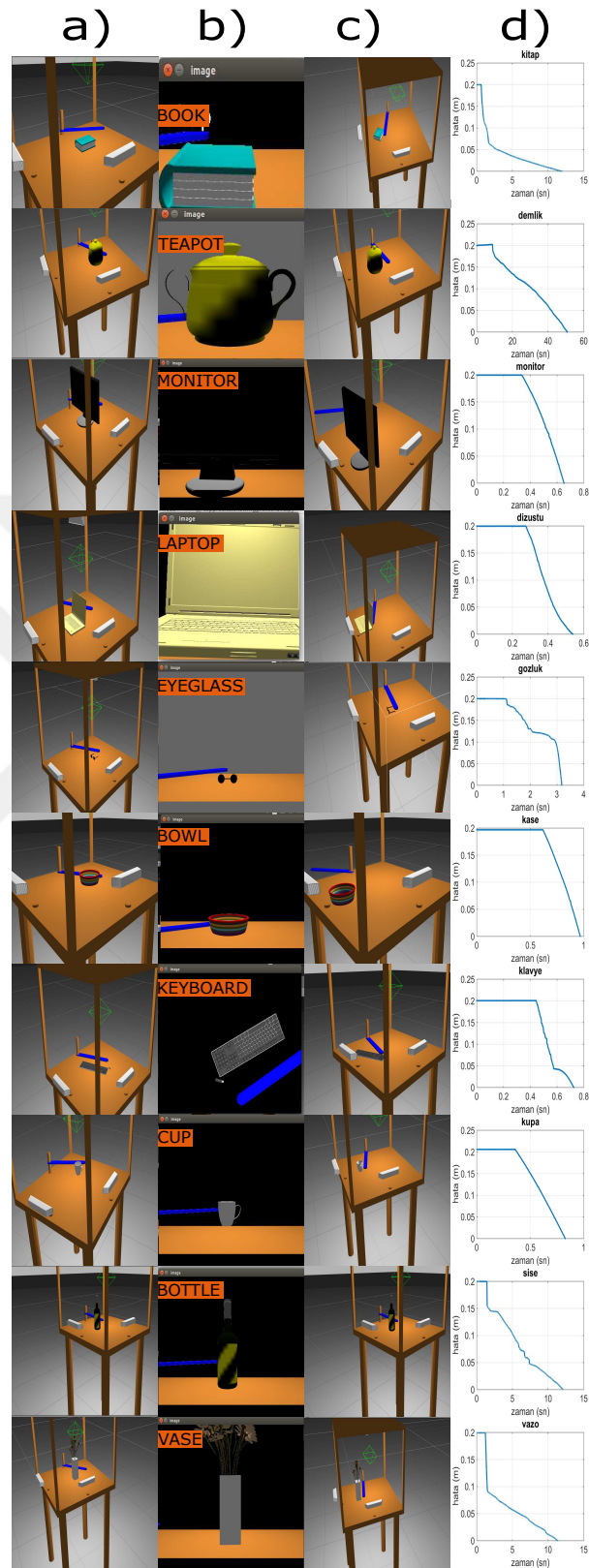


Figure 5.4 : Simulation results of pushing object via proposed control method.

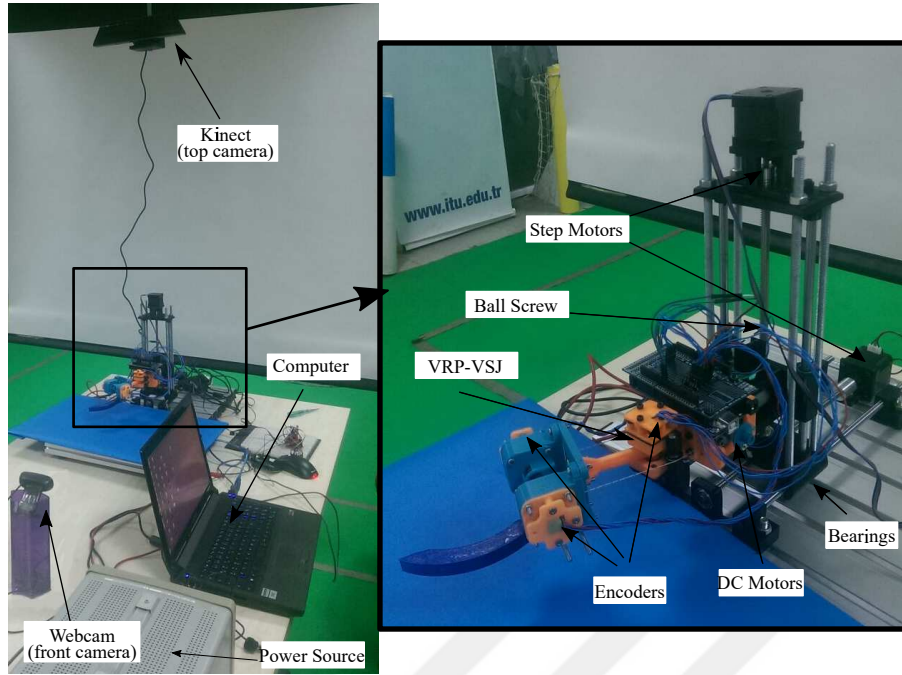


Figure 5.5 : Experimental setup to test the control method.

mechanism to exert a force on the objects with a smooth surface. The actuation of the Cartesian platform is provided by two Nema 17 stepper motors with ball-screw mechanisms, and totally 8 linear bearing supports the motion with minimum friction. An independent from VRP-VSJ Arduino Mega board is employed to control this platform.

The vision system is equipped with a depth camera and a webcam. The depth camera, which provides the height of the object, is located 100 cm above the table focusing the object from the top. Besides, the webcam is placed in front of the manipulation platform with 60 cm distance.

All the data is collected in the computer which processes and calculates four outputs; i) position, ii) stiffness of VRP-VSJ and position of the Cartesian platform in iii) x-axis and iv) y-axis. A serial port connection is preferred to transmit commands and receive sensory feedback because of simplicity.

5.5.2 Results

The experiments conducted in this section is given for five possible scenarios including combinations of faulty positioning and stiffness selection for high and low inertia objects. To demonstrate and investigate those possible scenarios, the proposed control algorithm is disrupted intentionally to generate wrong stiffness or position outputs,

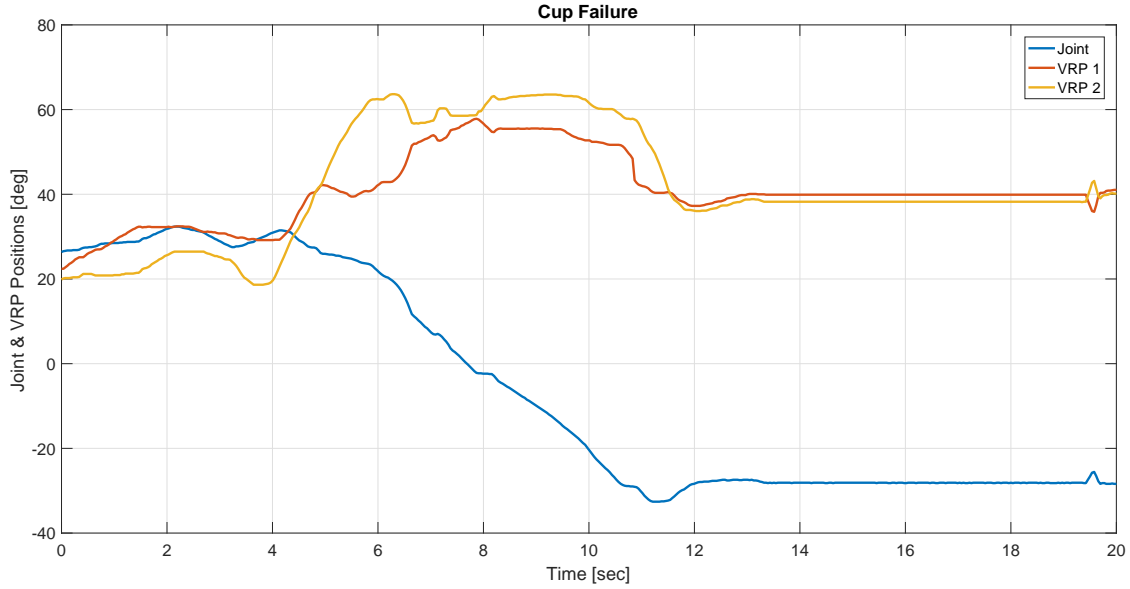


Figure 5.6 : Manipulation failure due to wrong positioning.

firstly. Then the algorithm is reset to defaults to show the performance of proposed control technique and VRP-VSJ mechanism.

5.5.2.1 Case 1: wrong positioning, manipulation failure

Even though it is a straightforward task, the contact point between the robot and the object is crucial for the pushing task. So, an experience with Newton dynamics is necessary to complete such a simple duty. While touching point under the center of gravity assures the stability of the pushing, higher points cause overturn. The data collected from the encoders of the VRP-VSJ mechanism during the experiment is given in Figure 5.6. It is worth mentioning that, the time of this figure start just before the contact moment. The contact between the object and the arm reflected in the difference of two VRP encoders. The differences between the VRPs are related to the applied force linearly, as stated in Chapter 3. Thus, it can be observed from the Figure 5.6 the contact is lost before the arm reaches desired position. In this case, although stiffness selection is appropriate for the object, herein a cup, the task fails because of the wrong choice of the contact point. The image sequence from both main camera and depth camera is given in Figure 5.7.

5.5.2.2 Case 2: wrong stiffness, low inertia, manipulation failure

The second experiment is to show how pushing task is concluded when the stiffness is set to the higher value than necessary amount for objects with lower inertias. To

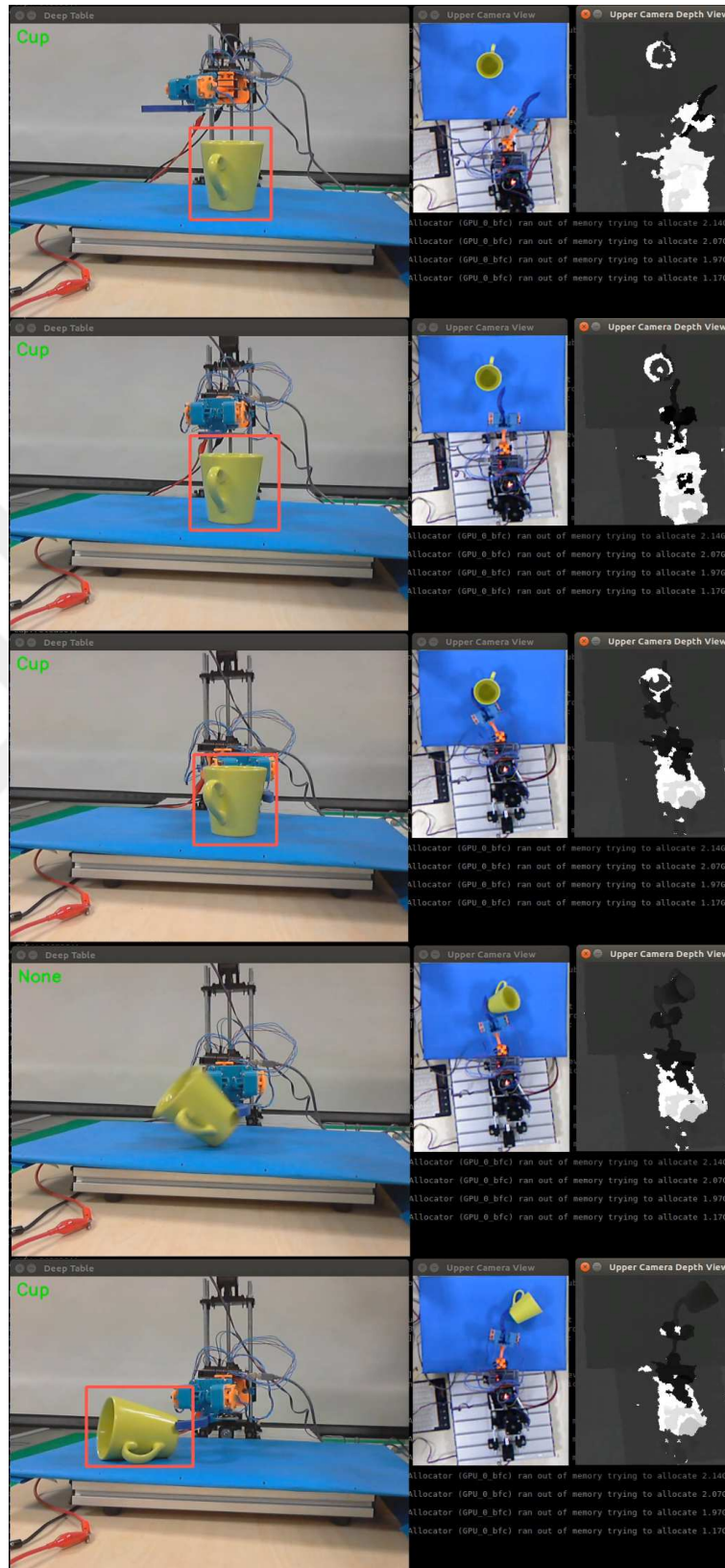


Figure 5.7 : Images from the first case.

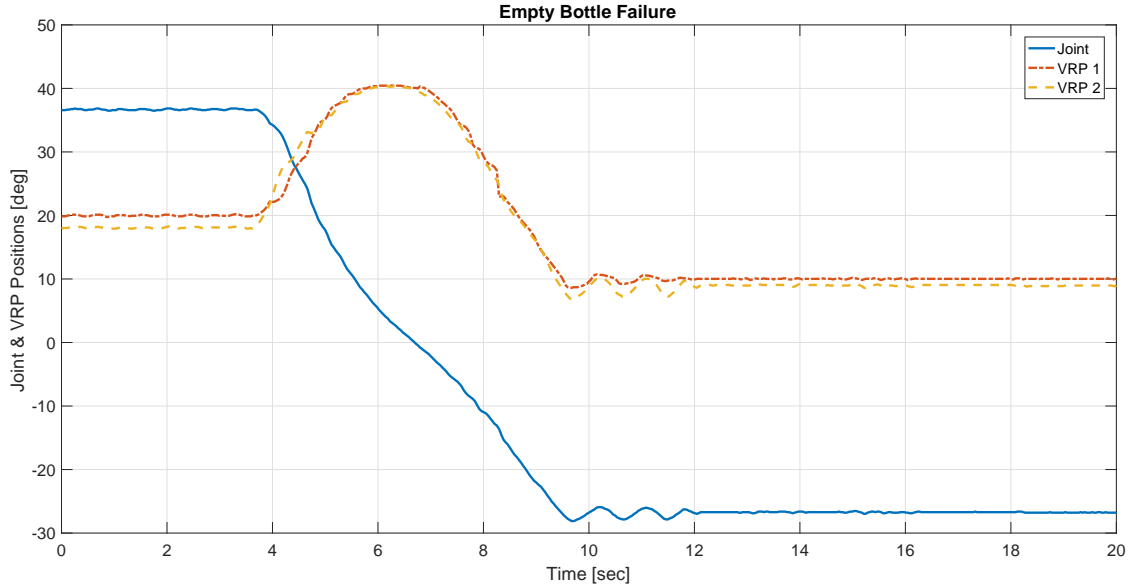


Figure 5.8 : Manipulation failure due to high stiffness.

illustrate this, an empty bottle, which is weighing a few grams, is chosen as the object to be manipulated. The results of the same procedure are given in Figure 5.8. As can be seen from the graph, the impact occurs at nearly fifth second, where the all encoder measurements intersect. At this point, the applied force does not increase with respect to encoders of VRPs. In fact, at the impact moment, the applied force is heavy enough to make contact unstable. Thus, the object overturns, and VRP-VSJ continues its motion without any further interaction.

5.5.2.3 Case 3: wrong stiffness, high inertia, manipulation failure

As well as the higher stiffness values, inadequate stiffness results in incomplete tasks. The inertia of the bottle is boosted by filling with water half of it. The outputs of the experiment are shown in Figure 5.9. After the first contact nearly at 25° , VRP-VSJ spends a great effort to push the object to the desired position. However, it can be seen that the motion of the arm stops at nearly -7° . In this experiment, the object is manually taken away to show that the arm can continue its motion when the way is not occluded with the heavy bottle. Another aspect of this is the difficulty of estimation of physical attributes of fillable objects such as bottle and cup despite the recognition of it. Even humans can fail in such a situation, indeed; they overcome this problem through feedback control.

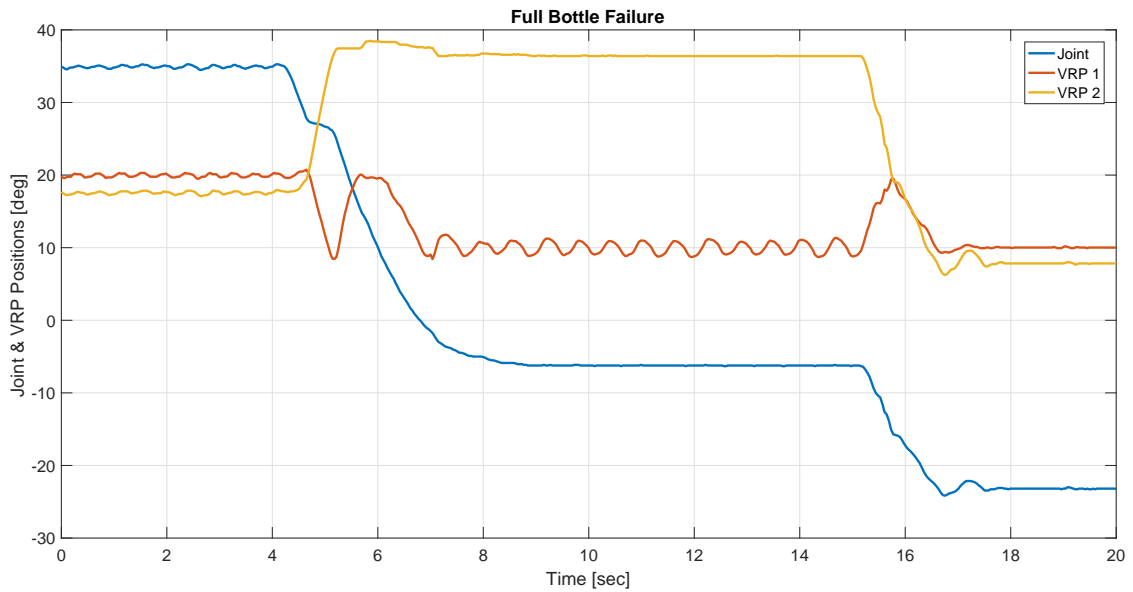


Figure 5.9 : Manipulation failure regarding low stiffness.

5.5.2.4 Case 4: correct stiffness, low inertia, manipulation success

In the last two experiments, the controller defaults are loaded to demonstrate the successful pushing tasks with the aforementioned objects. In this case, when the inertia is low, the adequate level of stiffness applies proper force to push the object safely. Figure 5.10 shows the successful experiment results. It can be inferred from the figure, during the contact phase which is between fifth and tenth seconds, the difference between both VRPs is small meaning that also the applied force is small. Since the inertia is assumed to be the priority, the motion is not completed at the desired position; nevertheless, without occlusion of the object, it can not reach that position. Thus, it can push the object as close as possible to the desired spot without harming or overturning it, which can be assumed as a successful experiment.

5.5.2.5 Case 5: correct stiffness, high inertia, manipulation success

The final experiment is carried out to show the performance of the controller when the object has high inertia, and cup is employed as the object. Figure 5.11 reveals the successful outputs of this experiment. Greater forces are applied to the object from the previous case, as can be seen from the graph. At the end of the experiment, the arm reaches the desired position, 30° .

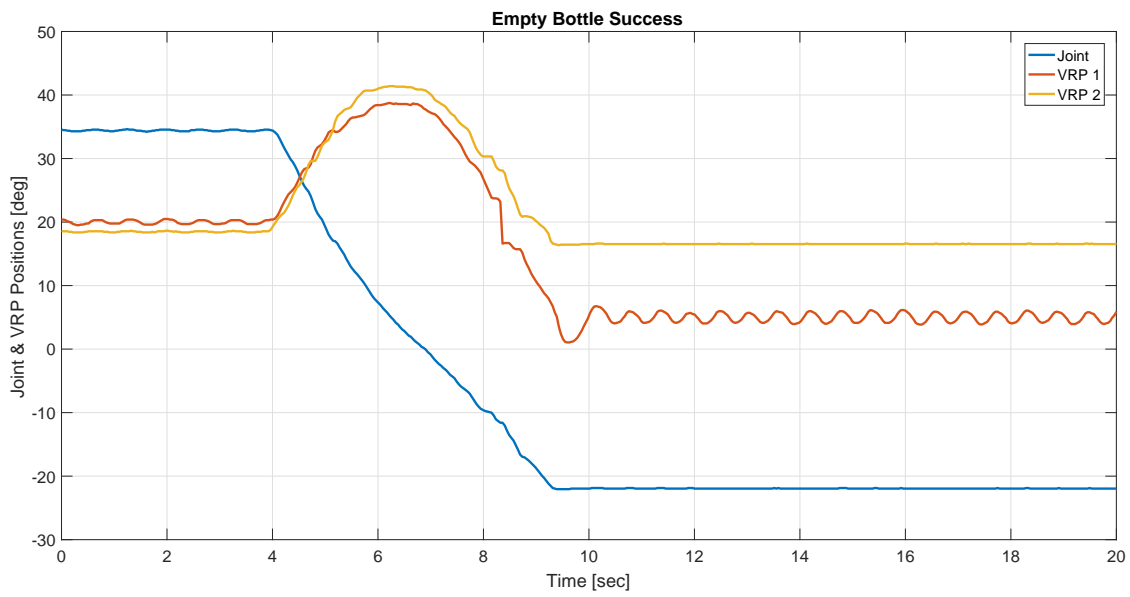


Figure 5.10 : Successful manipulation for low-inertia object.

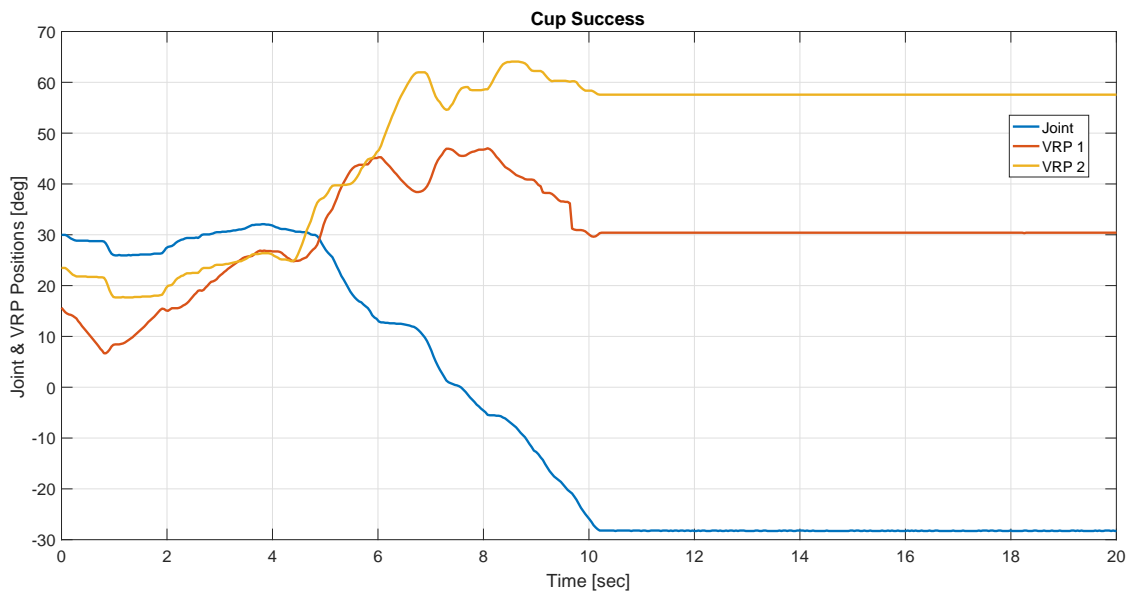


Figure 5.11 : Successful manipulation for high-inertia object.

5.6 Conclusion

In this chapter, rather than controlling stiffness at low-level for the proposed mechanisms, an attempt is presented to determine correct stiffness values which involve main control architecture as an outer loop to low-level stiffness control loops given in the previous chapters. The methodology benefits from the semantic information of the manipulated object by extracting it from contemporary visual data processing techniques. To retrieve the correct labeling, first, an image dataset is formed containing both synthetic and real object images which are frequently used object in the daily life of humans. By using fine-tuned models, the objects are first identified in the simulation environment. Following the recognition, the simple arm in simulation mimicking the VRP-VSJ mechanism is actuated to perform simple push-the-object-task. Then an experimental setup is manufactured, and the control technique is evaluated experimentally. The findings reveal that careful stiffness and contact spot determination is crucial even a simple manipulation task; therefore, the proposed method which combines the advantages of feedforward and feedback control can contribute the high-level stiffness control of such mechanisms detailed in this thesis.

The further directions of this research can be pursued including advanced experimental setup (a full arm equipped with VRP-VSJ and VRP-VSJ3s) and dexterous grasping ability. A more complicated assessment of both physical features of the objects and grasp configuration is an additional research question that can be considered for further studies.



6. CONCLUSION

Achieving the design of safe, energy-efficient and low-cost joints is one of the grand challenges in the humanoid robotics area. Besides, both following human-like motion trajectories and having a structure which is similar to musculoskeletal system are desired aspects. Additionally, considering the variety of the tasks that took place in the daily life of humans, the joint should be able to adjust its stiffness. In this thesis, three joint mechanisms, having basically different designs but the same purpose, are presented to fulfill the listed requirements of the humanoid robots for the joints of 3 DOF neck, 1 DOF elbow-knee, 3 DOF shoulder-hip/wrist-ankle. Also, stiffness variation property adds up an extra DOF to each joint.

6.1 Summary

Firstly, CDPS mechanism is presented which contains a helical spring and a universal joint with the two-part shaft and four cable-motor pairs. The behavior of helical spring resembles the human upper vertebrae/neck joint, whereas the shaft constrains the motion which makes it possible to treat the mechanism as serial-chain. The kinematics of the mechanism is analyzed according to cable lengths between two plates, and a simplified inverse kinematic algorithm is proposed assuring minimum energy consumption due to minimum spring deformations. Afterwards, the dynamic model of the system, which requires the analysis of combined compression and bending behavior of the helical spring, is presented. The models are validated through FEA method and experiments. With its suitable ROM for daily activities and stiffness adjustment ability, the mechanism is a promising solution for neck joints in humanoid robots.

Secondly, VRP-VSJ mechanism is described which is suitable for 1 DOF joints in a humanoid robot body, such as elbow and knee. This mechanism resembles the human musculoskeletal system; the motor-cable pair imitates the muscle while the VRP mechanism mirrors the functions of tendons. The artificial muscle-tendon

pair is arranged in an antagonistic manner, one for both sides of the revolute joint. Therefore, the stiffness and the position change are obtained in collaboration with both motors and VRPs. Three methods, named as analytical, optimal and numerical, are presented to synthesize VRP which acts as an energy storage element and the source of elasticity. The synthesis methods seek best possible pulley profile which determines the force-elongation curve. Next, with the synthesized VRP, the dynamics and stiffness models are given for the VRP-VSJ. Following the synthesis of the VRP and the modeling of the proposed mechanism, three algorithms are detailed, based on KF, EFOB, and ANN, to estimate external F/T via only encoder measurements. Control and estimation experiments are conducted; the mechanism is observed to show similar functions to the human musculoskeletal system, in terms of control and perception.

Finally, the advanced version of the previous mechanism, VRP-VSJ3, is presented. By adding two motors-cables-VRPs, and substituting the revolute joint with the spherical joint, the kinematic and the dynamic models of the system is formulated benefiting from the previous designs. Simulations and experiments are performed to validate the models and the control approach, yielding that four cables are adequate for achieving the desired motions successfully. Subsequently, the VRP-VSJ3 is appropriate for highly dexterous joint of the humanoid robots with respect to the magnetic spherical joint inside the mechanism which enables a great ROM.

The proposed mechanism offers various advantages to humanoid robot designers; one can summarize them as follows:

1. *Variable stiffness*: Two different stiffness adjustment strategies are applied to aforementioned joint designs. In particular, VRP mechanism is beneficial due to its versatility arising from the synthesis of the pulley according to desired force-elongation function.
2. *Compliance and safety*: Elastic components used in the system designs bring compliance and safety without a necessity for advanced force control techniques.
3. *Energy-efficiency*: Elastic elements within the mechanism support the structure; it enables to retain the position constantly without motor activity. VRP-VSJ and VRP-VSJ3 mechanisms are backdrivable mechanisms with nonbackdrivable

gearboxes which lead to passive gravity compensation and compliance at the same time.

4. *Simplicity and production easiness*: The stiffness change in the given systems is obtained by only a helical spring by benefiting its natural characteristics, or a pulley with a varying radius. All the components are either suitable for FDM type 3D printing production or off-the-shelf products.

5. *Compactness and being light-weight*: Mechanisms presented in this study requires minimum number of elements. Simplicity in the design both reduces the volume and the weight.

6. *Low-cost*: The absence of the requirement for cutting-edge motors or complicated sensors reduce the cost of the mechanism considerable amount. The structural elements are produced via FDM type cost-efficient 3D printers which also drastically reduces expenditure for this item almost to zero.

7. *Minimum backlash*: Low-cost gearbox is generally not preferred in robot joint designs because of its backlash problem. However, the pretension in the cables contributes to decrease the backlash.

8. *Modularity*: The motors beneath the upper plates of the mechanism are encapsulated and can be placed separately. In addition to that, all the joints are designed to work individually.

9. *Similarity to human joints*: The joint designs are inspired by the human musculoskeletal system and imitate their functional features.

10. *Perception of external F/T without additional sensor*: As humans can sense the external loads, the proposed mechanisms are able to estimate external effects by probing the deflections of elastic elements.

In addition to achieving the desired stiffness in the joint-level, another critical problem is to decide the stiffness value for miscellaneous tasks properly. In this thesis, a control technique is introduced which is mainly inspired by humans. In this method, both feedforward and feedback control is applied to a simplified manipulation task. The Newtonian dynamics of the Earth is transferred as pre-knowledge about the object by recognizing the object to be manipulated so that its physical attributes are obtained.

On the other hand, visual cues and force sensing ability pave the path to better stiffness adjustment ability like humans do. The conducted simulations and experiments show that the stiffness adjustment is crucial for even an uncomplicated slide-the-object task in terms of safety and accuracy.

6.2 Future Directions

The study explored in this thesis can be extended to increase similarity with human joints regarding position and stiffness. To achieve this, first, experiments can be conducted on humans to learn motion and stiffness patterns according to several daily tasks. Then, this experience can be transferred to joint designs by applying machine learning methods. Also, advanced control techniques can be applied to mechanisms to increase accuracy.

The joint designs are presented individually in this thesis; however, the other extension of this study is to investigate the behaviors when added in a successive manner. In this respect, the joint designs can be assembled to build a full limb and eventually a humanoid robot. The robot can carry the manipulation task in a better way moving the performance one step closer to human dexterity and skill and complete complex tasks with the consideration of proposed approach as a basis.

REFERENCES

- [1] **Tözeren, A.** (1999). *Human body dynamics: classical mechanics and human movement*, Springer Science & Business Media.
- [2] **Faller, A., Schünke, M. and Schünke, G.** (2004). *The Human Body: An Introduction to Structure and Function.*, Thieme.
- [3] **Pollard, N.S., Hodgins, J.K., Riley, M.J. and Atkeson, C.G.** (2002). Adapting human motion for the control of a humanoid robot, *Robotics and Automation, 2002. Proceedings. ICRA'02. IEEE International Conference on*, volume 2, IEEE, pp.1390–1397.
- [4] **Kajita, S., Hirukawa, H., Harada, K. and Yokoi, K.** (2014). *Introduction to humanoid robotics*, volume101, Springer.
- [5] **Kato, I., Ohteru, S., Kobayashi, H., Shirai, K., others and Uchiyama, A.,** (1974). Information-power machine with senses and limbs, *On Theory and Practice of Robots and Manipulators*, Springer, pp.11–24.
- [6] **Sakagami, Y., Watanabe, R., Aoyama, C., Matsunaga, S., Higaki, N. and Fujimura, K.** (2002). The intelligent ASIMO: System overview and integration, *Intelligent Robots and Systems, 2002. IEEE/RSJ International Conference on*, volume 3, IEEE, pp.2478–2483.
- [7] **Behnke, S.** (2008). Humanoid robots-from fiction to reality?, *KI*, 22(4), 5–9.
- [8] **Kaneko, K., Kanehiro, F., Morisawa, M., Akachi, K., Miyamori, G., Hayashi, A. and Kanehira, N.** (2011). Humanoid robot hrp-4-humanoid robotics platform with lightweight and slim body, *Intelligent Robots and Systems (IROS), 2011 IEEE/RSJ International Conference on*, IEEE, pp.4400–4407.
- [9] **Niemüller, T., Ferrein, A., Eckel, G., Pirro, D., Podbregar, P., Kellner, T., Rath, C. and Steinbauer, G.** (2010). Providing Ground-Truth Data for the Nao Robot Platform., *RoboCup*, Springer, pp.133–144.
- [10] **Tapus, A., Peca, A., Aly, A., Pop, C., Jisa, L., Pintea, S., ... David, D.O.** (2012). Children with autism social engagement in interaction with Nao, an imitative robot: A series of single case experiments, *Interaction studies*, 13(3), 315–347.
- [11] **Cousins, S.** (2010). Ros on the pr2 [ros topics], *IEEE Robotics & Automation Magazine*, 17(3), 23–25.

- [12] **Degallier, S., Righetti, L., Natale, L., Nori, F., Metta, G. and Ijspeert, A.** (2008). A modular bio-inspired architecture for movement generation for the infant-like robot iCub, *Biomedical Robotics and Biomechanics, 2008. BioRob 2008. 2nd IEEE RAS & EMBS International Conference on*, IEEE, pp.795–800.
- [13] **Nakanishi, Y., Asano, Y., Kozuki, T., Mizoguchi, H., Motegi, Y., Osada, M., ... Inaba, M.** (2012). Design concept of detail musculoskeletal humanoid “Kenshiro”-toward a real human body musculoskeletal simulator, *Humanoid Robots (Humanoids), 2012 12th IEEE-RAS International Conference on*, IEEE, pp.1–6.
- [14] **Albu-Schäffer, A., Haddadin, S., Ott, C., Stemmer, A., Wimböck, T. and Hirzinger, G.** (2007). The DLR lightweight robot: design and control concepts for robots in human environments, *Industrial Robot: an international journal*, 34(5), 376–385.
- [15] **Leidner, D. and Dietrich, A.** (2015). Towards intelligent compliant service robots, *29th AAAI Conference on Artificial Intelligence*.
- [16] **Mori, M., MacDorman, K.F. and Kageki, N.** (2012). The uncanny valley [from the field], *IEEE Robotics & Automation Magazine*, 19(2), 98–100.
- [17] **Koschate, M., Potter, R., Bremner, P. and Levine, M.** (2016). Overcoming the uncanny valley: Displays of emotions reduce the uncanniness of humanlike robots, *The Eleventh ACM/IEEE International Conference on Human Robot Interaction*, IEEE Press, pp.359–365.
- [18] **Wainer, J., Robins, B., Amirabdollahian, F. and Dautenhahn, K.** (2014). Using the humanoid robot KASPAR to autonomously play triadic games and facilitate collaborative play among children with autism, *IEEE Transactions on Autonomous Mental Development*, 6(3), 183–199.
- [19] **Hanson, D., Mazzei, D., Garver, C., Ahluwalia, A., De Rossi, D., Stevenson, M. and Reynolds, K.** (2012). Realistic humanlike robots for treatment of ASD, social training, and research; shown to appeal to youths with ASD, cause physiological arousal, and increase human-to-human social engagement, *Proceedings of the 5th ACM International Conference on Pervasive Technologies Related to Assistive Environments (PETRA'12)*.
- [20] **Tellez, R., Ferro, F., Garcia, S., Gomez, E., Jorge, E., Mora, D., ... Faconti, D.** (2008). Reem-B: An autonomous lightweight human-size humanoid robot, *Humanoid Robots, 2008. Humanoids 2008. 8th IEEE-RAS International Conference on*, IEEE, pp.462–468.
- [21] **Diftler, M.A., Mehling, J., Abdallah, M.E., Radford, N.A., Bridgwater, L.B., Sanders, A.M., ... Ambrose, R.O.** (2011). Robonaut 2-the first humanoid robot in space, *Robotics and Automation (ICRA), 2011 IEEE International Conference on*, IEEE, pp.2178–2183.
- [22] **Feng, S., Whitman, E., Xinjilefu, X. and Atkeson, C.G.** (2014). Optimization based full body control for the atlas robot, *Humanoid Robots*

(Humanoids), 2014 14th IEEE-RAS International Conference on, IEEE, pp.120–127.

- [23] **Pratt, G. and Manzo, J.** (2013). The darpa robotics challenge [competitions], *IEEE Robotics & Automation Magazine*, 20(2), 10–12.
- [24] **Khatib, O., Yeh, X., Brantner, G., Soe, B., Kim, B., Ganguly, S., ... Creuze, V** (2016). Ocean one: A robotic avatar for oceanic discovery, *IEEE Robotics & Automation Magazine*, 23(4), 20–29.
- [25] **Lapeyre, M., Rouanet, P., Grizou, J., Nguyen, S., Depraetre, F., Le Falher, A. and Oudeyer, P.Y.** (2014). Poppy Project: Open-source fabrication of 3D printed humanoid robot for science, education and art, *Digital Intelligence 2014*, p. 6.
- [26] **Langevin, G.** (2014). InMoov-Open Source 3D printed life-size robot, pp. URL: <http://inmoov.fr>; License: <http://creativecommons.org/licenses/by-nc/3.0/legalcode>.
- [27] **Yang, G., Lin, W., Kurbanhusen, M.S., Pham, C.B. and Yeo, S.H.** (2005). Kinematic design of a 7-DOF cable-driven humanoid arm: a solution-in-nature approach, *IEEE/ASME International Conference on Advanced Intelligent Mechatronics (AIM)*, Monterey, CA, July, pp.24–28.
- [28] **Hernández-Santos, C., Rodríguez-Leal, E., Soto, R. and Gordillo, J.** (2012). Kinematics and dynamics of a new 16 DOF humanoid biped robot with active toe joint, *International Journal of Advanced Robotic Systems*, 9(5), 190.
- [29] **McCloskey, D., Ebeling, P. and Goodwin, G.** (1974). Estimation of weights and tensions and apparent involvement of a “sense of effort”, *Experimental neurology*, 42(1), 220–232.
- [30] **Höppner, H.** (2016). Analysis of Human Intrinsic Stiffness Modulation and its Use in Variable-Stiffness Robots, (Ph.D. thesis), Technische Universität München.
- [31] **Hogan, N.** (1985). The mechanics of multi-joint posture and movement control, *Biological cybernetics*, 52(5), 315–331.
- [32] **Wickiewicz, T.L., Roy, R.R., Powell, P.L., Perrine, J.J. and Edgerton, V.R.** (1984). Muscle architecture and force-velocity relationships in humans, *Journal of Applied Physiology*, 57(2), 435–443.
- [33] **Biewener, A.A. and Roberts, T.J.** (2000). Muscle and tendon contributions to force, work, and elastic energy savings: a comparative perspective., *Exercise and sport sciences reviews*, 28(3), 99–107.
- [34] **Hogan, N.** (1984). Adaptive control of mechanical impedance by coactivation of antagonist muscles, *IEEE Transactions on Automatic Control*, 29(8), 681–690.

- [35] **Delp, S.L., Anderson, F.C., Arnold, A.S., Loan, P., Habib, A., John, C.T., ... Thelen, D.G.** (2007). OpenSim: open-source software to create and analyze dynamic simulations of movement, *IEEE transactions on biomedical engineering*, 54(11), 1940–1950.
- [36] (1995). Man-System Integration Standards, **Standard**, NASA.
- [37] **Elliott, D.M. and Allen, K.** (2017). Special Issue: Spotlight on the Future of Musculoskeletal Biomechanics: Frontiers and Challenges in Musculoskeletal Biomechanics, *Journal of biomechanical engineering*, 139(11), 110301.
- [38] **Park, I.W., Kim, J.Y., Lee, J. and Oh, J.H.** (2005). Mechanical design of humanoid robot platform KHR-3 (KAIST humanoid robot 3: HUBO), *Humanoid Robots, 2005 5th IEEE-RAS International Conference on*, IEEE, pp.321–326.
- [39] **Tadesse, Y., Subbarao, K. and Priya, S.** (2010). Realizing a humanoid neck with serial chain four-bar mechanism, *Journal of Intelligent Material Systems and Structures*, 21(12), 1169–1191.
- [40] **Brouwer, D.M., Bennik, J., Leideman, J., Soemers, H.M. and Stramigioli, S.** (2009). Mechatronic design of a fast and long range 4 degrees of freedom humanoid neck, *Robotics and Automation, 2009. ICRA'09. IEEE International Conference on*, IEEE, pp.574–579.
- [41] **Albers, A., Brudniok, S., Ottnad, J., Sauter, C. and Sedchaicharn, K.** (2006). Upper body of a new humanoid robot-the design of armar iii, *Humanoid Robots, 2006 6th IEEE-RAS International Conference on*, IEEE, pp.308–313.
- [42] **Nori, F., Jamone, L., Sandini, G. and Metta, G.** (2007). Accurate control of a human-like tendon-driven neck, *Humanoid Robots, 2007 7th IEEE-RAS International Conference on*, IEEE, pp.371–378.
- [43] **Gao, B., Xu, J., Zhao, J., Xi, N., Shen, Y. and Yang, R.** (2012). A humanoid neck system featuring low motion-noise, *Journal of Intelligent & Robotic Systems*, 67(2), 101–116.
- [44] **Stanišić, M. and Goehler, C.** (2008). Reproducing human arm motion using a kinematically coupled humanoid shoulder–elbow complex, *Applied Bionics and Biomechanics*, 5(4), 175–185.
- [45] **Ott, C., Eiberger, O., Friedl, W., Bauml, B., Hillenbrand, U., Borst, C., ... Hirzinger, G.** (2006). A humanoid two-arm system for dexterous manipulation, *Humanoid Robots, 2006 6th IEEE-RAS International Conference on*, IEEE, pp.276–283.
- [46] **Cui, B. and Jin, Z.** (2009). Accuracy analysis of a novel humanoid robot shoulder joint, *Reconfigurable Mechanisms and Robots, 2009. ReMAR 2009. ASME/IFTOMM International Conference on*, IEEE, pp.423–427.

- [47] **Stanišić, M., Wiitala, J. and Feix, J.** (2001). A dexterous humanoid shoulder mechanism, *Journal of Field Robotics*, 18(12), 737–745.
- [48] **Okada, M., Nakamura, Y. and Ban, S.** (2001). Design of programmable passive compliance shoulder mechanism, *Robotics and Automation, 2001. Proceedings 2001 ICRA. IEEE International Conference on*, volume 1, IEEE, pp.348–353.
- [49] **Gouaillier, D., Hugel, V., Blazevic, P., Kilner, C., Monceaux, J., Lafourcade, P., ... Maisonnier, B.** (2009). Mechatronic design of NAO humanoid, *Robotics and Automation, 2009. ICRA'09. IEEE International Conference on*, IEEE, pp.769–774.
- [50] **Park, I.W., Kim, J.Y., Lee, J. and Oh, J.H.** (2007). Mechanical design of the humanoid robot platform, HUBO, *Advanced Robotics*, 21(11), 1305–1322.
- [51] **Lohmeier, S., Buschmann, T., Ulbrich, H. and Pfeiffer, F.** (2006). Modular joint design for performance enhanced humanoid robot LOLA, *Robotics and Automation, 2006. ICRA 2006. Proceedings 2006 IEEE International Conference on*, IEEE, pp.88–93.
- [52] **Kaneko, K., Kajita, S., Kanehiro, F., Yokoi, K., Fujiwara, K., Hirukawa, H., ... Isozumi, T.** (2002). Design of advanced leg module for humanoid robotics project of METI, *Robotics and Automation, 2002. Proceedings. ICRA'02. IEEE International Conference on*, volume 1, IEEE, pp.38–45.
- [53] **Konno, A., Sellaouti, R., Amar, F.B. and Oueddou, F.B.** (2002). Design and development of the biped prototype ROBIAN, *Robotics and Automation, 2002. Proceedings. ICRA'02. IEEE International Conference on*, volume 2, IEEE, pp.1384–1389.
- [54] **Okada, M., Shinohara, T., Gotoh, T., Ban, S. and Nakamura, Y.** (2003). Double spherical joint and backlash clutch for lower limbs of humanoids, *Robotics and Automation, 2003. Proceedings. ICRA'03. IEEE International Conference on*, volume 1, IEEE, pp.491–496.
- [55] **Tsagarakis, N.G., Morfey, S., Cerda, G.M., Zhibin, L. and Caldwell, D.G.** (2013). Compliant humanoid coman: Optimal joint stiffness tuning for modal frequency control, *Robotics and Automation (ICRA), 2013 IEEE International Conference on*, IEEE, pp.673–678.
- [56] **Tsagarakis, N.G., Li, Z., Saglia, J. and Caldwell, D.G.** (2011). The design of the lower body of the compliant humanoid robot “cCub”, *Robotics and Automation (ICRA), 2011 IEEE International Conference on*, IEEE, pp.2035–2040.
- [57] **Lee, B., Knabe, C., Orekhov, V. and Hong, D.** (2014). Design of a human-like range of motion hip joint for humanoid robots, *ASME International Design Engineering Technical Conferences*.

- [58] **Enoch, A., Sutas, A., Nakaoka, S. and Vijayakumar, S.** (2012). BLUE: A bipedal robot with variable stiffness and damping, *Humanoid Robots (Humanoids), 2012 12th IEEE-RAS International Conference on*, IEEE, pp.487–494.
- [59] **Jafari, A., Tsagarakis, N.G. and Caldwell, D.G.** (2011). AwAS-II: A new actuator with adjustable stiffness based on the novel principle of adaptable pivot point and variable lever ratio, *Robotics and Automation (ICRA), 2011 IEEE International Conference on*, IEEE, pp.4638–4643.
- [60] **Pratt, G.A. and Williamson, M.M.** (1995). Series elastic actuators, *Intelligent Robots and Systems 95.'Human Robot Interaction and Cooperative Robots', Proceedings. 1995 IEEE/RSJ International Conference on*, volume 1, IEEE, pp.399–406.
- [61] **Vanderborght, B., Albu-Schäffer, A., Bicchi, A., Burdet, E., Caldwell, D.G., Carloni, R., ... Wolf, S.** (2013). Variable impedance actuators: A review, *Robotics and autonomous systems*, 61(12), 1601–1614.
- [62] **Migliore, S.A., Brown, E.A. and DeWeerth, S.P.** (2005). Biologically inspired joint stiffness control, *Robotics and Automation, 2005. ICRA 2005. Proceedings of the 2005 IEEE International Conference on*, IEEE, pp.4508–4513.
- [63] **English, C. and Russell, D.** (1999). Mechanics and stiffness limitations of a variable stiffness actuator for use in prosthetic limbs, *Mechanism and machine theory*, 34(1), 7–25.
- [64] **Hollander, K.W., Sugar, T.G. and Herring, D.E.** (2005). Adjustable robotic tendon using a 'Jack Spring'/spl trade, *Rehabilitation robotics, 2005. icorr 2005. 9th international conference on*, IEEE, pp.113–118.
- [65] **Sentis, L., García, J.G., Fernández, B.R., Gonzales, M. and Paine, N.** (2011). Design, construction and control of a fluidic robotic joint for compliant legged locomotion, *Industrial Electronics (ISIE), 2011 IEEE International Symposium on*, IEEE, pp.887–894.
- [66] **Catalano, M.G., Grioli, G., Garabini, M., Bonomo, F., Mancini, M., Tsagarakis, N. and Bicchi, A.** (2011). Vsa-cubebot: A modular variable stiffness platform for multiple degrees of freedom robots, *Robotics and Automation (ICRA), 2011 IEEE International Conference on*, IEEE, pp.5090–5095.
- [67] **Schepelmann, A., Geberth, K.A. and Geyer, H.** (2014). Compact nonlinear springs with user defined torque-deflection profiles for series elastic actuators, *Robotics and Automation (ICRA), 2014 IEEE International Conference on*, IEEE, pp.3411–3416.
- [68] **Tonietti, G., Schiavi, R. and Bicchi, A.** (2005). Design and control of a variable stiffness actuator for safe and fast physical human/robot interaction, *Robotics and Automation, 2005. ICRA 2005. Proceedings of the 2005 IEEE International Conference on*, IEEE, pp.526–531.

- [69] **McGeer, T.** (1990). Passive dynamic walking, *I. J. Robotic Res.*, 9(2), 62–82.
- [70] **Galloway, K.C., Clark, J.E. and Koditschek, D.E.** (2013). Variable stiffness legs for robust, efficient, and stable dynamic running, *Journal of Mechanisms and Robotics*, 5(1), 011009.
- [71] **Braun, D., Howard, M. and Vijayakumar, S.** (2012). Optimal variable stiffness control: formulation and application to explosive movement tasks, *Autonomous Robots*, 33(3), 237–253.
- [72] **Grioli, G., Wolf, S., Garabini, M., Catalano, M., Burdet, E., Caldwell, D., ... Bicchi, A.** (2015). Variable stiffness actuators: The user's point of view, *The International Journal of Robotics Research*, 34(6), 727–743.
- [73] **Wolf, S., Grioli, G., Eiberger, O., Friedl, W., Grebenstein, M., Höppner, H., ... Albu-Schäffer, A.** (2016). Variable stiffness actuators: Review on design and components, *IEEE/ASME transactions on mechatronics*, 21(5), 2418–2430.
- [74] **Van Ham, R., Sugar, T.G., Vanderborght, B., Hollander, K.W. and Lefeber, D.** (2009). Compliant actuator designs, *IEEE Robotics & Automation Magazine*, 16(3).
- [75] **Albu-Schäffer, A. and Bicchi, A.**, (2016). Actuators for Soft Robotics, Springer Handbook of Robotics, Springer, pp.499–530.
- [76] **Burdet, E., Osu, R., Franklin, D.W., Milner, T.E. and Kawato, M.** (2001). The central nervous system stabilizes unstable dynamics by learning optimal impedance, *Nature*, 414(6862), 446–449.
- [77] **Lackner, J.R. and Dizio, P.** (1994). Rapid adaptation to Coriolis force perturbations of arm trajectory, *Journal of neurophysiology*, 72(1), 299–313.
- [78] **Villani, L. and De Schutter, J.**, (2008). Force Control, Springer Berlin Heidelberg, Berlin, Heidelberg, pp.161–185, https://doi.org/10.1007/978-3-540-30301-5_8.
- [79] **Fumagalli, M.** (2013). *Increasing perceptual skills of robots through proximal force/torque sensors: A study for the implementation of active compliance on the icub humanoid robot*, Springer Science & Business Media.
- [80] **Part, S.** (1985). Impedance control: An approach to manipulation, *Journal of dynamic systems, measurement, and control*, 107, 17.
- [81] **Lim, H.o., Setiawan, S.A. and Takanishi, A.** (2001). Balance and impedance control for biped humanoid robot locomotion, *Intelligent Robots and Systems, 2001. Proceedings. 2001 IEEE/RSJ International Conference on*, volume 1, IEEE, pp.494–499.
- [82] **Wieland, S., Gonzalez-Aguirre, D., Vahrenkamp, N., Asfour, T. and Dillmann, R.** (2009). Combining force and visual feedback for physical interaction tasks in humanoid robots, *Humanoid Robots, 2009. Humanoids 2009. 9th IEEE-RAS International Conference on*, IEEE, pp.439–446.

- [83] **Zinn, M., Roth, B., Khatib, O. and Salisbury, J.K.** (2004). A new actuation approach for human friendly robot design, *The international journal of robotics research*, 23(4-5), 379–398.
- [84] **McIntyre, J., Zago, M., Berthoz, A. and Lacquaniti, F.** (2001). Does the brain model Newton’s laws?, *Nature neuroscience*, 4(7), 693.
- [85] **Bayraktar, E. and Boyraz, P.** (2017). Analysis of feature detector and descriptor combinations with a localization experiment for various performance metrics, *Turkish Journal of Electrical Engineering & Computer Sciences*, 25(3), 2444–2454.
- [86] **Krizhevsky, A., Sutskever, I. and Hinton, G.E.** (2012). Imagenet classification with deep convolutional neural networks, *Advances in neural information processing systems*, pp.1097–1105.
- [87] **Simonyan, K. and Zisserman, A.** (2014). Very deep convolutional networks for large-scale image recognition, *arXiv preprint arXiv:1409.1556*.
- [88] **Szegedy, C., Vanhoucke, V., Ioffe, S., Shlens, J. and Wojna, Z.** (2016). Rethinking the inception architecture for computer vision, *Proceedings of the IEEE Conference on Computer Vision and Pattern Recognition*, pp.2818–2826.
- [89] **He, K., Zhang, X., Ren, S. and Sun, J.** (2016). Deep residual learning for image recognition, *Proceedings of the IEEE conference on computer vision and pattern recognition*, pp.770–778.
- [90] **Schalkoff, R.J.** (1997). *Artificial neural networks*, volume 1, McGraw-Hill New York.
- [91] **Lim, W., Yeo, S., Yang, G. and Mustafa, S.** (2009). Kinematic analysis and design optimization of a cable-driven universal joint module, *Advanced Intelligent Mechatronics, 2009. AIM 2009. IEEE/ASME International Conference on*, IEEE, pp.1933–1938.
- [92] **Lim, W.B., Yang, G., Yeo, S.H. and Mustafa, S.K.** (2012). Modular Cable-Driven Robotic Arms for Intrinsically Safe Manipulation, *Service Robots and Robotics: Design and Application: Design and Application*, 274.
- [93] **Alici, G. and Shirinzadeh, B.** (2004). Topology optimisation and singularity analysis of a 3-SPS parallel manipulator with a passive constraining spherical joint, *Mechanism and Machine Theory*, 39(2), 215–235.
- [94] **Kim, J.S., Jeong, J.H. and Park, J.H.** (2015). Inverse kinematics and geometric singularity analysis of a 3-SPS/S redundant motion mechanism using conformal geometric algebra, *Mechanism and Machine Theory*, 90, 23–36.
- [95] **Leech, A.R.** (1994). A study of the deformation of helical springs under eccentric loading, (Ph.D. thesis), Monterey, California. Naval Postgraduate School.

- [96] **Ferrario, V.F., Sforza, C., Serrao, G., Grassi, G. and Mossi, E.** (2002). Active range of motion of the head and cervical spine: a three-dimensional investigation in healthy young adults, *Journal of orthopaedic research*, 20(1), 122–129.
- [97] **Bennett, S.E., Schenk, R.J. and Simmons, E.D.** (2002). Active range of motion utilized in the cervical spine to perform daily functional tasks, *Clinical Spine Surgery*, 15(4), 307–311.
- [98] **Leech, A.R.** (1994). A study of the deformation of helical springs under eccentric loading, (Ph.D. thesis), Monterey, California. Naval Postgraduate School.
- [99] **Yigit, C.B. and Boyraz, P.** (2017). Design and Modelling of a Cable-Driven Parallel-Series Hybrid Variable Stiffness Joint Mechanism for Robotics, *Mechanical Sciences*, 8(1), 65.
- [100] **Schmit, N. and Okada, M.** (2012). Design and realization of a non-circular cable spool to synthesize a nonlinear rotational spring, *Advanced Robotics*, 26(3-4), 234–251.
- [101] **Malosio, M., Spagnuolo, G., Prini, A., Tosatti, L.M. and Legnani, G.** (2017). Principle of operation of RotWWC-VSA, a multi-turn rotational variable stiffness actuator, *Mechanism and Machine Theory*, 116, 34–49.
- [102] **Fiorio, L., Parmiggiani, A., Berret, B., Sandini, G. and Nori, F.** (2012). pnrVSA: human-like actuator with non-linear springs in agonist-antagonist configuration, *2012 12th IEEE-RAS International Conference on Humanoid Robots (Humanoids 2012)*, IEEE, pp.502–507.
- [103] **Spagnuolo, G., Malosio, M., Dinon, T., Tosatti, L.M. and Legnani, G.** (2017). Analysis and synthesis of LinWWC-VSA, a Variable Stiffness Actuator for linear motion, *Mechanism and Machine Theory*, 110, 85–99.
- [104] **Endo, G., Yamada, H., Yajima, A., Ogata, M. and Hirose, S.** (2010). A passive weight compensation mechanism with a non-circular pulley and a spring, *Robotics and Automation (ICRA), 2010 IEEE International Conference on*, IEEE, pp.3843–3848.
- [105] **Cui, M., Wang, S. and Li, J.** (2015). Spring Gravity Compensation Using the Noncircular Pulley and Cable For the Less-Spring Design, *Proceedings of the 14th IFToMM World Congress*, pp.135–143.
- [106] **Kim, B. and Deshpande, A.D.** (2014). Design of Nonlinear Rotational Stiffness Using a Noncircular Pulley-Spring Mechanism, *Journal of Mechanisms and Robotics*, 6(4), 041009.
- [107] **Schepelmann, A., Geberth, K.A. and Geyer, H.** (2014). Compact nonlinear springs with user defined torque-deflection profiles for series elastic actuators, *2014 IEEE International Conference on Robotics and Automation (ICRA)*, IEEE, pp.3411–3416.

- [108] **Shin, D., Yeh, X. and Khatib, O.** (2011). Variable radius pulley design methodology for pneumatic artificial muscle-based antagonistic actuation systems, *2011 IEEE/RSJ International Conference on Intelligent Robots and Systems*, IEEE, pp.1830–1835.
- [109] **Seriani, S. and Gallina, P.** (2016). Variable Radius Drum Mechanisms, *Journal of Mechanisms and Robotics*, 8(2), 021016.
- [110] **Kilic, M., Yazicioglu, Y. and Kurtulus, D.F.** (2012). Synthesis of a torsional spring mechanism with mechanically adjustable stiffness using wrapping cams, *Mechanism and Machine Theory*, 57, 27–39.
- [111] **Kalman, R.E. and Bucy, R.S.** (1961). New results in linear filtering and prediction theory, *Journal of basic engineering*, 83(1), 95–108.
- [112] **Park, Y.J. and Chung, W.K.** (2013). External torque-sensing algorithm for flexible-joint robot based on Kalman filter, *Electronics Letters*, 49(14), 877–878.
- [113] **Rucker, D.C. and Webster, R.J.** (2011). Deflection-based force sensing for continuum robots: A probabilistic approach, *Intelligent Robots and Systems (IROS), 2011 IEEE/RSJ International Conference on*, IEEE, pp.3764–3769.
- [114] **Wahrburg, A., Zeiss, S., Matthias, B. and Ding, H.** (2014). Contact force estimation for robotic assembly using motor torques, *Automation Science and Engineering (CASE), 2014 IEEE International Conference on*, IEEE, pp.1252–1257.
- [115] **Xu, K. and Simaan, N.** (2008). An investigation of the intrinsic force sensing capabilities of continuum robots, *IEEE Transactions on Robotics*, 24(3), 576–587.
- [116] **Bajo, A. and Simaan, N.** (2012). Kinematics-based detection and localization of contacts along multisegment continuum robots, *IEEE Transactions on Robotics*, 28(2), 291–302.
- [117] **Murakami, T. and Ohnishi, K.** (1992). Observer-based adaptive force control of multi-degrees-of-freedom manipulator, *Industrial Electronics, Control, Instrumentation, and Automation, 1992. Power Electronics and Motion Control., Proceedings of the 1992 International Conference on*, IEEE, pp.1500–1505.
- [118] **Komada, S., Nomura, K., Ishida, M., Ohnishi, K. and Hori, T.** (1992). Adaptive robust force control by disturbance observer, *Industrial Electronics, Control, Instrumentation, and Automation, 1992. Power Electronics and Motion Control., Proceedings of the 1992 International Conference on*, IEEE, pp.1494–1499.
- [119] **Bo, T.X., Phuong, T.T., Ohishi, K., Yokokura, Y. and Miyazaki, T.** (2016). Robust position control using double disturbance observers based state feedback for two mass system, *Industrial Electronics Society, IECON 2016-42nd Annual Conference of the IEEE*, IEEE, pp.5814–5819.

- [120] **Roozing, W., Malzahn, J., Caldwell, D.G. and Tsagarakis, N.G.** (2016). Comparison of open-loop and closed-loop disturbance observers for series elastic actuators, *Intelligent Robots and Systems (IROS), 2016 IEEE/RSJ International Conference on*, IEEE, pp.3842–3847.
- [121] **Sariyildiz, E. and Ohnishi, K.** (2015). An adaptive reaction force observer design, *IEEE/ASME Transactions on Mechatronics*, 20(2), 750–760.
- [122] **Suzumura, A. and Fujimoto, Y.** (2016). On explicit implementation of multiple disturbance observers derived from three-degree-of-freedom control, *Advanced Motion Control (AMC), 2016 IEEE 14th International Workshop on*, IEEE, pp.442–447.
- [123] **Wang, W., Yu, L. and Yang, J.** (2017). Toward force detection of a cable-driven micromanipulator for a surgical robot based on disturbance observer, *Mechanical Sciences*, 8(2), 323.
- [124] **Ugurlu, B., Nishimura, M., Hyodo, K., Kawanishi, M. and Narikiyo, T.** (2015). Proof of concept for robot-aided upper limb rehabilitation using disturbance observers, *IEEE Transactions on Human-Machine Systems*, 45(1), 110–118.
- [125] **Narendra, K.S. and Parthasarathy, K.** (1990). Identification and control of dynamical systems using neural networks, *IEEE Transactions on neural networks*, 1(1), 4–27.
- [126] **Nho, H.C. and Meckl, P.** (2003). Intelligent feedforward control and payload estimation for a two-link robotic manipulator, *IEEE/ASME transactions on mechatronics*, 8(2), 277–282.
- [127] **Leahy, M., Johnson, M.A. and Rogers, S.K.** (1991). Neural network payload estimation for adaptive robot control, *IEEE transactions on neural networks*, 2(1), 93–100.
- [128] **Smith, A.C., Mobasser, F. and Hashtrudi-Zaad, K.** (2006). Neural-network-based contact force observers for haptic applications, *IEEE Transactions on Robotics*, 22(6), 1163–1175.
- [129] **Bishop, G. and Welch, G.** (2001). An introduction to the kalman filter, *Proc of SIGGRAPH, Course*, 8(27599-23175), 41.
- [130] **Murray, R.M., Li, Z., Sastry, S.S. and Sastry, S.S.** (1994). *A mathematical introduction to robotic manipulation*, CRC press.
- [131] **Yang, K., Yang, G., Wang, J., Zheng, T. and Yang, W.** (2015). Design analysis of a 3-DOF cable-driven variable-stiffness joint module, *Robotics and Biomimetics (ROBIO), 2015 IEEE International Conference on*, IEEE, pp.529–534.
- [132] **Petit, F. and Albu-Schäffer, A.** (2011). State feedback damping control for a multi dof variable stiffness robot arm, *Robotics and Automation (ICRA), 2011 IEEE International Conference on*, IEEE, pp.5561–5567.

- [133] **Kim, J.S., Jeong, J.H. and Park, J.H.** (2015). Inverse kinematics and geometric singularity analysis of a 3-SPS/S redundant motion mechanism using conformal geometric algebra, *Mechanism and Machine Theory*, 90, 23–36.
- [134] **Yang, K., Yang, G., Wang, Y., Zhang, C. and Chen, S.** (2017). Stiffness-oriented cable tension distribution algorithm for a 3-DOF Cable-driven variable-stiffness module, *Advanced Intelligent Mechatronics (AIM), 2017 IEEE International Conference on*, IEEE, pp.454–459.
- [135] **Flash, T. and Mussa-Ivaldi, F.** (1990). Human arm stiffness characteristics during the maintenance of posture, *Experimental brain research*, 82(2), 315–326.
- [136] **Botzer, L. and Karniel, A.** (2013). Feedback and feedforward adaptation to visuomotor delay during reaching and slicing movements, *European Journal of Neuroscience*, 38(1), 2108–2123.
- [137] **Lee, J.H. and Kim, J.H.** (2010). Investigation of the relationship between visual information and interaction force on load-on task within virtual environment, *Control Automation and Systems (ICCAS), 2010 International Conference on*, IEEE, pp.1759–1764.
- [138] **Howard, M., Braun, D.J. and Vijayakumar, S.** (2013). Transferring human impedance behavior to heterogeneous variable impedance actuators, *IEEE Transactions on Robotics*, 29(4), 847–862.
- [139] **LeCun, Y., Bengio, Y. and Hinton, G.** (2015). Deep learning, *nature*, 521(7553), 436.
- [140] **Chollet, F.** (2016). Xception: Deep learning with depthwise separable convolutions, *arXiv preprint*.
- [141] **Szegedy, C., Ioffe, S., Vanhoucke, V. and Alemi, A.A.** (2017). Inception-v4, inception-resnet and the impact of residual connections on learning., *AAAI*, volume 4, p. 12.
- [142] **Ren, S., He, K., Girshick, R. and Sun, J.** (2015). Faster r-cnn: Towards real-time object detection with region proposal networks, *Advances in neural information processing systems*, pp.91–99.
- [143] **Dai, J., Li, Y., He, K. and Sun, J.** (2016). R-fcn: Object detection via region-based fully convolutional networks, *Advances in neural information processing systems*, pp.379–387.
- [144] **Lin, T.Y., Goyal, P., Girshick, R., He, K. and Dollár, P.** (2017). Focal loss for dense object detection, *arXiv preprint arXiv:1708.02002*.
- [145] **Bayraktar, E.** (2018). Manipulation of Visually Recognized Objects Using Deep Learning, (Ph.D. thesis), Istanbul Technical University.
- [146] **Baruh, H.** (1999). *Analytical dynamics*, WCB/McGraw-Hill Boston.

CURRICULUM VITAE

Name Surname: Cihat Bora Yiğit

Place and Date of Birth: Beyoğlu, 1987

E-Mail: borayigit@yahoo.com, yigitci@itu.edu.tr

EDUCATION:

- **B.Sc.:** 2009, Istanbul Technical University, Mechanical Engineering
- **M.Sc.:** 2012, Istanbul Technical University, Mechatronics Engineering

PUBLICATIONS, PRESENTATIONS AND PATENTS ON THE THESIS:

- **Cihat Bora Yiğit**, and Pinar Boyraz. "Design and Modelling of a Cable-Driven Parallel-Series Hybrid Variable Stiffness Joint Mechanism for Robotics." *Mechanical Sciences* 8.1 (2017): 65.
- Ertugrul Bayraktar, **Cihat Bora Yiğit**, and Pinar Boyraz. "A Hybrid Image Dataset Towards Bridging The Gap Between Real and Simulation Environments For Robotics." *Machine Vision and Applications* (Under review)
- **Cihat Bora Yiğit**, Ertugrul Bayraktar, and Pinar Boyraz. "Low-Cost Variable Stiffness Joint Design Using Translational Variable Radius Pulleys." *Mechanism and Machine Theory* (Under review)
- Pinar Boyraz, **Cihat Bora Yigit**, and H. Okan Bicer. "UMAY 1: A modular humanoid platform for education and rehabilitation of children with autism spectrum disorders." *Control Conference (ASCC), 2013 9th Asian. IEEE*, 2013.
- Halise Türkmen, Nazlı Öksüzömer, **Cihat Bora Yiğit**, Ertuğrul Bayraktar, Haluk Küçük, Pinar Boyraz. "Robust and smooth colour tracking by a tendon driven humanoid neck" *8th International Conference on Image Processing, Wavelet and Applications*, 22-24 September, Istanbul Turkey, 2016
- Ertuğrul Bayraktar, **Cihat Bora Yiğit**, Pinar Boyraz. "Tailoring the AI for Robotics: Fine-tuning Predefined Deep Convolutional Neural Network Model for a Narrower Class of Objects", *ICMSCE 2017*, 2-4 February, Kayseri Turkey, 2017
- **Cihat Bora Yiğit**, Ozan Kaya, Ertuğrul Bayraktar, Pinar Boyraz. "Online External Force/Torque Estimation of Antagonistic Cable-driven Flexible Joints Using Only Position Sensors", *ICMSCE 2017*, 2-4 February, Kayseri Turkey, 2017

- Ertuğrul Bayraktar, **Cihat Bora Yiğit**, Pinar Boyraz. " Visual Recognition of Objects with CNN and Object Manipulation", ICMSCE 2017, 2-4 February, Kayseri Turkey, 2017
- Ertuğrul Bayraktar, **Cihat Bora Yiğit**, and Pinar Boyraz. "Robotic arm control by fine-tuned convolutional neural network model." Signal Processing and Communications Applications Conference (SIU), 2017 25th. IEEE, 2017.
- Nese Topuz, Huseyin Burak Kurt, Pinar Boyraz, **Cihat Bora Yigit**, "Servis Amaçlı Robotlarda Modüler ve Esnek Boyun Mekanizması Tasarımı ve Kontrolü", TOK 2014, Kocaeli, Turkey, 2014

OTHER PUBLICATIONS, PRESENTATIONS AND PATENTS:

- **Cihat Bora Yigit**, and Erdinc Altug. "Visual Attitude Estimation and Stabilization of Flying Robots." Mobile Robots for Dynamic Environments. ASME Press, 2015
- **Cihat Bora Yigit**, and Erdinc Altug. "Visual attitude stabilization of a unmanned helicopter in unknown environments with an embedded single-board computer."Robotic and Sensors Environments (ROSE), 2012 IEEE International Symposium on. IEEE, 2012.
- Arezou Rahimi, **Cihat Bora Yigit**, Behnaz Hoseini, Pinar Boyraz, "Visual Servo-Control Application in Humanoid Robots using Depth- Camera Information", Contech 2013, Istanbul, Turkey, 2013
- Behnaz Hosseini, **Cihat Bora Yigit**, Arezou Rahimi, Pinar Boyraz, " Indirect Force Control in 6DOF Humanoid Robot Arm using Impedance controller", Contech 2013, Istanbul, Turkey, 2013
- Baris Ozcan, Pinar Boyraz, and **Cihat Bora Yigit**, "A MonoSLAM approach to lane departure warning system." 2014 IEEE/ASME International Conference on Advanced Intelligent Mechatronics. IEEE, 2014
- Gokce Burak Taglioglu, **Cihat Bora Yigit**, Eray Cakiray, Mesut Acar, "Moduler Mobil Robot Tasarımı ve Imalati", TOK 2015, Denizli, Turkey, 2015